Department of Applied Physics

Quantum state control with a superconducting qubit

Karthikeyan Sampath Kumar

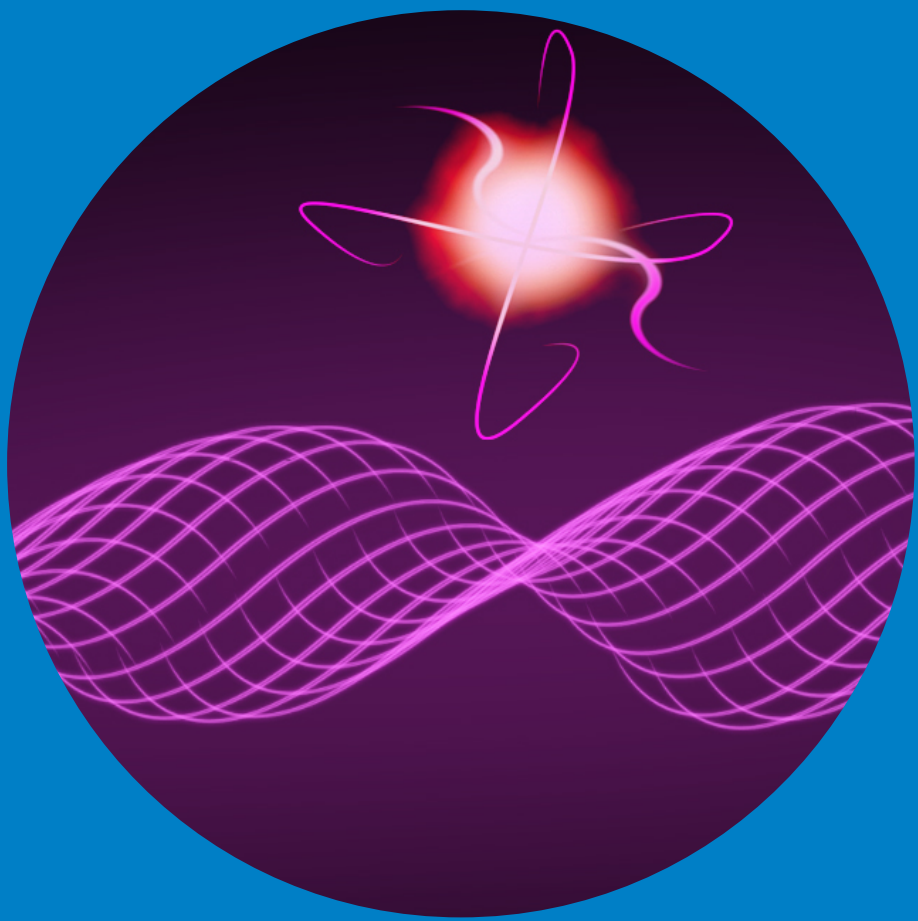

Aalto University

DOCTORAL DISSERTATIONS

Aalto University publication series
DOCTORAL DISSERTATIONS 158/2015

Quantum state control with a superconducting qubit

Karthikeyan Sampath Kumar

A doctoral dissertation completed for the degree of Doctor of Science (Technology) to be defended, with the permission of the Aalto University School of Science, at a public examination held at the lecture hall M232, Otakaari 1, of the school on 4 December 2015 at 12:00.

Aalto University
School of Science
Department of Applied Physics
Kvantti group

Supervising professor
Prof. Jukka Pekola

Thesis advisor
Doc. Sorin Paraoanu

Preliminary examiners
Dr. Juan Jose Garcia Ripoll, Instituto de Fisica Fundamental, Spain
Prof. Nadav Katz, The Racah Institute of Physics, Jerusalem

Opponent
Dr. Olivier Buisson, Institut Neel, France

Aalto University publication series
DOCTORAL DISSERTATIONS 158/2015

ISBN 978-952-60-6477-2 (printed)
ISBN 978-952-60-6478-9 (pdf)
ISSN-L 1799-4934
ISSN 1799-4934 (printed)
ISSN 1799-4942 (pdf)
http://urn.fi/URN:ISBN:978-952-60-6478-9

Unigrafia Oy
Helsinki 2015

Finland

441 697
Printed matter

Aalto University

Abstract

Aalto University, P.O. Box 11000, FI-00076 Aalto www.aalto.fi

Author
Karthikeyan Sampath Kumar

Name of the doctoral dissertation
Quantum state control with a superconducting qubit

Publisher School of Science

Unit Department of Applied Physics

Series Aalto University publication series DOCTORAL DISSERTATIONS 158/2015

Field of research Engineering Physics, circuit QED, Quantum Information

Manuscript submitted 17 August 2015 **Date of the defence** 4 December 2015

Permission to publish granted (date) 12 October 2015 **Language** English

☐ **Monograph** ☒ **Article dissertation (summary + original articles)**

Abstract

This thesis explores circuit quantum electrodynamics (circuit QED), an experimental platform for studying fundamental quantum-optics phenomena in the microwave regime. For the realization of a quantum processor, this architecture offers the advantage of scalability and the use of technologies similar to those used in the semiconductor industry. The circuit QED system studied in this thesis is called transmon, and it consists of a superconducting qubit (a tunable artificial atom) coupled to a one-dimensional coplanar waveguide resonator. The qubit can be designed to have a very large electric dipole moment, leading to the strong coupling regime which was hard to reach in optical cavity QED. The main motivation of this thesis is to study the quantum states that can be prepared using this device and how they can be manipulated under various types of modulation.

In the early 1980s, Richard Feynman proposed that quantum computers would be useful in performing powerful computational tasks and could perform simulations of interacting quantum many-body systems. In this light, the thesis starts by exploring novel ways of designing gate sequences. The quest to understand if there are fundamental limitations for the speeding-up of standard quantum algorithms prompted us to discover a new quantum impossibility result: the quantum no-reflection theorem. Next, we present our experimental results obtained with the transmon. We discuss the physics of dispersive coupling between the qubit and resonator and we explore the nonlinearities induced by the presence of the qubit when the resonator is strongly driven. Then, the thesis presents the first steps taken in the direction of simulating many-body quantum systems, where the motional averaging observed in NMR based systems was simulated in a circuit QED architecture. By changing the modulation of the qubit from random to periodic latching, we observe a Stückelberg interference spectrum in a strong nonadiabatic regime where the Landau-Zener formula is not valid. Finally, the last chapter of the thesis is devoted to the presentation of our experimental results on quantum state control, from Rabi oscillations to stimulated Raman adiabatic passage.

Keywords Quantum computation, quantum information, superconducting artificial atom, circuit QED, motional averaging, STIRAP

ISBN (printed) 978-952-60-6477-2 **ISBN (pdf)** 978-952-60-6478-9

ISSN-L 1799-4934 **ISSN (printed)** 1799-4934 **ISSN (pdf)** 1799-4942

Location of publisher Helsinki **Location of printing** Espoo **Year** 2015

Pages 170 **urn** http://urn.fi/URN:ISBN:978-952-60-6478-9

A! Aalto-yliopisto

Tiivistelmä

Aalto-yliopisto, PL 11000, 00076 Aalto www.aalto.fi

Tekijä
Karthikeyan Sampath Kumar

Väitöskirjan nimi
Quantum state control with a superconducting qubit

Julkaisija Perustieteiden korkeakoulu

Yksikkö Department of Applied Physics

Sarja Aalto University publication series DOCTORAL DISSERTATIONS 158/2015

Tutkimusala Engineering Physics, Quantum Information

Käsikirjoituksen pvm 17.08.2015 **Väitöspäivä** 04.12.2015

Julkaisuluvan myöntämispäivä 12.10.2015 **Kieli** Englanti

☐ **Monografia** ☒ **Yhdistelmäväitöskirja (yhteenveto-osa + erillisartikkelit)**

Tiivistelmä

Tämän vaitöskirjan aiheena on sähköpiirien kvanttielektrodynamiikka (QED, quantum electrodynamics), jota sovelletaan kokeellisesti perustavanlaatuisten kvanttioptiikan ilmiöiden tutkimiseen mikroaaltoalueella. Kvanttilaskennan realisoimisessa sähköpiirien QED:n etuna on sen skaalautuvuus ja yhteensopivuus puolijohdeteollisuuden käyttämien teknologioiden kanssa. QED-systeemi, johon tässä väitöskirjassa keskitytään, on suprahjohtava transmon-kubitti (säädettävä keinotekoinen atomi), joka on kytketty yksiulotteiseen aaltojohtovärähtelijään. Kubitti voidaan suunnitella siten, että sillä on erittäin suuri sähköinen dipolimomentti, mikä johtaa suureen kytkentään aaltojohdon ja kubitin välillä. Vastaavaa kytkentää on ollut vaikea saavuttaa optiseen onkaloon perustuvissa QED-systeemeissä. Tämän väitöskirjan tärkein sisältö on transmonilla saavutettavien kvanttitilojen ja niiden manipuloinnin tutkiminen.

1980-luvun alussa Richard Feynman esitti kvanttitietokoneiden olevan hyödyllisiä sekä laskennallisiin tarkoituksiin että vuorovaikuttavien monen kappaleen kvanttisysteemien mallintamiseen. Tämän inspiroimana väitöskirja alkaa tutkimalla uusia tapoja suunnitella kvanttilogiikkaporttien sarjoja. Yrittäessämme ymmärtää olennaisia rajoja kvanttialgoritmien nopeuttamiseksi, löysimme uuden tuloksen: kvanttiheijastumattomuusteoreeman. Tämän jälkeen esitämme kokeellisia tuloksia transmon-mittauksista. Esittelemme kubitin ja resonaattorin väliseen dispersiiviseen kytkentään liittyvää fysiikkaa ja tutkimme korkean tehon mikroaalloilla viritetyn värähtelijän ja kubitin läsnäolon aiheuttamia epälineaarisuuksia. Tässä väitöksessä myös otetaan ensiaskelia kohti monen kappaleen kvanttisimulaatioita kokeellisesti mallintamamalla ydinmagneettisessa resonanssissa (NMR, nuclear magnetic resonance) tapahtuvaa liikkeen keskiarvoistumista käyttäen QED-systeemiä. Vaihtamalla kubitin modulaatiota satunnaisaallosta kanttiaaltomuotoiseksi, havaitsemme Stückelberg interferenssin epäadiabaattisella rajalla, jossa Landau-Zener yhtälö ei enää toimi. Väitöskirjan viimeisessä osassa keskitytään kvanttitilan kontrollointiin liittyvien kokeellisten tulostemme esittelyyn aina Rabi-oskillaatioista stimuloituun adiabaattiseen Raman prosessiin.

Avainsanat Quantum computation, quantum information, superconducting artificial atom, circuit QED, motional averaging, STIRAP

ISBN (painettu) 978-952-60-6477-2 **ISBN (pdf)** 978-952-60-6478-9

ISSN-L 1799-4934 **ISSN (painettu)** 1799-4934 **ISSN (pdf)** 1799-4942

Julkaisupaikka Helsinki **Painopaikka** Espoo **Vuosi** 2015

Sivumäärä 170 **urn** http://urn.fi/URN:ISBN:978-952-60-6478-9

This thesis explores circuit quantum electrodynamics (circuit QED), an experimental platform for studying fundamental quantum-optics phenomena in the microwave regime. For the realization of a quantum processor, this architecture offers the advantage of scalability and the use of technologies similar to those used in the semiconductor industry. The circuit QED system studied in this thesis is called transmon, and it consists of a superconducting qubit (a tunable artificial atom) coupled to a one-dimensional coplanar waveguide resonator. The qubit can be designed to have a very large electric dipole moment, leading to the strong coupling regime which was hard to reach in optical cavity QED. The main motivation of this thesis is to study the quantum states that can be prepared using this device and how they can be manipulated under various types of modulation.

In the early 1980s, Richard Feynman proposed that quantum computers would be useful in performing powerful computational tasks and could perform simulations of interacting quantum many-body systems. In this light, the thesis starts by exploring novel ways of designing gate sequences. The quest to understand if there are fundamental limitations for the speeding-up of standard quantum algorithms prompted us to discover a new quantum impossibility result: the quantum no-reflection theorem. Next, we present our experimental results obtained with the transmon. We discuss the physics of dispersive coupling between the qubit and resonator and we explore the nonlinearities induced by the presence of the qubit when the resonator is strongly driven. Then, the thesis presents the first steps taken in the direction of simulating many-body quantum systems, where the motional averaging observed in NMR based systems was simulated in a circuit QED architecture. By changing the modulation of the qubit from random to periodic latching, we observe a Stückelberg interference spectrum in a strong nonadiabatic regime where the Landau-Zener formula is not valid. Finally, the last chapter of the thesis is devoted to the presentation of our experimental results on quantum state control, from Rabi oscillations to stimulated Raman adiabatic passage.

Preface

The research work presented in this thesis was carried out at the O.V. Lounasmaa Laboratory of Aalto University between January 2010 and December 2014.

During the years I have worked in the lab, I have managed to gather a long list of people to thank for. Undoubtedly, my supervisor as well as the leader of the Kvantti group, Docent Sorin Paraoanu receives my first gratitude for introducing me into the field of superconducting quantum circuits, for his instructive guidance and the ideas he shared throughout my study and research. I practically had no experience on experimental physics when I started in his group. I thank him for all the patience and trust he has had on me over the years. In addition to the guidance he has given me, he has provided me an exemplary role model of a top-level physicist.

Second, I would like to thank Khattiya Chalapat, a member of the Kvantti group who introduced me to clean room fabrication techniques, and Jian Li who introduced me to the nuances of handling a dilution refrigerator.

Many thanks to Dr. Alexander Savin for his patience and valuable advices to help me solve problems in cooling down the dilution refrigerator, especially at the early stage of my PhD and for keeping the lab running.

I am so grateful to Prof. Pertti Hakonen, the director of the O.V. Lounasmaa Laboratory and the leader of the Nano group, for his constructive suggestions and spirited discussions and for the enormous amount of work he puts in to make the lab run as a whole. I also want to thank the former director of the laboratory Prof. Mikko Paalanen and all the lab administration for making it possible for me complete the thesis in our laboratory.

I want to express my gratitude to all the co-authors of the articles included in this thesis. It has been a great privilege to work with all the

present members and alumni in the Kvantti group: Sergey Danilin, Robab Jabdaraghi, Antti Vepsäläinen, and for the discussions with Juha-Matti Pirkkalainen. I am grateful to all the colleagues who used to be and presently are in Office Room 162a: Vitaly Emets, Pasi Häkkinen, Raphaël Khan, Daniel Cox, Ville Kauppila, Pasi Lähteenmäki, Mika Oksanen, Antti Puska, Jayanta Sarkar, Xuefeng Song, and Matti Tomi, for their efforts to create a pleasant and lively working atmosphere. I am also grateful to Prof. Erkki Thuneberg, Dr. Jani Tuorila and Prof. Jukka Pekola.

The financial support of my studies from the Academy of Finland under a grant of my supervisor Sorin Paraoanu is acknowledged. I am deeply grateful to my family for their endless support and encouragement.

Espoo, October 22, 2015,

K. S. Kumar

Contents

List of Publications

This thesis consists of an overview and of the following publications which are referred to in the text by their Roman numerals.

I K. S. Kumar and G. S. Paraoanu. A quantum no-reflection theorem and the speeding up of Grover's search algorithm. *EPL*, 93, 20005, 2011.

II K. S. Kumar and G. S. Paraoanu. Designing quantum gates using the genetic algorithm. In *26th International Conference on Low Temperature Physics (LT26)*, Beijing, China, J. Phys.: Conf. Ser. 400 022101, August 2011.

III J. Li, M. P. Silveri, K. S. Kumar, J.-M. Pirkkalainen, A. Vepsäläinen, W. C. Chien, J. Tuorila, M. A. Sillanpää, P. J. Hakonen, E. V. Thuneberg and G. S. Paraoanu. Motional Averaging in a Superconducting Qubit. *Nature Communications, 4, 1420*, 2013.

IV J. Li, M. P. Silveri, K. S. Kumar, J.-M. Pirkkalainen, A. Vepsäläinen, W. C. Chien, J. Tuorila, M. A. Sillanpää, P. J. Hakonen, E. V. Thuneberg and G. S. Paraoanu. Simulation of motional averaging using a superconducting circuit. In *Progress In Electromagnetics Research Symposium*, Stockholm, Sweden, 785-788, August 2013.

V M. P. Silveri, K. S. Kumar, J. Tuorila, J. Li, A. Vepsäläinen, E. V. Thuneberg and G. S. Paraoanu. Stückelberg interference in a superconducting qubit under periodic latching modulation. *New J. Phys.*, 17, 043058, 2015.

VI K. S. Kumar, A. Vepsäläinen, S. Danilin, and G. S. Paraoanu. Stimulated Raman adiabatic passage using a three-level superconducting circuit. *arXiv:1508.02981v1*, 4-August 2015.

Author's Contribution

Publication I: "A quantum no-reflection theorem and the speeding up of Grover's search algorithm"

The author did the initial calculations and contributed in the further development of the ideas and the writing of the manuscript.

Publication II: "Designing quantum gates using the genetic algorithm"

The author had the initiative of performing this study; he did the numerical simulations and wrote the manuscript.

Publication III: "Motional Averaging in a Superconducting Qubit"

The author contributed to all the measurements, and in particular took and analyzed the data on Rabi oscillations on the sidebands.

Publication IV: "Simulation of motional averaging using a superconducting circuit"

The author provided the experimental parameters for the simulations and participated in the writing of the manuscript.

Publication V: "Stückelberg interference in a superconducting qubit under periodic latching modulation"

The author did the measurements for this experiment as well as some of the data analysis, and discussed the results with the other authors.

Publication VI: "Stimulated Raman adiabatic passage using a three-level superconducting circuit"

The author realized the experimental setup, took many data sets with different parameters, and contributed to the data analysis and discussions about the manuscript.

Other Author's contributions: The author did an extensive experimental study of nonlinearities in the Jaynes-Cumming model. Some of the results are presented in Chapter 3.4 and in K. S. Kumar, I. Pietikäinen, S. Danilin, J. Tuorila, and G. S. Paraoanu, Qubit-induced nonlinearities in a strongly driven superconducting resonator, manuscript (2015).

1. Introduction

Research in the field of quantum mechanics started just about a century ago, with the introduction of revolutionary concepts such as the quantization of energy, photons, and wave-particle duality. Since then, quantum mechanics has grown into a very successful theory capable of explaining most of the experiments, from the microscopic scale to the phenomena occuring in stars and other large-scale structures in the universe. Subsequent technological and theoretical developments of the 20^{th} century allowed physicists to analyse and test quantum-level effects in the laboratory - opening the doors to newer applications.

One such exciting application is the processing of information using quantum devices. In quantum computing the aim is to encode classical information into the state of a system and then to perform a set of gates (a quantum algorithm) to realize a certain computational task. In classical computing, the information is stored as bits, where each bit can be either 0 or 1, at a particular instance. With a qubit (**qu**antum **bit**), the quantum nature of the physical system allows the information to take the value 0 and 1 simultaneously. It is this possibility of exploiting quantum properties such as superposition of states, quantum entanglement etc., for the purpose of information processing, that allows quantum computers to be potentially more powerful than classical computers.

Indeed, quantum systems exhibit exotic properties such as entanglement of states. Exploiting entanglement allows experiments such as quantum teleportation, which has no classical analogue. Another possible task in a quantum system is quantum cryptography that provides an unconditionally secure information transmission which is impossible in the classical sense. Quantum algorithms have also been developed that can solve a problem much faster than a classical algorithm; well-known examples being Shor's factoring algorithm that provides an exponential speedup,

and Grover's search algorithm that provides a quadratic speedup when compared to the classical algorithms. Richard Feynman had proposed the quantum computer as a viable way to simulate many body quantum physics. Simulating complex systems such as a large molecule with its iteractions is computationally inefficient on a classical computer. The possibility of a speedup in these calculations is a major motivational factor driving research interest in the direction of quantum information processing.

There are many potential quantum computer architectures such as ion traps, cavity QED, nuclear magnetic resonance, spin in few-electron quantum dots, *etc*., but the scalability feature of the superconducting qubit makes it a more promising candidate. Some of the early proposals for the use of Josephson junctions to realize superconducting qubits are due to Shnirman in 1997 [1], followed by the Cooper pair box realization by Devoret in 1998 [2] . The coherent oscillations in a Cooper pair box were experimentally achieved by Nakamura *et al.* in 1999 [3]. Josephson junction based qubit design has been under active research for less than the last two decades. Though in its infancy, the research has shown significant progress and the challenges are actively addressed.

The thesis is organized as follows. Chapter 2 presents the concepts of quantum information; from qubits to quantum gates and quantum algorithms leading to our discovery of a new quantum impossibility result: the quantum no-reflection theorem. The chapter finishes by explaining the use of a genetic algorithm to implement quantum gates experimentally. Following that, our genetic algorithm simulation results for a Hamiltonian that can model a circuit quantum electrodynamics qubit is presented. This work leads to a better understanding of the qubit gate, from a black box schematic to an experimental realization.

Chapter 3 explains circuit quantum electrodynamics as an experimental platform to implement a quantum two-level system (transmon qubit), coupled to a one-dimensional coplanar waveguide, acting as a microwave resonator. Following that, our measurement results showing the nonlinearity effects of the coupled system, when the cavity is strongly driven, are presented.

Chapter 4 presents the spectral measurements of a transmon qubit. The transmon qubit behaves as a tunable artificial atom. A rich interference pattern emerges when the transition frequencies are modulated sinusoidally, by square waves and by random telegraph signal. The interesting

new results are the motional averaging observed when the transition frequency is subject to random telegraph noise and the novel adiabatic-impulse model for the evolution of the system subject to square wave modulation.

Chapter 5 starts with the quantum state control in a transmon system, when it is used as a two-level system. The latter part describes STIRAP, a robust population transfer scheme for a three-level system and describes our STIRAP measurement results for a three-level transmon presented in Ref. arXiv:1508.02981v1.

2. Quantum Computation and Quantum Information

"Computers are physical objects, and computations are physical processes. What computers can or cannot compute is determined by the laws of physics alone, and not by pure mathematics."
- David Deutsch [4]

In the latter part of the last century we saw a tremendous progress in research that led to better and fuller understanding of quantum mechanics. This understanding might lead to the harnessing of quantum mechanics into novel technologies and applications. Quantum computing is one such outcome, which emerges from the question whether it is possible to use quantum states to represent information and employ the mechanisms of quantum physics to process it.

In quantum mechanics, a physical system is characterized by a set of quantum states. Mathematically, quantum states are represented as state vectors in a Hilbert space. Any superposition of the basis states is a possible state of the system. The evolution of the system is defined by the evolution of the state vector under a unitary operator determined by the Hamiltonian of the system and the external interactions and perturbations. Following the evolution of the state, a measurement is performed on the system, when an eigenvalue of the measured variable (operator) is found and the state of the system collapses to the corresponding eigenvector. The idea of quantum computation is to use the quantum properties of the system to represent data and to devise quantum mechanisms to perform operations on this data. Making use of quantum mechanical phenomena such as superposition and entanglement leads to quantum parallelism in computation which can result into an exponential speedup in finding the solution of some specific problems (for example, factorization through Shor's algorithm). The research on quantum computing gained a significant impetus only in the last couple of decades. A few experiments have been carried out on

a small number of qubits (**qu**antum **bit**) where quantum computational tasks have been successfully demonstrated.

There are many suitable quantum systems based on nuclear magnetic resonance, electronic resonance, ion traps *etc*., which can be used to store and manipulate quantum information. But independent of the architecture, the qubit is mathematically equivalent to a spin $^1/_2$ system and hence can be modelled by a similar Hamiltonian. One challenge common to all the architectures for quantum computing is the isolation of the spin $^1/_2$ system from the environment. Interaction of the quantum systems with the environment is an irreversible process, leading to loss of information. Decoherence is one of the main limiting factors in building a quantum computer.

2.1 Qubits

The elementary unit of classical information is the bit, whereas for quantum information we need to introduce the concept of quantum bit. A qubit is just a quantum system which can be approximately described by a two-dimensional Hilbert space. Thus, the qubit is essentially a two-level system. Though many physical realizations of qubits are possible, the physical definition of information content is the same for all different architectures and its dynamics follow the same fundamental physics.

In order to establish the notations, we define a two dimensional Hilbert space, with basis states $|0\rangle, |1\rangle$. Contrary to the classical bit, which can exist in only one of the basis states at a given instant, the qubit can be put in any arbitrary linear superposition of the basis states, represented as $|\psi\rangle = \alpha|0\rangle + \beta|1\rangle$, where $(\alpha, \beta) \in \mathbb{C}$ with the normalization $|\alpha|^2 + |\beta|^2 = 1$. This can be written in vector notation as

$$|0\rangle = \begin{bmatrix} 1 \\ 0 \end{bmatrix}, |1\rangle = \begin{bmatrix} 0 \\ 1 \end{bmatrix}, |\psi\rangle = \begin{bmatrix} \alpha \\ \beta \end{bmatrix}, \text{and } \rho = |\psi\rangle\langle\psi| = \begin{bmatrix} \alpha^*\alpha & \beta^*\alpha \\ \alpha^*\beta & \beta^*\beta \end{bmatrix}, \quad (2.1)$$

with ρ the density matrix. Though the qubit can exist in an infinite number of quantum states, finding the coefficients α and β is not a deterministic process. A single measurement randomly collapses the qubit into the basis state $|0\rangle$ or $|1\rangle$ with the probability $|\alpha|^2$ or $|\beta|^2$, respectively.

The pure state of a qubit can be better understood using a graphical representation known as a Bloch sphere, named after the physicist Felix Bloch. The Bloch sphere is a unit sphere, representing the two dimensional Hilbert space, as shown in Fig. 2.1. This representation maps $|0\rangle$ to the

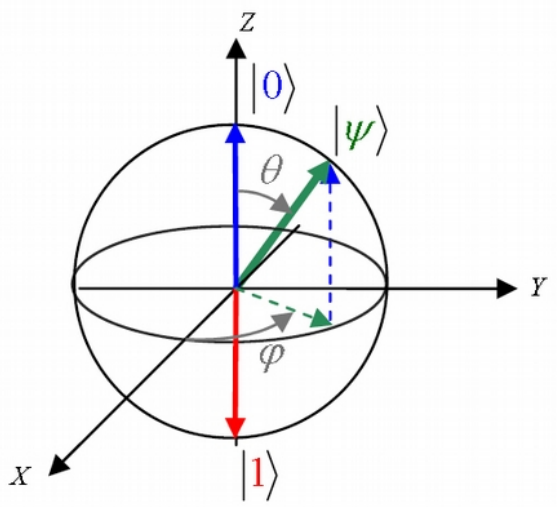

Figure 2.1. Bloch sphere representation of a qubit.

North Pole and $|1\rangle$ to the South Pole. The equator represents an equal superposition of the two states: $\frac{1}{\sqrt{2}}(|0\rangle + e^{i\phi}|1\rangle)$. Pure qubit states are be represented as points on the surface of the sphere, whereas the interior points correspond to mixed states. In cartesian coordinates, the Bloch vector, $|\psi\rangle$ is given by $(\cos\phi\sin\theta, \sin\phi\sin\theta, \cos\theta)$.

In this representation, the general qubit state $|\psi\rangle$ can be written in terms of the basis states $|0\rangle$ and $|1\rangle$ as

$$|\psi\rangle = e^{i\gamma}\left\{\cos\left(\frac{\theta}{2}\right)|0\rangle + e^{i\phi}\sin\left(\frac{\theta}{2}\right)|1\rangle\right\}, \tag{2.2}$$

with $0 \leq \theta < \pi$ and $0 \leq \phi < 2\pi$. The global phase γ plays no role in the dynamics of the quantum system.

This definition can be extended for a multiple qubit system. When there are multiple qubits involved, the Hilbert space consists of a tensor product of the individual qubit spaces. An n qubit system, requires a 2^n dimensional Hilbert space to define the system. An arbitrary normalized n qubit state can be represented as a superposition of the basis states, as

$$|\psi\rangle = \sum_{i=0}^{2^n-1} a_i|i\rangle, \tag{2.3}$$

where the normalization imposes that $\sum_i |a_i|^2 = 1$, so that the probability of measuring $|i\rangle$ is $|a_i|^2$.

Within this 2^n dimensional complex space there exists state vectors that cannot be factored into a product of states of the individual qubits. In this case, the qubits are said to be entangled. Even if the qubits are spatially

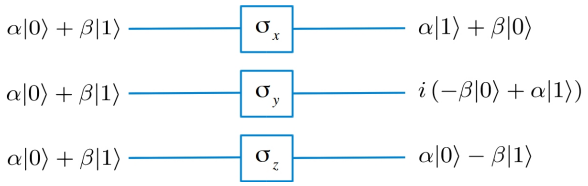

Figure 2.2. Single qubit X, Y and Z quantum gates.

Figure 2.3. Single qubit Hadamard gate.

separated, the measurements on entangled qubits result in correlated values. Some of these correlations do not have a classical analog, as shown by Bell's theorem [5]. This remarkable feature is exploited in quantum information processing tasks such as quantum teleportation, and quantum cryptography.

2.2 Qubit gates

The objective of Quantum Information Processing (QIP), is to implement coherent control on qubits with quantum gates. A one qubit quantum gate can be thought of as a rotation of a vector on the Bloch sphere (Fig. 2.1). A sequence of quantum gates can be engineered to produce a quantum circuit that allows arbitrary rotations of the qubit. Some nontrivial single qubit gates are the Pauli matrices, σ_x , σ_y and σ_z [6].

$$\sigma_x|0\rangle = |1\rangle; \sigma_x|1\rangle = |0\rangle; \sigma_y|0\rangle = i|1\rangle; \sigma_y|1\rangle = -i|0\rangle; \sigma_z|0\rangle = |0\rangle; \sigma_z|1\rangle = -|1\rangle, \tag{2.4}$$

with the matrix representation,

$$\sigma_x = \begin{pmatrix} 0 & 1 \\ 1 & 0 \end{pmatrix}, \sigma_y = \begin{pmatrix} 0 & -i \\ i & 0 \end{pmatrix}, \sigma_z = \begin{pmatrix} 1 & 0 \\ 0 & -1 \end{pmatrix}. \tag{2.5}$$

One sees immediately that σ_x is similar to the NOT gate that flips the bit, σ_y is the bit flip with an additional phase and σ_z is the phase flip operator. (Fig. 2.2).

Another interesting single qubit gate for which there exists no classical analogue is the Hadamard gate H (Fig. 2.3), which, when operating on one of the basis states $|0\rangle$ or $|1\rangle$, flips it half way to the equatorial plane of the Bloch sphere. On subsequent application, we obtain the original state as $HH = I$. The Hadamard gate is written in the matrix form as

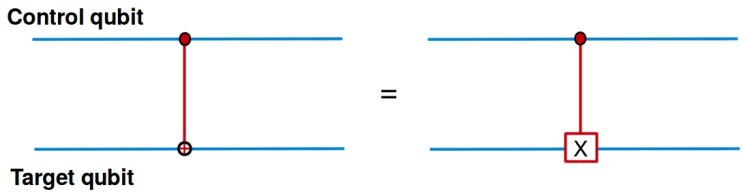

Figure 2.4. Schematic of a two qubit CNOT gate.

Figure 2.5. Two level system subject to Harmonic perturbation.

$$H = \frac{1}{\sqrt{2}} \begin{pmatrix} 1 & 1 \\ 1 & -1 \end{pmatrix}. \tag{2.6}$$

An example of the two qubit gate is the controlled NOT gate (CNOT). The schematic of the CNOT gate is shown in Fig. 2.4. In the CNOT gate the first qubit is the control qubit while the second qubit is the target qubit. The target qubit will be operated by the σ_x operator if and only if the control qubit is 1. If the control qubit is 0, no gate is applied to the target qubit. Both the control qubit and target qubit can be in a superposition state. The cNOT gate operation can be defined as

$$\text{CNOT}|00\rangle = |00\rangle; \text{CNOT}|01\rangle = |01\rangle; \text{CNOT}|10\rangle = |11\rangle; \text{CNOT}|11\rangle = |10\rangle, \tag{2.7}$$

and the matrix representation as

$$\text{CNOT} = \begin{pmatrix} 1 & 0 & 0 & 0 \\ 0 & 1 & 0 & 0 \\ 0 & 0 & 0 & 1 \\ 0 & 0 & 1 & 0 \end{pmatrix}. \tag{2.8}$$

Harmonic perturbation and Rabi oscillations : realizing single-qubit gates

The harmonic perturbation of a two level system and the resulting Rabi oscillations are a good starting point to understand quantum gates for a single qubit system. Consider a two level system with an energy separation of $\hbar\nu$ and an external perturbation at frequency ω as shown in Fig. 2.5.

The Hamiltonian of the two level system can be expressed in the eigen-

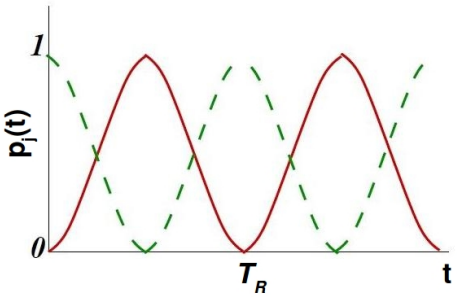

Figure 2.6. The continuous line represents the occupation probability for state $|0\rangle$ and the dotted line the occupation probability for state $|1\rangle$.

basis of the non-perturbed qubit as

$$H = \frac{\hbar\nu}{2}\sigma_z + \hbar\Omega\cos(\omega t)\sigma_x. \tag{2.9}$$

Let $\nu = \omega$, when the external field is at resonance with the energy splitting. Consider a general state of the system,

$$|\psi\rangle = a(t)e^{-i\nu t/2}|1\rangle + b(t)e^{i\nu t/2}|0\rangle. \tag{2.10}$$

Now allow the state to evolve under the Hamiltonian

$$H|\psi\rangle = i\hbar\frac{\partial}{\partial t}|\psi\rangle. \tag{2.11}$$

Solving equation (2.11) with rotating wave approximation will show that the probability of occupancy of the states $|0\rangle$ and $|1\rangle$ oscillates in time with the Rabi frequency Ω and hence a Rabi time period $T_R = 2\pi/\Omega$ as shown in Fig. 2.6.

When the external perturbation is switched off at $T_R/2$, the state $|0\rangle$ goes to $|1\rangle$ (or $|1\rangle$ goes to $|0\rangle$), which represents a bit flip operation. When the external perturbation is switched off at $T_R/4$, it can be seen that the system ends in a coherent superposition of $|0\rangle$ and $|1\rangle$ state.

2.3 The quantum computer

The CNOT gate along with single qubit phase gates U_ϕ, that rotate a single qubit to any point on the Bloch sphere, form a universal set of gates for a quantum computer. Another difference with respect to classical computation is that quantum gates are reversible. A sequence of such reversible quantum gates can form a quantum circuit that can be engineered to perform a particular task. One example of a quantum circuit is shown in Fig.

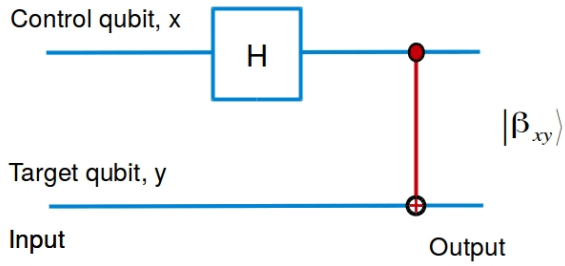

Figure 2.7. A quantum circuit that produces maximally entangled Bell states.

2.7, which creates four maximally entangled Bell states, when the control and target qubit are $\{x, y\} \in \{00, 01, 10, 11\}$.

The general guidelines for building a quantum computer has been formulated by David DiVincenzo of IBM [7]. The rules and conditions required for successful quantum computing are:

1. A register of 2-level systems (qubits).

2. Initialization of the qubit register viz., setting all the qubit states to $|00\ldots0\rangle$.

3. One and two qubit gates *e.g.*, Hadamard and CNOT gates. The product of the simple universal set of quantum gates should be able to realize any arbitrary transformation U on the N qubit system.

4. Readout of single qubits, where each of the N qubits will be projected into its basis states, $|0\rangle$, $|1\rangle$.

5. Long decoherence times, within which to complete the required quantum computational tasks.

The main challenge in realizing a quantum computer is the decoherence of the quantum states. The requirements states that the quantum architecture should allow qubit initialization, control and readout while also keeping the qubit isolated from external noise sources. Quantum computation and quantum information offers many challenges to the physicists but the new physics that is disclosed in the pursuit is rewarding in itself.

2.4 Quantum algorithms

The main factor that led the research interest in the direction of quantum computation is the invention of quantum algorithms that promises better computational performance than classical algorithms. The first instance of such an algorithm was created by David Deustch in 1985. Later, in 1994, Peter Shor proposed an algorithm that could factor large numbers exponentially faster than a classical algorithm [8]. The difficulty of factoring large numbers has been utilized in the RSA cryptography which is widely used for secure data transmission. This practical public-key cryptosystem is named after Ron Rivest, Adi Shamir, and Leonard Adleman who proposed the algorithm in 1977. The idea of a quantum computer that can break the RSA cryptosystem, as well as the possibility of creating secure data communication systems that disallow eaves-dropping (quantum cryptography) were developments that stimulated much interest. Another notable algorithm is the search algorithm proposed by Grover in 1997, which provides a quadratic speedup searching an unstructured database, in comparison to the classical search algorithm [9]. Recently, there has been rapid progress in discovering quantum algorithms with varied applications such as eigenvalue estimation [10], Gauss sum estimation [11], boson sampling [12, 13], solving linear systems of equations [14], numerical gradient estimation [15] and integration [16] *etc*., In the next section, I will focus on the Grover search algorithm. I will show that the attempt to speedup this algorithm leads to a new no-go result: the quantum no-reflection theorem.

One feature to note is that the algorithms run by a quantum computer are probabilistic, which is due to the randomness of the result of the quantum measurement. In spite of the intrinsic randomness, intrinsic quantum properties like quantum parallelism and quantum entanglement, when intelligently exploited, allow some operations like quantum teleportation and cryptography, and faster information processing than classical computers.

2.5 Quantum search algorithm

Among all quantum algorithms, Grover's quantum search scheme is perhaps the one which is simplest but at the same time solves a very useful problem. It is a heuristic search problem that is more efficient than classical search, as the size of the database increases. If the search space

consists of N points to search, a classical computer would take $\mathcal{O}(N)$ operations to determine the solution, whereas the Grover's quantum search problem would find solution in $\mathcal{O}(\sqrt{N})$ operations. The quantum search algorithm offers only a quadratic speedup as opposed to the exponential speedup provided by the Shor's factoring problem, but it is still of great interest as the range of applications is wider.

2.5.1 The standard Grover search algorithm

In this section, I will explain the Grover search algorithm [6, 9] with the intention of providing an illustration of how an algorithm can be broken down into simple quantum circuits, which are just products of simple quantum gates.

In order to search a space of N elements, we need n qubits which serves as an index to the elements. This imposes that $N = 2^n$, so all the elements to be included in the search are addressed. The search problem has M exact solutions, such that $1 \leq M \leq N$. Let the function $f(x)$, be the objective function that finds the solution to the search problem, which takes one particular index x, in the range of 0 to $N-1$, and outputs $f(x) = 1$, if x points to a solution to the search problem, and 0 otherwise.

The Grover operator can be defined as $G = (2|\psi\rangle\langle\psi| - I)O$, where $|\psi\rangle$ is the initial uniform superposition state and O is the oracle operator. The initial uniform superposition state $|\psi\rangle$ is iterated by the Grover operator $\mathcal{O}(\sqrt{N/M})$ times and measured in the computational basis to complete the quantum search algorithm. In the following text, I present the complete formulation of the search algorithm and in the latter section, I show how using a 2-d geometric visualisation results in a quite simple picture of the search process.

We start by introducing the Oracle operator as

$$|x\rangle|q\rangle \xrightarrow{O} |x\rangle|q \oplus f(x)\rangle. \tag{2.12}$$

When the Oracle qubit is chosen to be $(|0\rangle - |1\rangle)/\sqrt{2}$, the action of the oracle becomes

$$|x\rangle \frac{|0\rangle - |1\rangle}{\sqrt{2}} \xrightarrow{O} (-1)^{f(x)}|x\rangle \frac{|0\rangle - |1\rangle}{\sqrt{2}}. \tag{2.13}$$

Thus it can be seen that the oracle marks the solution to the search problem by flipping its phase. Its action can be represented by the simplified notation

$$|x\rangle \xrightarrow{O} (-1)^{f(x)}|x\rangle, \tag{2.14}$$

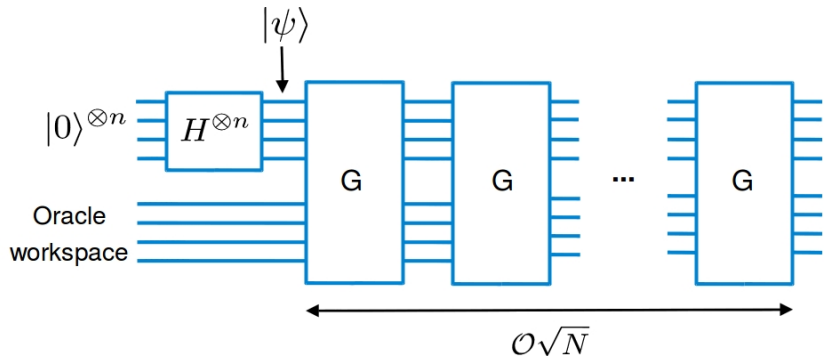

Figure 2.8. Schematic of Grover search algorithm.

as the Oracle qubit is left unchanged during its action.

The algorithm starts with the n qubits all initialised to $|0\rangle^{\otimes n}$. An n-qubit Hadamard gate is applied, to create a uniform superposition state,

$$|\psi\rangle = \frac{1}{\sqrt{N}} \sum_{0 \leq x \leq N-1} |x\rangle. \tag{2.15}$$

This state is first operated by the Oracle, and the result $O|\psi\rangle$ is operated by $(2|\psi\rangle\langle\psi| - I)$ to complete one Grover iteration. One iteration of the Grover operator can be defined as

$$G = (2|\psi\rangle\langle\psi| - I)O. \tag{2.16}$$

The operator $(2|\psi\rangle\langle\psi| - I)$ can further be written as $H^{\otimes n}(2|0\rangle\langle 0| - I)H^{\otimes n}$, which is nothing but a conditional phase shift operator sandwiched between two n-qubit Hadamard operators. It is straightforward to see that the conditional phase shift operator $(2|0\rangle\langle 0| - I)$, leaves $|0\rangle$ unchanged, but flips the phase of all other states. Thus the Grover operator can be broken down into a product of simpler operations, as shown in Fig. 2.9.

When the initial uniform superposition state $|\psi\rangle$ is iterated over the Grover operator G, $\mathcal{O}(\sqrt{N/M})$ times, and then measured in the computational basis, the measurement results should provide the index to the solution of the search problem. The algorithm is represented as a schematic circuit in Fig. 2.8.

A 2-d geometric visualisation for the search problem

It becomes quite simple to understand the Grover operation on using a two-dimensional representation by defining a superposition of all non-solution states $|\alpha\rangle = \frac{1}{\sqrt{N-M}} \sum_x'' |x\rangle$, and the superposition of all states that are solutions to the search problem $|\beta\rangle = \frac{1}{\sqrt{M}} \sum_x' |x\rangle$. Here M denotes the number of solutions of the search problem. With these notations the initial

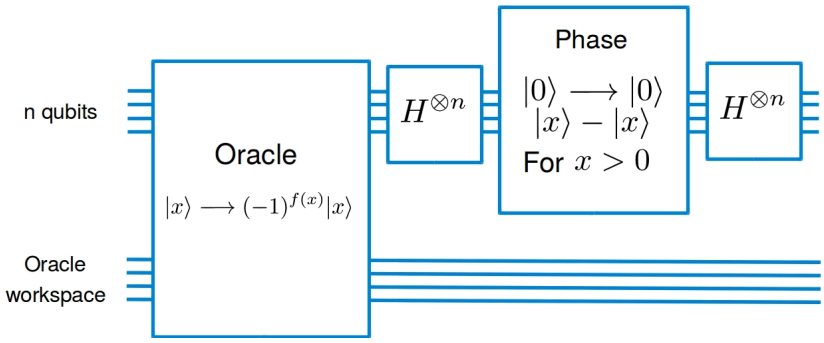

Figure 2.9. Schematic of Grover operator.

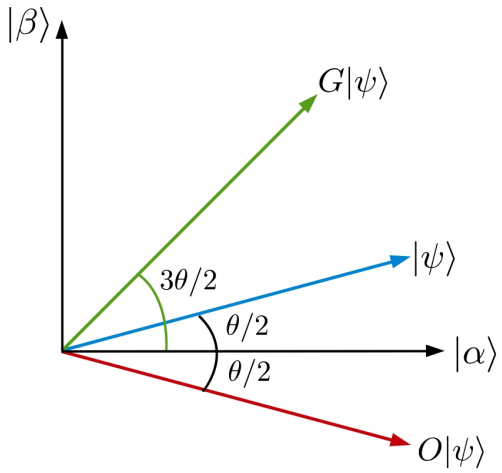

Figure 2.10. State evolution in 2-dimensions for one iteration of the Grover operator.

state is

$$|\psi\rangle = \sqrt{\frac{N-M}{N}}|\alpha\rangle + \sqrt{\frac{M}{N}}|\beta\rangle. \tag{2.17}$$

On defining $\cos\theta/2 = \sqrt{(N-M)/N}$ and $\sin\theta/2 = \sqrt{M/N}$, the initial uniform superposition state can be written as

$$|\psi\rangle = \cos\frac{\theta}{2}|\alpha\rangle + \sin\frac{\theta}{2}|\beta\rangle. \tag{2.18}$$

Then one sees that the oracle causes a reflection about the $|\alpha\rangle$ axis whereas the $(2|\psi\rangle\langle\psi| - I)$ operating on $O|\psi\rangle$ causes the state vector to get reflected about the $|\psi\rangle$ axis.

So on first iteration, the state evolves as

$$G|\psi\rangle = \cos\frac{3\theta}{2}|\alpha\rangle + \sin\frac{3\theta}{2}|\beta\rangle. \tag{2.19}$$

This implies that the state $|\psi\rangle$ is rotated towards $|\beta\rangle$ by an angle θ for one iteration of the Grover operator, as shown in Fig. 2.10.

After k iterations the resulting state is

$$G^k|\psi\rangle = \cos\frac{(2k+1)\theta}{2}|\alpha\rangle + \sin\frac{(2k+1)\theta}{2}|\beta\rangle. \tag{2.20}$$

Thus each iteration rotates the state further towards $|\beta\rangle$ by an angle θ. The total number of iterations R to get close to β before measurement is given by $R \leq \lceil \frac{\pi}{2\theta} \rceil$, and $\theta/2 \geq \sin\theta/2 = \sqrt{M/N}$. Therefore $R \leq \lceil (\pi/4)\sqrt{N/M} \rceil$, or $R = \mathcal{O}(\sqrt{\frac{N}{M}})$, leading to a quadratic speedup when compared to a classical algorithm that requires $\mathcal{O}(N)$, database reads.

2.5.2 Exponential speedup and modifications of the search algorithm

Many quantum algorithms (most notably the factorization algorithm) provide an exponential speedup; a natural question to ask is whether it is possible to accelerate the search problem beyond the quadratic speedup. In this section, we present a search algorithm which apparently would make the standard Grover search algorithm faster. Next, we show that this modification is in conflict with other quantum mechanical concepts, and in doing so, we discover a result that we call impossibility of reflection with respect to an unknown state, which is explained in section 2.5.3.

The schematic circuit of the modified search algorithm is shown in Fig. 2.11, which uses the iteration dependent operator K_l, for the l^{th} iteration, and is defined as $K_l|\psi_{l-1}\rangle = |\psi_l\rangle$. The operator K_l is defined recursively as

$$K_{l+1} = (2|\psi_l\rangle\langle\psi_l| - I)O, \tag{2.21}$$

where initially $|\psi_0\rangle = |\psi\rangle$, the uniform superposition state as defined in equation 2.15. The first iteration is identical to the standard Grover operator, $K_1 = G = (2|\psi\rangle\langle\psi| - I)O$, but starting from the second iteration, the rotation of the state vector is accelerated. The fundamental idea is to use the information contained in $|\psi_k\rangle$ for the $(k+1)^{th}$ iteration. In other words, in the standard Grover algorithm, consecutive reflections are realized with respect to the same state $|\psi\rangle$. But the state vector from the previous iteration is closer to the solution $|\beta\rangle$, so in some sense it contains more information about where the solution is. Thus, by reflecting with respect to the previous vector we would expect to find the solution in a smaller number of steps.

We show that after the step l, the state vector makes an angle $3^l\theta/2$ with the axis $|\alpha\rangle$. This follows immediately by induction.

$$|\psi_1\rangle = K_1|\psi\rangle = G|\psi\rangle = \cos\frac{3\theta}{2}|\alpha\rangle + \sin\frac{3\theta}{2}|\beta\rangle, \tag{2.22}$$

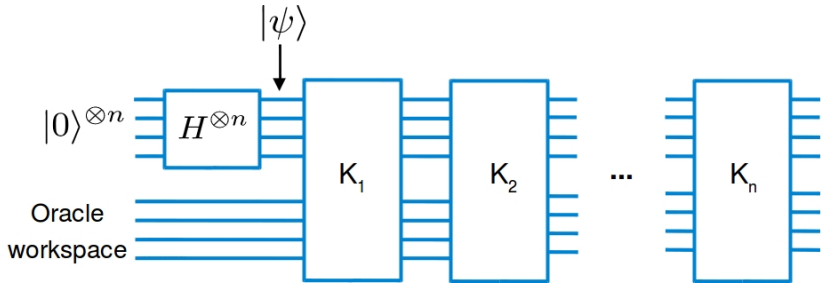

Figure 2.11. Geometrical representation of the modified Grover algorithm.

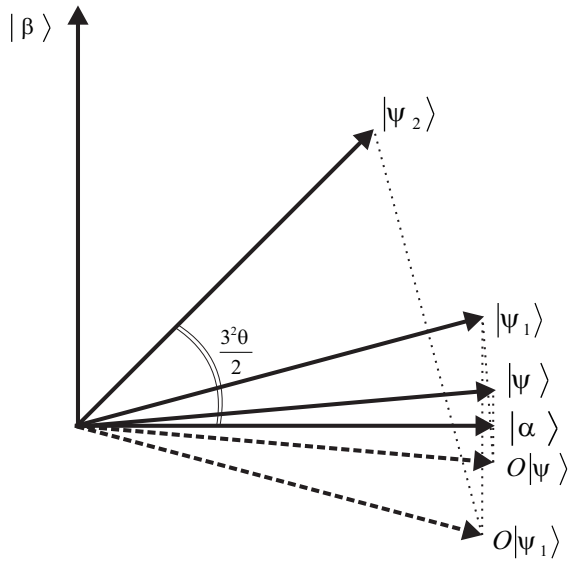

Figure 2.12. State evolution in 2-d for two iterations in the modified search problem, $K_2K_1|\psi\rangle$.

and, if $|\psi_l\rangle = \cos\frac{3^l\theta}{2}|\alpha\rangle + \sin\frac{3^l\theta}{2}|\beta\rangle$, then

$$K_{l+1}|\psi_l\rangle = [2|\psi_l\rangle\langle\psi_l| - I]O|\psi_l\rangle \tag{2.23}$$

$$= [2(\cos 3^l\frac{\theta}{2}|\alpha\rangle + \sin 3^l\frac{\theta}{2}|\beta\rangle)(\cos 3^l\frac{\theta}{2}\langle\alpha| + \sin 3^l\frac{\theta}{2}\langle\beta|) - I] \times \tag{2.24}$$

$$O[\cos 3^l\frac{\theta}{2}|\alpha\rangle + \sin 3^l\frac{\theta}{2}|\beta\rangle] \tag{2.25}$$

$$= \cos 3^{l+1}\frac{\theta}{2}|\alpha\rangle + \sin 3^{l+1}\frac{\theta}{2}|\beta\rangle. \tag{2.26}$$

At each iteration the state which had the initial phase of $\theta/2$ gets rotated towards $|\beta\rangle$ by the angles $3\theta/2, 9\theta/2, 27\theta/2, ...$, up to $\pi/2$. This is a geometric progression, thus one expects an exponential reduction in the number of steps needed. This is geometrically represented in two dimensions in Fig. 2.12.

Now we want to find the number of iterations R_{mod} for our search algo-

rithm; from the equation $\pi/2 = 3^{R_{\rm mod}}\theta/2$, we get $R_{\rm mod} = \log_3 \pi/\theta$, which together with $\sin\theta/2 \approx \theta/2 = \sqrt{M/N}$ gives

$$R_{\rm mod} = \mathcal{O}(\log_3 \sqrt{\frac{N}{M}}). \tag{2.27}$$

Is it possible to make such a construction possible, physically? What prevents the exponential speedup of a search algorithm? We first note that in general the operator $(2|\psi\rangle\langle\psi| - I)$ is unitary irrespective to what $|\psi\rangle$ is; this is expected also from its geometrical interpretation since reflections take a normalized state into a normalized state. The problem arises due to a fundamental limitation of quantum physics that does not allow measuring $|\psi_l\rangle$ fully [17, 18]. Though the algorithm creates the state $|\psi_l\rangle$, at l^{th} iteration, the quantum no-cloning theorem [19] disallows storing the precise quantum information of the state $|\psi_l\rangle$, which is required to construct the gate K_{l+1}.

Approximate quantum cloning techniques and the search problem

There are imprecise cloning techniques, which allow approximate copies of quantum states to be made, and they have been shown to increase the performance of certain quantum tasks [20]. Probabilistic cloning uses postselection to produce perfect clones with a finite probability of success [21], whereas deterministic cloning produces approximate clones with a loss of fidelity [22]. The quality of the clones is quantified by fidelity $0 \leq F \leq 1$, where higher fidelity implies better clones. Here we discuss the possibility of using these two approximate cloning techniques in the context of the modified search problem, where we need to clone the state $|\psi_l\rangle$, in order to construct the operator K_{l+1}.

For simplicity consider the case when $M = 1$, where the search problem has only one solution. Let $|\psi_l\rangle$ be the state that is required to be cloned, in order to construct the operator K_{l+1}. The general structure of these states (both in the standard and the modified version of the Grover algorithm) is

$$|\psi\rangle = \sin\varphi|\beta\rangle + \cos\varphi|\alpha\rangle, \tag{2.28}$$

where $|\beta\rangle$ is the solution state we are searching for. Probabilistic cloning requires that the state $|\beta\rangle$ is linearly independent from the other basis states $|x\rangle$, to successfully clone it with higher probability. In other words, the state $|\beta\rangle$ should be more differentiated from the other states, for a successful cloning. To check for the linear independence of these states, we

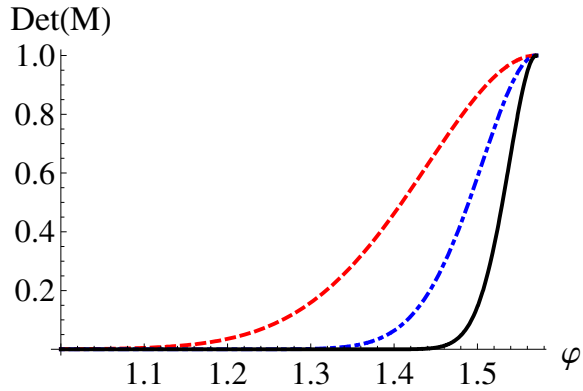

Figure 2.13. The determinant of the matrix M for different-size registers $n = 5$ (dashed), $n = 7$ (dash-dotted), $n = 9$ (continuous).

calculate the determinant of a matrix M with $\sin\varphi$ on the diagonal and $(1/\sqrt{N-1})\cos\varphi$ as the other entries (see Fig. 2.13).

In the Grover search problem, the starting state is the uniform superposition state, so state $|\beta\rangle$ is not differentiated from the other states. This is reflected as the determinant of the matrix M being close to zero in the initial part of the calculations. With more iterations of the Grover operator, the states corresponding to different solutions of the search begin to differentiate with respect to each other due to amplification of the probability amplitude of the solution. This is reflected with the Det(M) increasing in value towards 1. The determinant reaches the value 1, at $\theta = \pi/2$, which corresponds to the case where the required Grover iterations are performed to find the solution to the search problem and hence the state $|\beta\rangle$ is maximally differentiated in its amplitude from the other basis states. It shows that although probabilistic cloning of these states is possible in principle, the smallness of the determinant for most of the angles means that probabilistic cloning can work effectively only in the latest iterations of the search algorithm.

The deterministic cloning technique is universal but produces only approximate copies of the original with a certain fidelity. The trade off is that as the size of the register to be cloned increases, the fidelity of the clones decreases. The search algorithm requires cloning a register of size n. For the case of creating two clones, the fidelity of the two copies with respect to the original is [22]

$$F = \frac{n+3}{2(n+1)}. \tag{2.29}$$

An interesting observation is that even for the case of an infinitely large

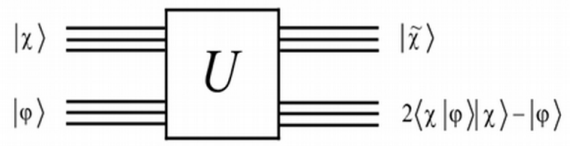

Figure 2.14. Schematic for a universal circuit that performs reflection of one state with respect to the other.

register, in the limit $n \to \infty$ the fidelity is finite, $F = 1/2$. However even for a few steps, the loss of fidelity leads to considerable errors, as the fidelity factor multiplies on cascaded operations.

2.5.3 Impossibility of reflection with respect to an unknown state

Accepting either a loss of fidelity due to approximate cloning, or performing probabilistic cloning with unit fidelity would mean that even after applying the Oracle to the state $|\psi_l\rangle$ we have a copy of $|\psi_l\rangle$ which can be used as a "control" register (n-qubit), in order to implement a projection with respect to it. At first sight, this looks like a simple operation, since we do not attempt to extract all the information from the state $|\psi_l\rangle$ (only the projection ${}_l\langle\psi|\psi\rangle_{l+1}$). Surprisingly however, this cannot be constructed as a universal gate, according to the rules of quantum mechanics.

Now the question is, how to implement the operator, K_{l+1}? The purpose of K_{l+1} is to generate a reflection of $O|\psi\rangle_l$ with respect to $|\psi\rangle_l$, using the clone $|\psi\rangle_l$. The result of this will lead to the state $2_l\langle\psi|\psi\rangle_{l+1}|\psi\rangle_l - |\psi\rangle_{l+1}$. And K_{l+1} is an iteration dependent operator, which requires that such a reflection should be constructed at each iteration. This imposes the requirement of a universal reflection circuit, in contrast to a custom made state specific reflection. Is such a universal reflection circuit possible?

The best starting point for such a reflection circuit is a controlled operation gate, such as the quantum cNOT gate : $|c\rangle|t\rangle \stackrel{\text{cNOT}}{=} |c\rangle|t \otimes c\rangle$. In our case, we need the clone $|\psi\rangle_l$ to act as a "control" and the state $O|\psi\rangle_{l+1}$ would be the target to be modified. In the cNOT, the control qubit is left unchanged after the gate. In our case, since at the next step $(l+2)$ we will not use the wavefunction $|\psi\rangle_l$ anymore, we do not need to necessarily impose that the "control" wavefunction $|\psi\rangle_l$ remains unchanged and can be modified into any wavefunction $|\tilde{\psi}\rangle_l$. Below we show that even in this relaxed form, it is impossible to find a quantum circuit that would perform the desired operation.

The generic operation of the gate we would need is shown in Fig. 2.14, implementing a unitary transformation U. Consider now the action of U on two sets of states $|\chi\rangle|\varphi\rangle$ and $|\chi'\rangle|\varphi'\rangle$,

$$U|\chi\rangle|\varphi\rangle = |\tilde{\chi}\rangle|[2\langle\chi|\varphi\rangle|\chi\rangle - |\varphi\rangle], \tag{2.30}$$

$$U|\chi'\rangle|\varphi'\rangle = |\tilde{\chi}'\rangle|[2\langle\chi'|\varphi'\rangle|\chi'\rangle - |\varphi'\rangle]. \tag{2.31}$$

Taking the adjoint of the second expression and multiplying with the first one we obtain the condition

$$\langle\chi'|\chi\rangle - \langle\tilde{\chi}'|\tilde{\chi}\rangle = 2\left[2\langle\chi'|\chi\rangle|\chi'\rangle\langle\chi| - |\chi'\rangle\langle\chi'| - |\chi\rangle\langle\chi|\right]\langle\tilde{\chi}'|\tilde{\chi}\rangle. \tag{2.32}$$

Let us now multiply Eq. (2.32) by $\langle\chi|$ on the left and by $|\chi\rangle$ on the right. We obtain

$$\langle\chi'|\chi\rangle = \left[2|\langle\chi'|\chi\rangle|^2 - 1\right]\langle\tilde{\chi}'|\tilde{\chi}\rangle. \tag{2.33}$$

Similarly, by multiplying to the left by $\langle\chi|$ and to the right by $|\chi'\rangle$ and using the fact that in general $|\chi\rangle$ and $|\chi'\rangle$ need not be orthogonal, we get

$$\langle\chi'|\chi\rangle = \left[4|\langle\chi'|\chi\rangle|^2 - 3\right]\langle\tilde{\chi}'|\tilde{\chi}\rangle. \tag{2.34}$$

Combining Eq. (2.33) and Eq. (2.34) we get $|\langle\chi'|\chi\rangle|^2 = 1$, which forces the two states $|\chi\rangle$ and $|\chi'\rangle$ to be identical. Thus, we have shown that it is impossible to build a quantum circuit performing the desired operation shown in Fig. 2.12.

2.6 The genetic algorithm

Optimization problems are characterized by contraints that limit the solution range, and objective functions that the solver has to minimize (or maximize). Some real world problems that involve non-linear, discontinuous or nondifferentiable objective functions, become increasingly difficult to solve by traditional numerical methods. Deterministic search methods become computationally expensive when they involve many discrete, continuous or mixed variables. Also when the search database is very large, a global optimum solution cannot be found in a reasonable time. In such instances, search heuristics based on evolutionary algorithms are the best choices. In this context, I will explain how to use the genetic algorithm, which belongs to the class of evolutionary algorithms, to implement multi-qubit quantum gates and hence quantum algorithms.

Evolutionary algorithms start from an initial population of individuals that are mapped to possible solutions. The algorithm moves towards the

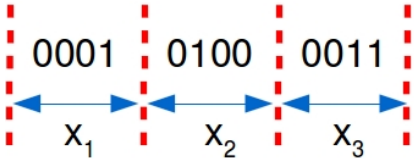

Figure 2.15. Mapping binary information of variables as a chromosome.

optimal solution by applying the Darwinian evolution theory, which is centered on the concept of survival of the fittest. In other words, similar to biological evolution based on the principle of natural selection, the GA 'evolves' the initial population towards the optimal solution through multiple generations. Solutions that do not satisfy the fitness criterion get discarded in the process.

2.6.1 Encoding the genotype

The genetic algorithm starts with an initial population, whose individuals are encoded variables, which are usually represented as a string of binary numbers. Consider that there are n properties that we associate to an individual and each property is represented by a string of l bits; then the individual can be mapped into a design vector of total string length of nl. For illustration, let there be 3 design variables, each represented by 4 binary bits. For simplicity, let the variables have the integer values $x_1 = 1$, $x_2 = 4$ and $x_3 = 3$. Then the chromosome representing the individual is made of 12 bits as shown in Fig. 2.15. Apart from the genotype of the individual, each individual has another attribute called fitness - which quantifies its quality to be the solution, for the search problem. The fitness value is calculated by the fitness function.

A collection of such individuals, encoded to represent information, make the initial population. Care should be taken that the population spans the entire set of search domain. The average distance between individuals is characterised by the attribute *diversity*. A low diversity has a higher possiblility of missing the optimal solution.

2.6.2 How does the genetic algorithm work

The evolution starts from the initial population and progresses in generations. The fitness function evaluates the fitness value of each individual of the current generation. In tandem with the evolutionary theory of natural selection, parents are selected stochastically from the current population,

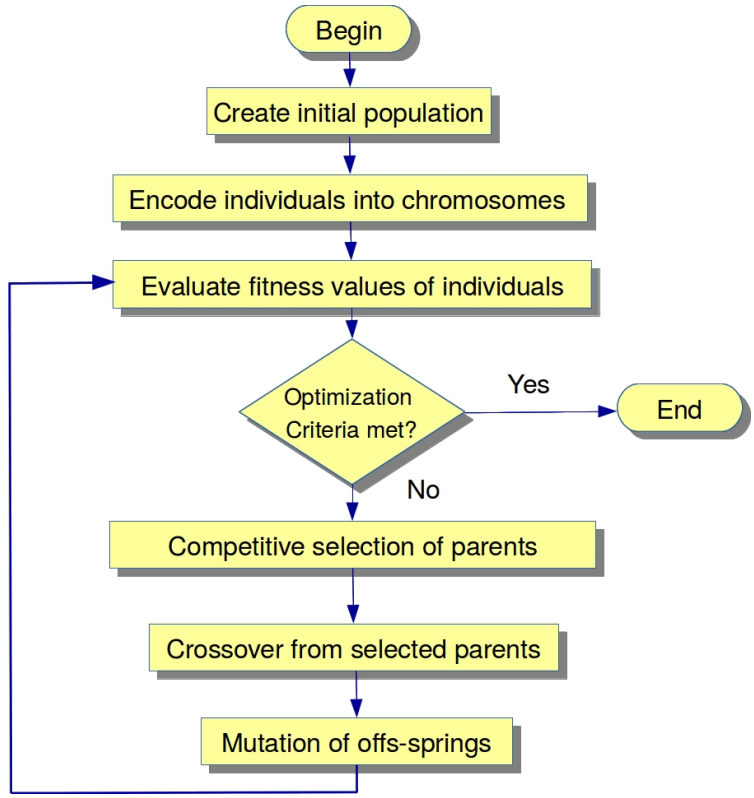

Figure 2.16. Flowchart of a simple genetic algorithm.

such that the best ones survive to create the next generation. New individuals for the next generation are created from recombination of the selected parents. In order to cover all search space, genetically inspired operations such as crossover and mutation is utilized. *Elite children* can also be programmed by cloning the best parent of the current generation into the next generation.

Crossover operation involves choosing a random point in two suitable parents, and swapping the bit strings to form two offsprings. Consider the 12-bit strings, '000101000011' and '100100110001'. Let the random crossover point be 5 bits from the left. The strings are cut into two segments as shown in Fig. 2.17a and the offsprings formed after swapping the bit strings are shown in Fig. 2.17b. The mutation operation involves a random genetic character being inserted into the chromosome. In other words, at a random chosen point, a binary bit is flipped, as shown in Fig. 2.18. Crossover and mutation rates are programmable and tuning these parameters can lead to finding the optimal solution with lower computational time. The general recommendation for most problems is a

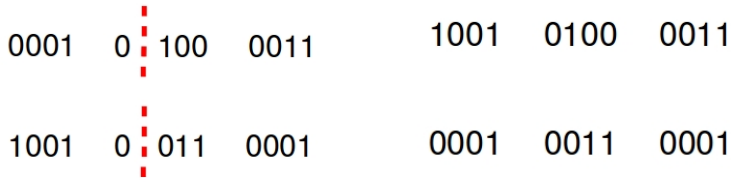

(a) Crossover point selection. **(b)** Crossover children.

Figure 2.17. Schematic of one point crossover.

Figure 2.18. Random mutation in the bit string.

high crossover rate between 60 to 90 percent of the population and a low mutation rate, lower than 1 percent.

The algorithm iterates by calculating the fitness value of the new population. Termination occurs when one of the stopping conditions are met. A successful termination happens when the program stops due to the fitness value of the best individual being better than the specified limit. Other termination conditions that might not ensure a good solution is when the program terminates after iterating over specified number of generations, or specified amount of time. The algorithm also terminates if the fitness value stalls without improvement over a sequence of generations, or amount of time. When the algorithm terminates under theses conditions, an optimal solution is not ensured.

The entire working of the algorithm can be summarized by the simple flow diagram [23] as in Fig. 2.16.

2.7 The genetic algorithm applied for circuit QED

This section explains the usage of genetic algorithm to tailor radio frequency pulses that produce unitary transformation in the circuit QED and other similar architectures. The formulation of pulses corresponding to single and two qubit gates and the corresponding simulation results are presented below.

Single qubit Hamiltonian and pulse design

We start with the simple case of a single qubit. Let ω be the transition frequency of the qubit between $|0\rangle$ and $|1\rangle$ and ω_{RF} is a single tone external drive. The Hamiltonian of this driven two level system is given by (setting $\hbar = 1$)

$$H_{\text{sys}} = \frac{\omega}{2}\sigma^z, \tag{2.35}$$

$$H_{\text{RF}} = \Omega \cos(\omega_{\text{RF}} t + \phi)\sigma^x. \tag{2.36}$$

The effective Hamiltonian is simplified by choosing a rotating frame at ω_{RF} and applying the rotating wave approximation (RWA)

$$H_{\text{eff}} = \frac{\delta}{2}\sigma^z + \frac{\Omega}{2}[\cos(\phi)\sigma^x - \sin(\phi)\sigma^y], \tag{2.37}$$

where the detuning between the drive and qubit transition is $\delta = \omega - \omega_{\text{RF}}$.

Now that we have described the Hamiltonian of the system, qubit gates can be implemented from the Hamiltonian dynamics. The unitary transformation which the genetic algorithm parametrizes using a radio frequency pulse is given by

$$U_{\text{exp}} = \exp(-iH^0_{\text{eff}}\tau_{\text{del}}) \times \exp(-iH_{\text{eff}}\tau_{\text{RF}}), \tag{2.38}$$

where $H^0_{\text{eff}} = \frac{\delta}{2}\sigma^z$.

The objective is to tailor U_{exp} by tuning experimentally controllable parameters so that the state evolution under U_{exp} is equivalent to the target qubit gate. We have used a rectangular pulse for simplicity, as shown in Fig 2.19. The five variables for the evolution of generations in GA are the qubit detuning δ, pulse amplitude Ω, phase ϕ, pulse on-time τ_{RF} and pulse off-time τ_{del}. During τ_{del} the system evolves under its internal Hamiltonian.

For simulation purpose, we choose the single qubit Hadamard gate as the target, which the radio frequency pulse 2.19 should implement.

$$U_T = \frac{1}{\sqrt{2}}\begin{pmatrix} 1 & 1 \\ 1 & -1 \end{pmatrix}. \tag{2.39}$$

In the resonant case and with $\tau_{\text{del}} = 0$, this coincides with the standard quantum optics result for $\pi/2$ pulse with the pulse area $\Omega \times \tau_{\text{RF}}$.

Now that we have parametrised the objective of the optimization problem, we have to define the fitness function to complete the setup of the GA algorithm. The fitness function defines how the fitness value is assigned to each individual of the population, and some penalty functions for unrealistic solutions. We have used a fitness function that calculates fitness values

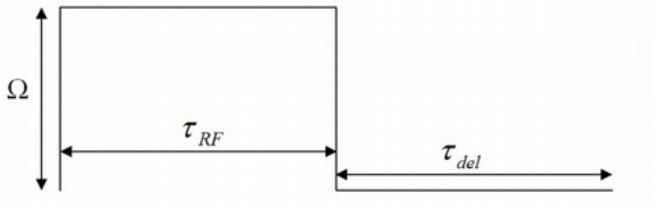

Figure 2.19. A rectangular pulse to implement U_T.

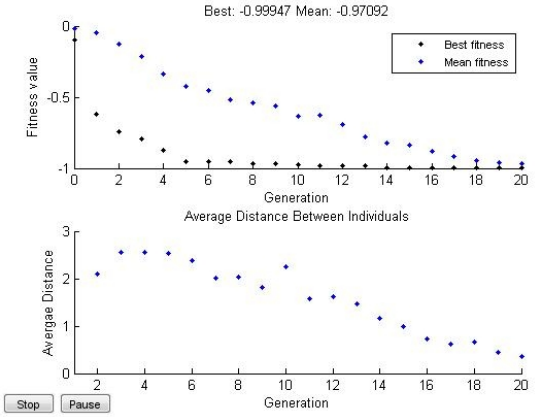

Figure 2.20. Genetic algorithm simulation results for the single qubit Hadamard gate.

as,

$$f = -\{\mathrm{Abs}[\mathrm{Tr}(U_T^{-1}U_{\mathrm{exp}})/2]\}^2. \tag{2.40}$$

This definition for the fitness value limits the value of f to be within $-1 \leq f \leq 0$. When $f = -1$, it means the U_{exp} exactly implements a unitary transformation U_T, and when $f = 0$, it means U_{exp} has no resemblance to U_T.

The algorithm then calculates the fitness value iteratively for each individual of the population for the programmed number of generations. The simulation, for a population size of fifty and evolution for twenty generations for a single qubit Hadamard gate is shown in Fig. 2.20. The simulations are done using Matlab gatool function. For other common single qubit gates such as Pauli-X,Y,Z and phase gates such as S and T gates, the convergence of population to the optimal solution occurred after 10 generations.

Two qubits and a two segment pulse

Universality constructs of Quantum Computation suggest that any unitary operation can be approximated to arbitrary accuracy using Hadamard, phase and cNOT gates. Here we extend the algorithm to a two qubit case

with cNOT as the target gate. The system is characterized by the two transition energies $\omega_{1,2}$, drive frequencies $\omega_{\mathrm{RF1,RF2}}$ with their corresponding drive amplitudes $\Omega_{1,2}$ and phase $\phi_{1,2}$ and the qubit coupling ω^{xx} [24]. The Hamiltonians are given by

$$H_{\mathrm{sys}} = \sum_{j=1,2} \frac{\omega_j}{2}\sigma_j^z, \tag{2.41}$$

$$H_{\mathrm{RF}} = \sum_{j=1,2} \Omega_j \cos(\omega_{\mathrm{RF,j}}t + \phi_j)\sigma_j^x, \tag{2.42}$$

$$H_c = \omega^{xx}\sigma_1^x\sigma_2^x. \tag{2.43}$$

On applying the rotating wave approximation,

$$\begin{aligned} H_{\mathrm{eff}} \quad &= \sum_{j=1,2} \frac{\delta_j}{2}\sigma_j^z + \sum_{j=1,2} \frac{\Omega_j}{2}[\cos(\phi_j)\sigma_j^x - \sin(\phi_j)\sigma_j^y] + \\ &\frac{\omega^{xx}}{2}(\sigma_1^x\sigma_2^x + \sigma_1^y\sigma_2^y) \\ &= H_{\mathrm{eff}}^0 + H_{\mathrm{ext}}, \end{aligned}$$

where $H_{\mathrm{eff}}^0 = \sum_j \frac{\delta_j}{2}\sigma_j^z + \frac{\omega^{xx}}{2}(\sigma_1^x\sigma_2^x + \sigma_1^y\sigma_2^y)$ and $H_{\mathrm{ext}} = \sum_j \frac{\Omega_j}{2}\left[\cos(\phi_j)\sigma_j^x - \sin(\phi_j)\sigma_j^y\right]$.

The target CNOT gate is represented in matrix form as

$$U_T = \begin{pmatrix} 1 & 0 & 0 & 0 \\ 0 & 1 & 0 & 0 \\ 0 & 0 & 0 & 1 \\ 0 & 0 & 1 & 0 \end{pmatrix}. \tag{2.44}$$

In this case, the single segment pulse did not always converge into an optimal solution. So we used a cascaded two segment rectangular pulse defined as

$$U_{\mathrm{exp}} = \prod_{k=1}^{2} U_{\mathrm{seg,k}}, \tag{2.45}$$

where each $U_{\mathrm{seg,k}} = U_{\mathrm{eff,k}}^0 \times U_{\mathrm{eff,k}}$, which are given by

$$U_{\mathrm{eff,k}}^0 = \exp(-iH_{\mathrm{eff,k}}^0\tau_{\mathrm{del,k}}), \tag{2.46}$$

and

$$U_{\mathrm{eff,k}} = \exp(-iH_{\mathrm{eff,k}}\tau_{\mathrm{del,k}}). \tag{2.47}$$

The number of variables per pulse segment is two detunings, two amplitudes, two phases and pulse on-time and off-time, making a total of eight. The two segment rectangular pulse requires a total of sixteen variables. The genetic algorithm evolution is simulated by calling the gatool function in Matlab, and the simulation results are shown in Fig. 2.21.

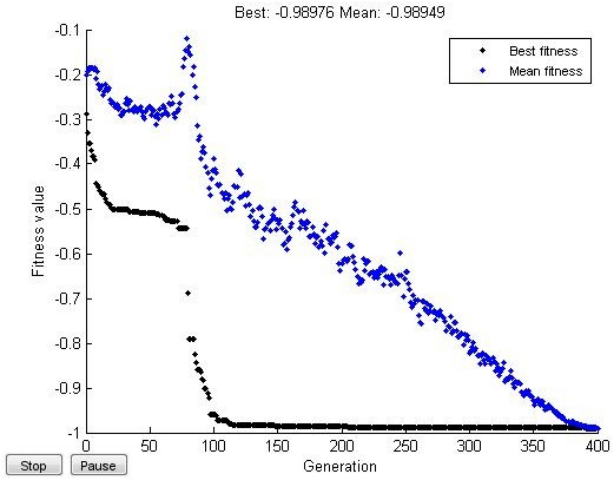

Figure 2.21. Genetic algorithm simulation results for the two qubit cNOT gate.

For other two qubit gates, the population did not always converge to the optimal solution for a single segment pulse. Tailoring a pulse sequence with multiple segments, allowed us to see the convergence towards optimal solution for all the common two qubit gates that we tested.

From the illustration above, it can be seen that the number of optimization parameters increase from 5 in the single qubit case to 16 for the two qubits. As the number of degrees of freedom increases in a quantum circuit, the parameters to manipulate the same become excessively complicated to solve by traditional numerical methods. Falling into the category of global search algorithms, genetic algorithms are optimal candidates for solving the parameters that can effectively manipulate quantum systems.

2.8 Advantages and disadvantages of evolutionary algorithms

Evolutionary algorithms based search is becoming highly useful when the problems are complex and involve non-linear objective functions. In contrast to other search techniques, evolutionary algorithms provide a population that converges towards the solution, which in essence, gives more than one good solution. Evolutionary algorithms are also popular as they are fast in providing an approximate solution. Operators such as *crossover* and *mutation*, ensure that the global search space is covered, in contrast to the local gradient ascent or descent techniques. They can also be programmed into a hybrid technique, where the ouput can be used with the local gradient ascent (or descent) technique, so an exact solution can

be found.

Belonging to the class of heuristic search methods, finding an optimal solution cannot be ensured, and convergence of the population towards the solution is problem oriented. The program might provide a solution with agreeable fitness value, but the parameters may not be suitable to implement for the practical problems. Care should be taken to write penalty functions, so the evolutionary algorithm operates the variables within the range of practical implementation.

3. Circuit quantum electrodynamics

In this chapter, we will discuss circuit quantum electrodynamics (circuit QED). Cavity quantum electrodynamics is the study of light-matter interaction at the quantum level. Circuit quantum electrodynamics borrows techniques from cavity QED, where superconducting circuits replace the atoms and microwave co-planar resonator replaces the cavity. The Josephson junction based "artificial atoms", whose transition energies can be tuned in-situ, offer an opportunity to explore regimes which are beyond those that can be reached with natural atoms. The strong coupling provided by circuit QED is difficult to reach with natural atoms. Being a solid state architecture, employing fabrication techniques such as lithography, circuit QED holds the promise of scalability.

The Jospephson junction is named after the British physicist Brian David Josephson, who predicted in 1962 the current-voltage characteristics across the tunnel junction [25, 26] at low bias voltages (below the superconducting gap). This was a milestone that led to further research in the field of superconducting devices. The SQUID (superconducting QUantum Interference Devices) are Josephson junction based devices that have various applications [27] such as magnetometers and gradiometers. The macroscopic quantum tunneling [28] in Jospephson junctions and the quantum behavior of the the phase across the Josephson junctions (a macroscopic degree of freedom [29]) was first observed by Clarke *et. al.,* [30] which was another milestone which enabled the usage of Josephson junction based devices in the quantum regime.

Here I show how the Josephson junction based devices are ideal candidates to construct a superconducting quantum bit. The fundamental criteria for a quantum system to operate as a qubit are anharmonicity of energy levels and operation temperature below the level spacing, see Fig. 3.1. The anharmonicity allows us to drive transitions only between

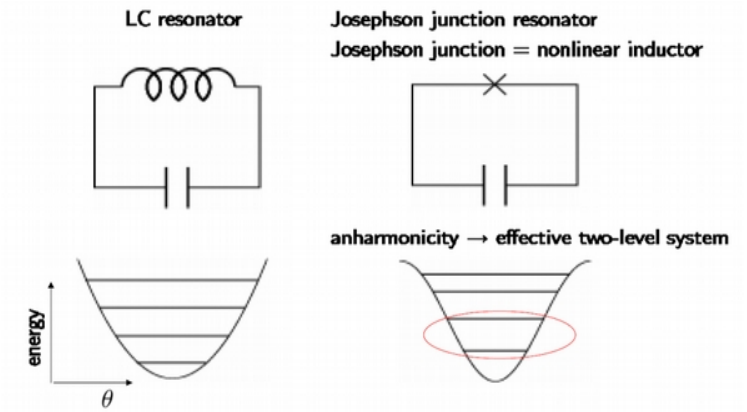

Figure 3.1. Nonlinearity and anharmonicity in a Josephson junction.

selected energy levels. For this reason, a quantum version of a simple harmonic oscillator (a superconducting LC circuit) cannot be used as a qubit.

From the basic Josephson equations $I = I_C \sin\phi$ and $V = \frac{\Phi_0}{2\pi}\frac{\partial\phi}{\partial t}$ and induction law in electrical ciruits $V = -L\frac{dI}{dt}$, it can be seen that the inductance due to the Josephson Junction is given by

$$L_J = \frac{\Phi_0}{2\pi I_c}\frac{1}{\cos\phi}. \tag{3.1}$$

It is straigtforward to see that the dependence of L_J on $\frac{1}{\cos\phi}$ provides it the intrinsic property of non-linearity which led it to be used in Cooper pair box based circuits and thence transmon.

The measurement results shown in this thesis were obtained with a transmon qubit coupled to a quarter wavelength resonator.

3.1 The Cooper pair box

The idea of circuit QED is to make an effective two-level system based on Josephson junctions [31, 32, 33] and to couple it to a one-dimensional coplanar waveguide, acting as a microwave resonator and employed as a readout device. In other words, circuit QED is a solid state approach to cavity QED, where the optical photons in the cavity interact with the artificial atoms.

The transmon is a capacitively-shunted Cooper pair box (CPB) [34]. The idea is to reduce the sensitivity of the standard Cooper pair box to charge noise, by using a large capacitor in parallel with the junctions [35]. To understand the transmon, we start with the explanation of the Cooper

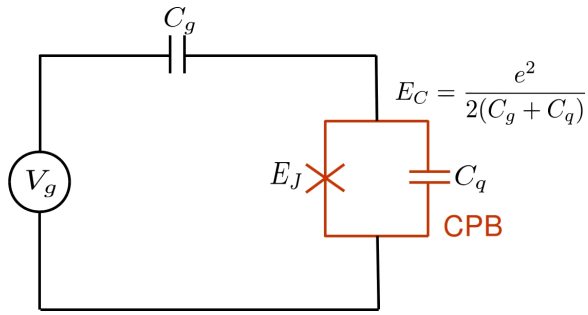

Figure 3.2. Schematic of a Cooper Pair Box

pair box (CPB), see Fig. 3.2 for the schematic. The CPB consists of a superconducting island connected to a reservoir via a Josephson junction in which C_q is the junction capacitance. The relevant parameters of the system are the Josephson energy E_J and the charging energy E_C. E_J represents the energy required for Cooper pair tunneling across the junction, while E_C is the charging energy necessary to add an electron to the island. Furthermore, an effective offset charge $N_g \times (2e) = C_g V_g$ is induced by the gate electrode voltage V_g which is capacitively coupled via C_g to the island.

The Hamiltonian of a CPB with discrete charge $n \times (2e)$ in the island is given by [34]

$$H_{\mathrm{CPB}} = 4E_C \left(n - \frac{C_g V_g}{2e} \right)^2 - E_J \cos\theta, \tag{3.2}$$

with charging energy $E_C = e^2/2C_\Sigma$ and $C_\Sigma = C_q + C_g$. For $E_J/E_C \ll 1$, the CPB is in the charge regime. In this regime the states of the CPB are almost pure charge states with avoided crossings between two charge states due to the Josephson coupling. The minimum energy difference between the levels at the avoided crossing is equal to E_J.

3.2 Split geometry

Another variation of the single CPB is the split CPB design, made up of two Josephson junctions in parallel. Let E_{J1} and E_{J2} be the Josephson energies of the two junctions respectively. This design offers the freedom of in-situ tuning of energy levels by controlling the flux that flows through the loop.

The Hamiltonian due to the Josephson component of the SQUID loop can be written as

$$H = -E_{J1} \cos\phi - E_{J2} \cos\left(\phi + \frac{2\pi\Phi}{\Phi_0} \right), \tag{3.3}$$

where ϕ is the superconducting phase difference across junction 1, and

$\Phi_0 = 2e/h$ is the magnetic flux quantum. With trigonometric identities, the Hamiltonian can be rewritten as

$$H = -E_{J\Sigma}\cos\left(\frac{\pi\Phi}{\Phi_0}\right)\sqrt{1+d^2\tan^2\left(\frac{\pi\Phi}{\Phi_0}\right)}\cos(\phi-\phi_0), \tag{3.4}$$

where $E_{J\Sigma} = E_{J1}+E_{J2}$ is the total Josephson energy, $d = (E_{J1}-E_{J2})/(E_{J1}+E_{J2})$ describes the asymmetry between junctions, and ϕ_0 is given by $\tan(\phi_0+\frac{\pi\Phi}{\Phi_0}) = d\tan(\frac{\pi\Phi}{\Phi_0})$. When the junction asymmetry is small, typically $d \lesssim 0.1$, the two junction loop behaves like a single junction with a flux-dependent Josephson energy,

$$E_J(\Phi) \simeq E_{J\Sigma}\cos\left(\frac{\pi\Phi}{\Phi_0}\right). \tag{3.5}$$

From equation (3.5), it is straightforward to see that the effective Josephson energy between the islands can be tuned by an external magnetic flux.

3.3 The transmon qubit as an artificial atom

The primary problem in a CPB is that the coherence time is largely affected by the fluctuations in N_g due to $1/f$ charge noise. When the charging energy is much larger than the Josephson energy $E_C \gg E_J$, the CPB eigenstates are essentially charge states. In this regime, the term $4E_C(n-N_g)^2$, gives rise to parabolic energy levels as a function of the gate charge N_g. The Josephson energy lifts the degeneracy between charge states which is popularly called as "avoided crossings". The interesting aspect to note is that at the half-integer values of N_g, the transition energies are also first-order insensitive to fluctuations in N_g; this is called a “sweet-spot”. The energy spectrum of the CPB is highly anharmonic, so one can construct a two level approximation that treats the lowest two levels of the CPB as an effective spin-1/2 system.

The idea of a transmon qubit is to introduce a modification to the standard CPB by adding a shunt capacitance in parallel to the Josephson junctions thereby lowering E_C. As the fraction E_J/E_C increases, the curves broaden out and the energy spectrum becomes less sensitive to charge fluctuations. Defining the charge dispersion as the spread in transition energy between adjacent energy levels,

$$\epsilon_m = E_{m,m+1}(n_g = 1/2) - E_{m,m+1}(n_g = 0), \tag{3.6}$$

where $E_{ij} = E_j - E_i$ is the energy difference between levels i and j, then

the residual charge dispersion decreases with increasing E_J/E_C as,

$$\epsilon_m \sim E_C \exp(-\sqrt{8E_J E_C}). \tag{3.7}$$

The charge dispersion drops exponentially with increase in E_J/E_C and when $E_J/E_C \approx 50$ the energy separation between the ground and excited state of the qubit becomes virtually insensitive to charge.

The transition energy between the ground and the excited state can be approximated by

$$\hbar\omega_q = \sqrt{8E_C E_{J\Sigma}\left|\cos(\frac{\pi\Phi}{\Phi_0})\right|} - E_C. \tag{3.8}$$

Equation (3.8) is used for designing E_J and E_C during fabrication, so that the qubit frequencies can be planned to be within the required range for experimentation.

There are additional effects due to the modification of the E_J/E_C ratio. It also affects the anharmonicity of the qubit. The anharmonicity α is defined as the difference between adjacent transition energies. For operation as a qubit, the bottom three levels play a significant role. Considering only the three lower levels,

$$\alpha = E_{12} - E_{01}. \tag{3.9}$$

The anharmonicity is only algebraic in E_J/E_C, whereas the charge dispersion drops exponentially with E_J/E_C. As $E_J/E_C \to \infty$, the anharmonicity asymptotically approaches $\alpha \sim E_C$. A typical transmon has $E_C \sim 300$ MHz, which provides sufficient anharmonicity for fast manipulation of the transmon state. This allows the transmon to be treated as a qubit for quantum information processing.

The Jaynes Cummings Hamiltonian

In circuit QED the combined system of a superconducting qubit and a resonator is best described by the Jaynes-Cummings Hamiltonian [36]

$$H = \hbar\omega_r(a^\dagger a + 1/2) + \frac{\hbar\omega_q}{2}\sigma_z + \hbar g(a + a^\dagger)\sigma_x, \tag{3.10}$$

with $\hbar\omega_q$ the energy difference between the lowest two eigenstates of the qubit, ω_r the resonator frequency, and g the coupling strength between a resonator photon and a qubit excitation. Writing $\sigma_x = \sigma_+ + \sigma_-$ and making the rotating wave approximation (RWA) to eliminate counter-rotating terms ($a^\dagger\sigma_+$ and $a\sigma$), the Jaynes-Cummings Hamiltonian reads

$$H = \hbar\omega_r a^\dagger a + \frac{\hbar\omega_q}{2}\sigma_z + \hbar g(a\sigma_+ + a^\dagger\sigma_-). \tag{3.11}$$

The ground state of the system is defined as $|0_q, 0_r\rangle$, where 0_q represents the ground state of the qubit (1_q would be the first excitation *etc.*) and 0_r indicates no photons in the cavity. The operator $\sigma^- a^\dagger$ transfers $|1_q, n_r\rangle$ to $|0_q, n_r + 1\rangle$ and $\sigma^+ a$ realizes the inverse of this transition.

Treating the circuit QED system in the simple JC Hamiltonian form allows one to solve analytically for the dressed eigenstates

$$|n, +\rangle = cos(\theta_n)|n-1, e\rangle + sin(\theta_n)|n, g\rangle, \tag{3.12}$$

$$|n, -\rangle = -sin(\theta_n)|n-1, e\rangle + cos(\theta_n)|n, g\rangle, \tag{3.13}$$

and eigenenergies

$$E_0 = \frac{\hbar\Delta}{2}, \tag{3.14}$$

$$E_{n,\pm} = n\hbar\omega_r \pm \frac{\hbar}{2}\sqrt{4g^2 n + \Delta^2}, \tag{3.15}$$

where $\Delta = \omega_q - \omega_r$ is the detuning between the qubit and cavity, and θ_n is given by

$$\tan(2\theta_n) = \frac{2g\sqrt{n}}{\Delta}. \tag{3.16}$$

3.3.1 Strong dispersive and resonant regime in circuit QED

The transmon system is said to be in the strong coupling regime, when the coupling between the qubit and the resonator is greater than their decay rates. The decay of the photons from the cavity is predominantly due to the finite cavity life-time, *i.e.,* the photons leak from the cavity due to radiative or dielectric loss. The combined mechanisms are characterized by the cavity decay rate, say κ. Similarly, the energy stored in the qubit also decays, with rate γ. When the coupling strength g between the qubit and the resonator is such that $g > \gamma, \kappa$, they are said to be in the strong coupling regime. In the strong coupling regime, even single excitations in the qubit or cavity exert a strong influence on each other [37].

When the qubit and cavity are in resonance, i.e., $\omega_r = \omega_q$, then $\theta_n = \pi/4$ and the eigenstates are

$$|n, \pm\rangle = (|n-1, e\rangle \pm |n, g\rangle)/\sqrt{2}, \tag{3.17}$$

$$E_{n,\pm} = n\hbar\omega_r \pm \hbar g\sqrt{n}. \tag{3.18}$$

This situation is depicted schematically in figure 3.3a. From equation (3.17), it can be seen that the eigenstates are an equal superposition of qubit and cavity excitations. Equation (3.18) shows a splitting $2\hbar g\sqrt{n}$ in their eigenenergies, which arises as the degeneracy is lifted due to

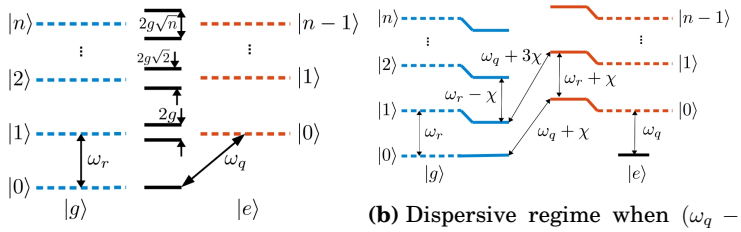

(a) Resonant regime when $\omega_r = \omega_q$ **(b)** Dispersive regime when $(\omega_q - \omega_r) \gg g$

Figure 3.3. Energy level diagram of the Jaynes-Cummings Hamiltonian

the coupling between eigenstates. This $\sqrt{n}$ scaling has been observed spectroscopically up to two photons [38] and six photons [39].

The second case is the dispersive regime where the qubit and cavity are so far detuned in frequency that they can no longer directly exchange energy. Instead, the dispersive interactions between the qubit and cavity cause a slight shift in their energy levels. When $g/\Delta \ll 1$, the Jaynes-Cummings Hamiltonian can be expanded in powers of (g/Δ) to second order as

$$H^{'} \simeq \hbar(\omega_r + \chi\sigma_z)a^{\dagger}a + \frac{\hbar}{2}(\omega_q + \chi)\sigma_z \tag{3.19}$$

where $\chi = g^2/\Delta$. This shows that the cavity frequency is qubit-state dependent, $\omega_r^{'} = \omega_r \pm \chi$ and the qubit transition frequency is renormalized by the Lamb shift, $\omega_q^{'} = \omega_q + \chi$. The dispersive shift of the energy levels of the system is depicted schematically in figure 3.3b. The qubit-state dependent cavity frequency provides a means to perform non-destructive readout of the qubit state [40]. This is the technique used for qubit measurements throughout this thesis.

3.4 Anharmonicity in circuit QED architecture

In this section we discuss the nonlinear effects that arises in the strong dispersive regime and proceed towards the behavior of the system when the cavity is driven at high power. As mentioned in the previous section, the strong dispersive regime is characterised by the detuning $\Delta = \omega_q - \omega_r$ between the qubit and cavity being larger than their coupling $g \ll \Delta$. In the dispersive limit, the dipole interaction can be treated as a perturbation and the Jaynes-Cummings Hamiltonian (3.10) can be expanded in powers of g/Δ up to 2nd order, as shown in equation (3.19). The effect of the photon number in the cavity on the qubit is observed by just regrouping

the Hamiltonian (3.19) as

$$H^{'} \simeq \hbar\omega_r a^\dagger a + \frac{\hbar}{2}(\omega_q + \frac{2g^2}{\Delta}a^\dagger a + \frac{g^2}{\Delta})\sigma_z. \tag{3.20}$$

From equation (3.20) it can be seen that the qubit transition frequency is sensitive to the photon number. Fluctuations in the same will lead to change in the qubit precession frequency, which amounts to dephasing noise and in broadening of the qubit linewidth. This can be experimentally seen by checking the qubit linewidth at low and high measurement power. At low measurement power, there are a few photons in the cavity and the qubit lineshape is Lorentzian with a width determined by qubit relaxation and dephasing rate. At high measurement power, the qubit shifts to higher frequency. When the shift per photon is smaller than the qubit linewidth, the individual peaks corresponding to photon number cannot be resolved, and the qubit spectrum observed has a Gaussian shape.

An interesting phenomenon is observed in the strong dispersive regime, when the Stark shift per photon gets larger than the qubit and cavity relaxation rates, *i.e.*, $2g^2/\Delta > \gamma, \kappa$. When the qubit transition frequency is shifted by more than its linewidth due to one photon entering the cavity, individual photons can be resolved [41]. Thus the qubit spectrum in the strong dispersive regime exemplifies the quantized nature of light.

So far we have discussed a coupled qubit-resonator system when the JC Hamiltonian is expanded to second order. But this is the result from the treatment of the approximate Hamiltonian (3.20). What happens if the cavity is driven at much higher power? Will the 2nd order approximation of Jaynes-Cummings Hamiltonian describe the results obtained in the circuit QED system? Expanding JC Hamiltonian to the fourth order, and solving for the eigenenergies [42], gives

$$\frac{E_{\pm,n}}{\hbar} = n\omega_r + \frac{\omega_q}{2} \pm (\frac{\Delta}{2} + n\frac{g^2}{\Delta} - n^2\frac{g^4}{\Delta^3}), \tag{3.21}$$

and the resonator transition frequency becomes dependent on the photon number

$$\omega_{r,n} = \frac{E_{\pm,n+1} - E_{\pm,n}}{\hbar} = \omega_r \pm \frac{1}{2}(\frac{g^2}{\Delta} - \frac{g^4}{\Delta^3} - 2n\frac{g^4}{\Delta^3}), \tag{3.22}$$

thereby making the cavity anharmonic. This effect in the strongly driven dispersive regime is used to achieve a scheme for high fidelity readout of the qubit state [43].

3.4.1 Measurement results and discussion

We have observed some interesting results in a strongly driven superconducting resonator capacitively coupled to a superconducting qubit (a transmon). The resonator is driven by a tone at a fixed frequency, while at the same time it is monitored by a weak probe field. At relatively high average number of quanta in the resonator, it displays standard nonlinear behavior such as bistability and bifurcation; but, if the average number of photons is increased even further, the linear response is regained. We show that the experimental results match the theoretical models based on the two-level approximation for the transmon (the Jaynes-Cummings models) and on multiple-levels extensions. We also confirm previous results for single-tone driving showing that the bistability region depends in general on the state of the qubit [44, 45].

Semiclassical treatment

Here we will briefly present the semiclassical approach proposed by Girvin *et. al.* [44]. The Hamiltonian of the dispersive Jaynes-Cummings system along with driving at frequency ω_d and amplitude A_d reads

$$H = \omega_c a^\dagger a + \frac{\omega_0}{2}\sigma_z + g(a\sigma_+ + a^\dagger\sigma_-) + \frac{A_d}{\sqrt{2}}\cos(\omega_d t)(a + a^\dagger), \tag{3.23}$$

Lets define N, the total the total number of excitations in the system as

$$N = a^\dagger a + \frac{1}{2}\sigma_z + \frac{1}{2}, \tag{3.24}$$

and $\Delta = \omega_0 - \omega_c$, the detuning between the cavity and the qubit. Now we make the transformation $T^\dagger H T$ to decouple the qubit and cavity. The unitary operator T is defined as

$$T = \exp[-\theta(4N^{-1/2})(a\sigma_+ - a^\dagger\sigma_-)], \tag{3.25}$$

where

$$\sin\theta = \frac{2gN^{1/2}}{\Delta\sqrt{1 + \frac{4g^2}{\Delta^2}N}}, \tag{3.26}$$

$$\cos\theta = \frac{1}{\Delta\sqrt{1 + \frac{4g^2}{\Delta^2}N}}. \tag{3.27}$$

In the semiclassical approximation a classical variable $A = \sqrt{X^2 + P^2} = \sqrt{2a^\dagger a}$ is introduced, where X and P are treated as numbers [44]. This yields

$$A^2 = \frac{\omega_c^2 A_d^2}{[\omega_d^2 - (\omega_c - \chi(A)^2)]^2 + \kappa^2\omega_d^2}, \tag{3.28}$$

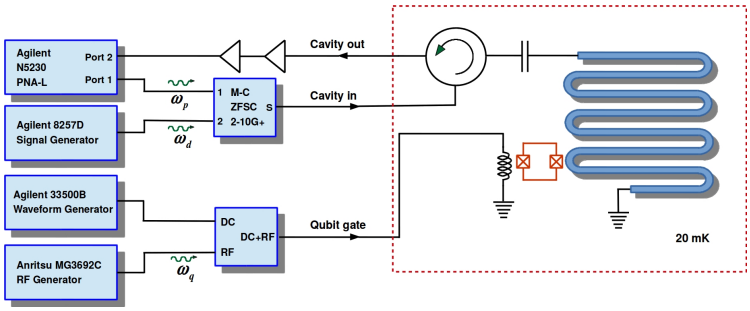

Figure 3.4. Schematic of the measurement setup of qubit induced nonlinearity.

where

$$\chi(A) = -\sigma_z \frac{g^2}{\Delta\sqrt{1+\frac{2g^2}{\Delta^2}(A^2+\sigma_z)}}. \tag{3.29}$$

The cavity frequency is shifted by $\chi(A)$ and only one of the solutions for A^2 is real. The strongly driven JC system is probed and is represented by the simple Hamiltonian

$$H = (\omega_c - \chi(A))a^\dagger a + A_p \cos(\omega_p t)(a + a^\dagger). \tag{3.30}$$

In a rotating frame at ω_p

$$|\langle a\rangle|^2 = \frac{(A_p/2)^2}{(\omega_c - \chi(A) - \omega_p)^2 + (\kappa/2)^2}. \tag{3.31}$$

Experimental setup and results

The harmonic oscillator investigated here is realized as a $\lambda/4$ section of a coplanar waveguide, with one end capacitively out-coupled to a transmission line and the other end shorted to the ground plane of the sample, see Fig. 3.4. This forms a microwave cavity with bare resonant frequency $\omega_c = 4.114\text{GHz}$. The qubit is the transmon described in section 3.3. The resonator is pumped by a strong microwave tone ω_d, which creates a large average number population of photons. To investigate the system, we use an additional small-amplitude microwave probe tone ω_p whose frequency is swept in a range of a few tens of MHz around the resonant frequency of the cavity. The cavity is driven strongly by a second tone, and the driving power of the second tone ranges from -35 dBm to 5 dBm using the radio frequency generator (cryogenic and room temperature attenuation ~ -90 dB).

Figure 3.5 shows experimental results when the cavity is weakly probed in the frequency range of 4.11 to 4.12 GHz. The cavity is driven by a second tone at 4.119 GHz. The qubit transition frequency is at 3.22 GHz, which

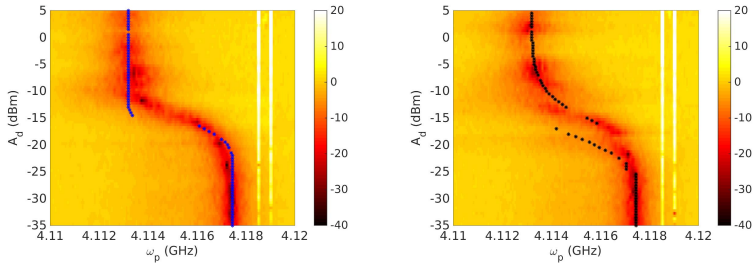

(a) Qubit in ground state.

(b) Qubit saturated by a continuous tone applied at the transition frequency.

Figure 3.5. The effect of the qubit in the ground **(a)** and excited state **(b)** is noticeable at the region of bifurcation. The simulation also reflects this feature (shown as dots on the measurement plot).

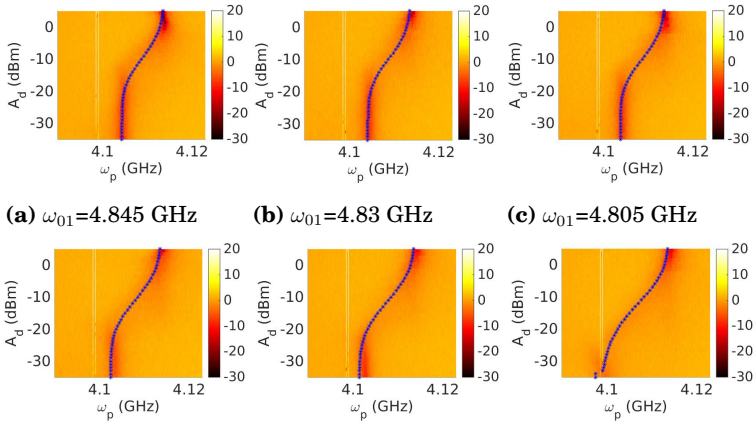

(a) ω_{01}=4.845 GHz **(b)** ω_{01}=4.83 GHz **(c)** ω_{01}=4.805 GHz

(d) ω_{01}=4.73 GHz **(e)** ω_{01}=4.68 GHz **(f)** ω_{01}=4.55 GHz

Figure 3.6. Nonlinear response of a strongly driven cavity at different cavity-qubit detuning. The dots represent the simulated data obtained using equation (3.31).

ensures that the transmon system is in the dispersive regime. The onset of nonlinearity is observed with increasing the drive power, and the effect of qubit in ground (Fig. 3.5a) and excited states (Fig. 3.5b) is noticeable at the region of bifurcation. The cavity response saturates to the bare resonator frequency on further increasing the driving power. In all the measurement plots of this thesis (such as Fig. 3.5), the colorbar represents the reflection amplitude of the cavity probe signal, $|S_{11}|$ unless otherwise stated.

In Fig. 3.6 we present the experimental data where the cavity is strongly driven at a fixed frequency, 4.099 GHz. The cavity-qubit detuning is varied by changing the flux bias of the qubit. A coupling strength of g = 83.8 MHz, is used for simulations. Next in Fig. 3.7 we show the experimental data

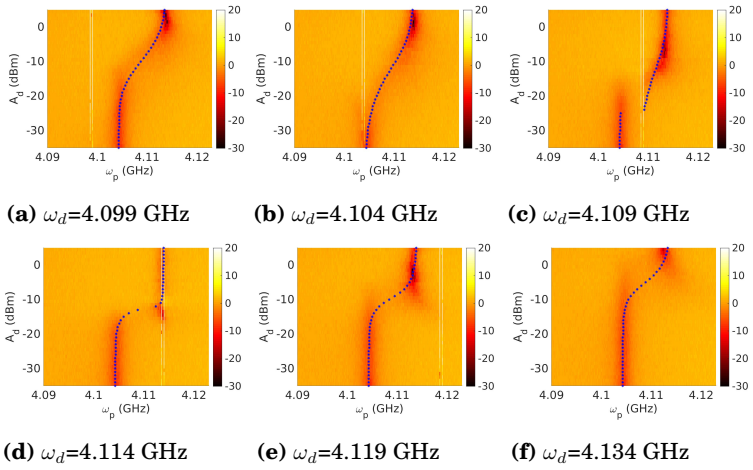

(a) ω_d=4.099 GHz **(b)** ω_d=4.104 GHz **(c)** ω_d=4.109 GHz

(d) ω_d=4.114 GHz **(e)** ω_d=4.119 GHz **(f)** ω_d=4.134 GHz

Figure 3.7. Nonlinear response of a strongly driven cavity at different driving tones. The dots represent the simulated data obtained using equation (3.31).

with qubit frequency fixed at 4.845 GHz and the cavity drive tone varied. A coupling strength of g = 83.8 MHz, is used for simulations.

When the cavity is driven at low amplitude, the cavity response is as expected with a dispersively shifted cavity frequency $\omega_c - g^2/\Delta$. On increasing the driving to intermediate values, the cavity enters the bistability region where the quantum noise causes switching between the two semiclassical solutions. Finally for the strongest driving, the cavity regains linear behavior with a strong resonance at the bare resonant frequency ω_c ($\lim_{A\to\infty} \chi(A) = 0$). The critical amplitude at which the resonator enters bistability is proportional to the detuning between the cavity drive tone and the bare cavity frequency $\omega_d - \omega_c$ [45]. This is also observed in the experimental data and the simulation results (eq. 3.31), as shown in Fig. 3.7.

3.5 Summary

This chapter starts by explaining circuit QED as a suitable experimental platform for operation as a qubit utilizing the Josephson junction based two-level systems coupled to the one-dimensional coplanar waveguide resonator. The nonlinearity in the artificial atom is essential to specifically address the two lowest energy levels. The chapter moves from discussing the fundamentals of Cooper pair box to the transmon qubit. Increasing the E_J/E_C ratio makes the transmon insensitive to charge noise while still retaining anharmonicity to operate as an effective two-level system.

The chapter finishes by presenting the experimental results showing the nonlinear effects observed in a strongly driven Jaynes-Cummings oscillator. This work is still under study and we are currently exploring the effects of a multi level transmon on the strongly driven resonator. A more complete theory based on multilevel dressed states has been recently developed by our collaborators in Oulu, and preliminary fittings with our data suggest that it can be used to fully simulate our results.

Circuit QED offers two major advantages: First, being a solid state architecture employing fabrication techniques such as lithography, it offers the promise of scalability. Second, the Josephson junction based artificial atoms have transition energies that can be tuned in-situ, by varying the flux that flows through the SQUID loop. What happens if we subject the transmon qubit to periodic flux modulation? The next chapter presents our research pertaining to this question.

4. Spectrum of a transmon under frequency modulation

Dynamical averaging and modulation experiments have a very long history and Floquet theory has been widely used to describe the experimental results. The Floquet picture provides a semiclassical treatment of the quantum system coupled to a classical driving field. This treatment is useful for the case of strong driving allowing the classical treatment of the driving field. This treatment is so robust that there exists scientific literature spanning more than half a century that uses the Floquet picture: from the Autler-Townes effect [46] in 1955, an elaborate treatment of the problem of solving a Schrödinger equation with a Hamiltonian periodic in time by Shirley [47] in 1965, to studies of the dressed states of a superconducting qubit subject to extreme driving by Delsing *et.al.,* in 2007 [48].

This chapter focuses mainly on frequency domain measurements performed on a transmon qubit. Starting from the single tone and two tone measurements that used to characterize a transmon qubit, the chapter progresses presenting the effects of modulating the transition frequency of qubit and the resulting Stückelberg interference patterns observed.

4.1 Single tone measurement

A general result in quantum physics is that interaction or a perturbation lifts the degeneracy of a Hamiltonian with degenerate eigenvalues. For a two-level system, this phenomenon is refered to as avoided crossing of energy levels. One illustration of this in the Cooper pair box is presented in Chapter 3.1, where the introduction of tunelling energy E_J leads to avoided crossings at the intersections of the parabolic charge dispersion curves.

It has also been explained in section 3.2 that the transmon can be used as an artificial atom whose transition energies can be tuned in-situ by

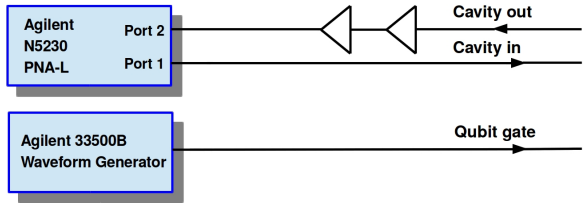

Figure 4.1. Schematic of the one-tone measurement setup.

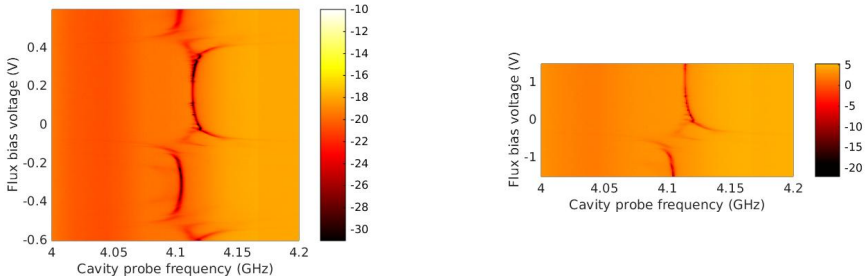

Figure 4.2. One tone measurement results : a) shows the periodicity with respect to the flux quanta, b) is a detail of one avoided crossover.

controlling the flux penetrating the SQUID loop. A similar effect is observed when the qubit crosses the cavity frequency. The measurement of this avoided crossing between the cavity and the qubit is known as single tone measurement in circuit QED, as it involves only one frequency source irradiating the one-dimensional coplanar waveguide cavity resonator, as a probe to the system.

The measurement setup is shown in Fig. 4.1. and the measurement results are shown in Fig. 4.2.

4.2 Two tone measurement

The flux dependence of the qubit in the dispersive regime is obtained from the two tone measurement, so named, as there are two frequency sources: one which excites the qubit and one that probes the cavity. The dispersive shift of the cavity due to the qubit in excited state is seen as the flux dependent curve in the spectrum.

The measurement setup is shown in Fig. 4.3 and a typical measurement result is as shown in Fig. 4.4.

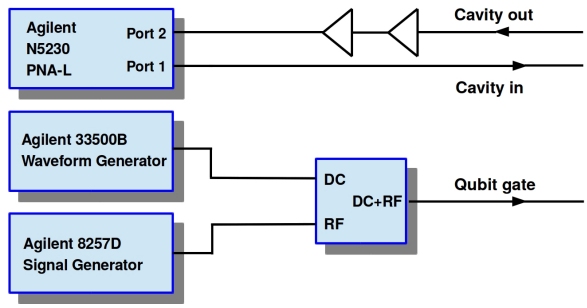

Figure 4.3. Schematic of two-tone measurement setup.

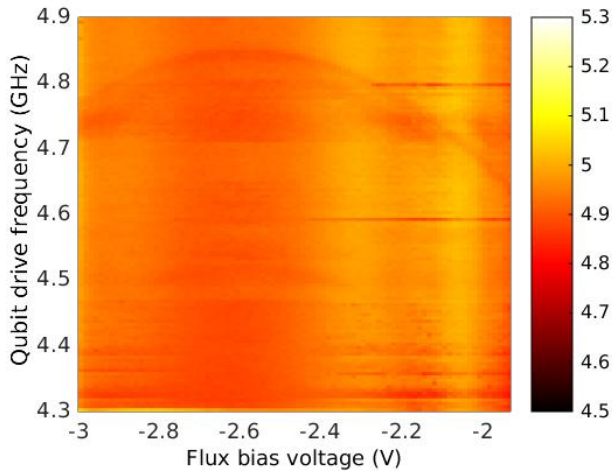

Figure 4.4. Two-tone spectroscopy for a qubit with the transition frequency higher than the cavity frequency ($\omega_r/2\pi = 3.795\text{GHz}$).

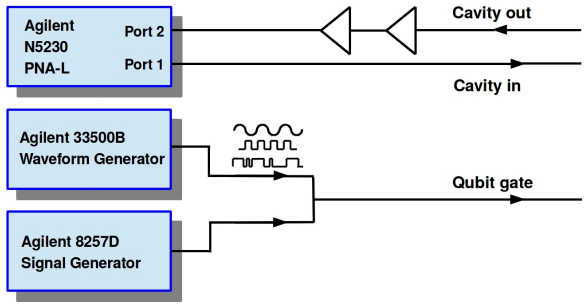

Figure 4.5. Schematic of the setup for modulating the energy splitting of the qubit in the longitudinal direction, with an additional drive in the transverse direction.

4.3 Modulating the transition frequency of the qubit

Interesting interference patterns have been observed in the spectrum of a modulated qubit system such as the Landau-Zener (LZ) interference. The LZ formula, obtained independently in 1932 by Lev Landau, Clarence Zener, Ernst Stueckelberg, and Ettore Majorana, is an approximate solution for the equation of motion of a 2-level quantum system for the case when the energy separation of the two states varies linearly in time [49]. In the circuit QED system, the transition frequency can be tuned in-situ through the flux bias of the transmon. So the cQED setup is best suited to study the modulation effects of the transition energy. In the following sections, we report the effects when the flux is modulated by sinusoidal, periodic latching and random telegraph noise.

The sample used in the experiments is a transmon with single-electron charging energy $E_{\rm C} = e^2/2(C_{\rm G}+C_{\rm B}) \approx h\times 0.35$ GHz, $E_{\rm J} = E_{\rm J1}+E_{\rm J2} \approx 24E_{\rm C}$ is the maximum Josephson energy, and $d = (E_{\rm J1} - E_{\rm J2})/E_{\rm J} \approx 0.11$ denotes the junction asymmetry. We choose $\Phi_{\rm dc}$ so that $\omega_0/2\pi = 2.62$ GHz, which is far detuned from the bare resonator frequency $\omega_{\rm r}/2\pi = 3.795$ GHz, allowing the dispersive measurement of the qubit through the resonator by standard homodyne and heterodyne techniques. The transmon is not a perfectly isolated system and the decoherence parameters have to be measured as well. The relaxation rate $\Gamma_1/2\pi = 1$ MHz is obtained by applying a π pulse and monitoring the exponential decay of the first excited state, and the dephasing rate $\Gamma_2/2\pi = 3$ MHz is extracted from Rabi oscillations and Ramsey interference experiments.

4.3.1 Sinusoidal modulation

The Hamiltonian of a transmon qubit whose energy splitting is modulated sinusoidally is $\hbar[\omega_0 + \delta\cos(\Omega t)]\sigma_z/2$. We also drive the system in the transverse direction at frequency ω, leading to the Hamiltonian

$$\hat{H} = \frac{\hbar}{2}[\omega_0 + \delta\cos(\Omega t)]\hat{\sigma}_z + \hbar g\cos(\omega t)\hat{\sigma}_x. \tag{4.1}$$

Measurements were conducted using the setup shown in Fig. 4.5. On sweeping the amplitude of the longitudinal sinusoidal modulation δ while keeping the modulation frequency Ω fixed, the intereference pattern observed in the measurement is shown in Fig. 4.6. The measurement plot is suggestive of a Landau Zener interference pattern. In the absence of the driving field, standard LZS processes are not possible because the qubit energy separation is one order of magnitude higher than the modulation frequency, and the standard LZS probability is negligibly small. Now, what causes these LZ-like interference patterns? This section is dedicated to the discussion of the interference patterns shown in Fig. 4.6 and 4.7, and shows that it can be interpreted as a photon-assisted Landau-Zener-Stückelberg (LZS) effect.

In the present case, the LZS effect occurs at a modulation frequency close to the detuning between the qubit frequency ω_0 and the driving field ω. It is thus a photon-assisted effect: the energy of the photons from the driving field is used to reduce the separation ω_0 of the bare qubit, and as a result the LZS effect occurs between the dressed states formed by the qubit and the transverse driving field. The transitions occur between dressed states $|\downarrow, n\rangle$ and $|\uparrow, n-1\rangle$, where n refers to the photon number of the transverse driving field. The phase difference of the two states gathered between the consecutive tunneling events leads to either constructive or destructive interference observed as maxima or minima in the occupation probability of the excited state. We start by transforming the Hamiltonian from the equation (4.1) into the frame rotating at ω around the z-axis [unitary transformation $\hat{U} = \exp(-\mathrm{i}\omega\hat{\sigma}_z/2)$], where it has the same form (in the RWA) as that of LZS-interference [49, 50, 51], namely

$$\hat{H} = \frac{\hbar}{2}[\omega_0 - \omega + \delta\cos(\Omega t)]\hat{\sigma}_z + \frac{\hbar}{2}g\hat{\sigma}_x. \tag{4.2}$$

Figure 4.7 shows a rich interference pattern observed experimentally by sweeping the modulation frequency Ω while keeping the modulation amplitude δ constant. The transverse drive was swept across a range of

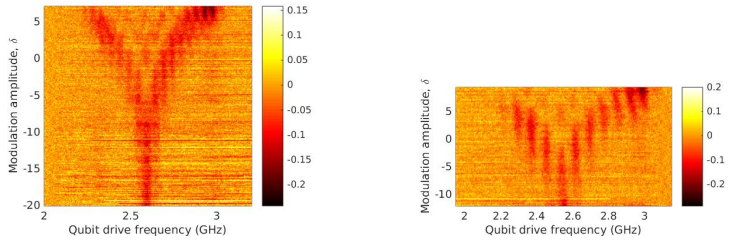

(a) $\Omega = 50\text{MHz}$ **(b)** $\Omega = 80\text{MHz}$

Figure 4.6. The interference pattern observed on sweeping δ while keeping Ω constant.

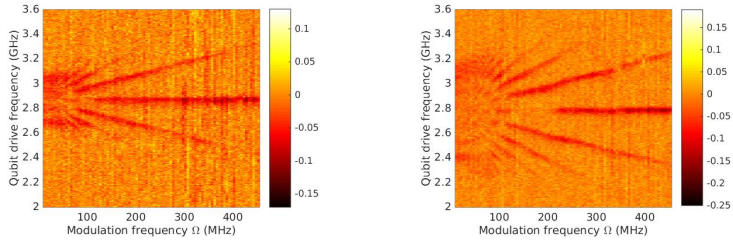

Figure 4.7. A rich sideband observed in the spectrum of a transmon under longitudinal sinusoidal modulation.

frequencies, centered around ω_0, and the cavity response was monitored from the reflected signal using the network analyzer.

These interference patterns can be explained in detail as follows. We start from the multi-photon transition processes associated with the sinusoidally modulated qubit, defined by the Hamiltonian as in equation (4.1). In order to eliminate the time-dependence from the longitudinal drive, the system is moved to a non-uniformly rotating frame with the unitary transformation [52],

$$\hat{U} = \exp\left[-\frac{\mathrm{i}}{2}\left(\omega_0 t + \frac{\delta}{\Omega}\sin\Omega t\right)\hat{\sigma}_z\right], \tag{4.3}$$

the effective Hamiltonian is $\hat{H}' = \hat{U}^\dagger \hat{H}\hat{U} + \mathrm{i}\hbar(\partial_t \hat{U}^\dagger)\hat{U}$, and by using the Jacobi-Anger relations, we get

$$\hat{H}' = \frac{\hbar g}{2}\left(\mathrm{e}^{\mathrm{i}\omega t} + \mathrm{e}^{-\mathrm{i}\omega t}\right)\mathrm{e}^{\mathrm{i}\omega_0 t}\sum_{k=-\infty}^{\infty} J_k\left(\frac{\delta}{\Omega}\right)\mathrm{e}^{\mathrm{i}k\Omega t}\hat{\sigma}_+ + \text{h.c.}. \tag{4.4}$$

When the transverse drive is close to a resonance, that is, $\omega \approx \omega_0 \pm k\Omega$ ($k = 0, 1, 2\ldots$) and that the resonances are resolvable $\Omega > g > \Gamma_2$, we transform back with $\hat{U} = \exp[\mathrm{i}(\omega_0 + k\Omega - \omega)t\hat{\sigma}_z/2]$ and ignore all the fast rotating terms except the resonant terms (rotating wave approximation, RWA). The resulting RWA Hamiltonian reads

$$\hat{H}'_{\text{RWA}} = \frac{\hbar}{2}\left[(\omega_0 + k\Omega - \omega)\hat{\sigma}_z + gJ_k\left(\frac{\delta}{\Omega}\right)\hat{\sigma}_x\right], \tag{4.5}$$

describing, in the Bloch spin representation, precessions around the vector $\mathbf{\Omega} = \left(gJ_k\left(\frac{\delta}{\Omega}\right), 0, \omega_0 + k\Omega - \omega\right)$ with the effective Rabi frequency

$$g_{\text{eff}}^{(k)} = \sqrt{(\omega_0 - \omega + k\Omega)^2 + g^2 J_k^2\left(\delta/\Omega\right)}. \tag{4.6}$$

At the multi-photon resonance $\omega = \omega_0 \pm k\Omega$ ($k = 0, 1, 2\ldots$), the effective Rabi frequency is $|gJ_k(\delta/\Omega)|$. Now we find the steady state occupation probability in the presence of relaxation with rate Γ_1 and decoherence with rate Γ_2 by solving the Bloch equations analytically. The result for the steady state excited state occupation probability is

$$P_{\text{e}} = \sum_{k=-\infty}^{\infty} \frac{\frac{\Gamma_2}{2\Gamma_1}\left[gJ_k\left(\frac{\delta}{\Omega}\right)\right]^2}{\Gamma_2^2 + (\omega_0 - \omega + k\Omega)^2 + \frac{\Gamma_2}{\Gamma_1}\left[gJ_k\left(\frac{\delta}{\Omega}\right)\right]^2}. \tag{4.7}$$

In the non-modulated case, the corresponding expression for the occupations is simply

$$P_{\text{e}} = \frac{\frac{\Gamma_2}{2\Gamma_1} g^2}{\Gamma_2^2 + (\omega_0 - \omega)^2 + \frac{\Gamma_2}{\Gamma_1} g^2}. \tag{4.8}$$

Numerical simulations were also performed using equation (4.7) and the results match the experimental data. This explains the interference pattern as photon-assisted Landau-Zener-Stückelberg (LZS) effect in the present setup of the circuit QED system.

4.3.2 Square wave modulation

This section deals with the measurement of the spectrum of a superconducting qubit under abrupt, square-pulse modulation of the transition frequency. A rich structure of sidebands appears in the experimental spectrum, which is reproduced numerically and also by approximate analytical results. Along each sideband, at specific modulation frequencies, tunneling is either maximized or suppressed by coherent destruction of tunneling. We demonstrate that the sidebands result from Landau-Zener-Stückelberg transitions and interference in the subspace of dressed states formed by the qubit hybridized with a strong transversal driving field. Finally, a detailed comparison with the case of harmonic modulation shows that the information about the shape of the pulse can be extracted from the spectrum at intermediate modulation frequencies.

Here we will demonstrate a number of effects that emerge as a result of repeating the pulses with a period $2\pi/\Omega$. We show that a specific pattern of sidebands appears in the spectrum, which can be understood as a photon-assisted Landau-Zener-Stückelberg (LZS) effect. On each sideband, the transfer to the excited state is suppressed at certain modulation

frequencies, a phenomenon similar to the so-called coherent destruction of tunneling (CDT) [53]. We also demonstrate that we can extract the difference between square-pulse modulation and sine modulation.

The transmon is flux-biased at a constant value $\Phi_{\rm dc}$, on top of which we overlap a time-dependent flux by adding a square wave in the bias coil, $\Phi_{\rm ext} = \Phi_{\rm dc} + \Phi_{\rm sq}(t)$, resulting in time-dependent ω_y and ω_{10}. The measured reflection spectrum together with the corresponding numerical simulations of the dispersive shift is shown in Fig. 4.8. The relevant timescales involved in the square pulse modulation are typically one order of magnitude smaller than the qubit transition frequency. Thus, to a good approximation, the qubit state is the instantaneous value corresponding to $\Phi_{\rm ext}(t)$. Thus ω_y and ω_{10} will be modulated around $\omega_y(\Phi_{\rm dc})$ and $\omega_0 \equiv \omega_{10}(\Phi_{\rm dc})$, leading to $\omega_y = \omega_y(\Phi_{\rm dc}) + \frac{\partial \omega_x}{\partial \Phi_{\rm ext}}|_{\Phi_{\rm dc}} \Phi_{\rm sq}(t)$ and $\omega_{10} = \omega_0 + \frac{\partial \omega_{10}}{\partial \Phi_{\rm ext}}|_{\Phi_{\rm dc}} \Phi_{\rm sq}(t) = \omega_0 + f_{\rm sq}(t)$.

The modulation of the magnetic field is a square function. For the modulation $f_{\rm sq}(t)$ of ω_{10} we denote the amplitude of this wave by δ and its frequency by Ω; the Fourier series expansion of $f_{\rm sq}$ is

$$f_{\rm sq}(t) = \frac{4\delta}{\pi} \sum_{j=0}^{\infty} \frac{(-1)^j}{2j+1} \cos\left[(2j+1)\Omega t\right]. \tag{4.9}$$

Besides the flux modulation, the qubit is also driven by the tone in the measuring resonator, $n_g(t) = n_g^0 \sin(\omega t)$. The transmon allows as well for an alternative type of driving through the flux line, which exploits the asymmetry of the junctions, but which leads eventually to the same effective form as Eq. (4.10) used below. We then assume that the driving field ω couples only the ground state and the excited state. This approximation is reasonable since the detuning of the field is smaller than the anharmonicity $E_{\rm C}$, that is $\hbar|\omega_{10} - \omega| < E_{\rm C}$.

Next, we transform into a frame rotating at the drive frequency ω around the z-axis, implemented by the unitary transformation $\exp[-i\omega\hat{\sigma}_z t/2]$. We have checked numerically that the modulation of ω_y can be neglected; this can be seen also by applying the rotating wave approximation (note that also that the higher-frequency components of the square function have decreasing amplitudes). With the notation $g = n_g^0 \left[2E_{\rm C}^3 E_{\rm J\Sigma} \cos(\pi\Phi_{\rm ext}/\Phi_0)\right]^{1/4}$, we can bring the Hamiltonian into the final effective form

$$\hat{H}_{\rm eff}(t) = \frac{\hbar}{2}\left[\omega_0 - \omega + f_{\rm sq}(t)\right]\hat{\sigma}_z + \frac{\hbar g}{2}\hat{\sigma}_x. \tag{4.10}$$

The Hamiltonian Eq. (4.10) can be transformed into a frame co-rotating with the longitudinal modulation $f_{\rm sq}(t)$ by employing the unitary transfor-

mation

$$\hat{U}(t) = \exp\left(-\frac{\mathrm{i}\hat{\sigma}_z}{2}\int_0^t f_{sq}(\tau)\mathrm{d}\tau\right), \tag{4.11}$$

which, in the Bloch-sphere picture, corresponds to a frame rotating around the z-axis with the instantaneous angular velocity $f_{\mathrm{sq}}(t)$. In this frame, the new effective Hamiltonian is obtained by $\hat{H}' = \hat{U}^\dagger\hat{H}\hat{U} + \mathrm{i}\hbar(\partial_t\hat{U}^\dagger)\hat{U}$,

$$\hat{H}_{\mathrm{eff}}(t) = \frac{\hbar}{2}(\omega_0-\omega)\hat{\sigma}_z + \frac{\hbar g}{2}\left[A_{\mathrm{sq}}(t)\hat{\sigma}_+ + A^\star_{\mathrm{sq}}(t)\hat{\sigma}_-\right], \tag{4.12}$$

where the time-dependent phase factor $A(t)$ plays the role of an excitation probability amplitude and is defined as $A_{\mathrm{sq}}(t) = \exp(\mathrm{i}\int_0^t f_{\mathrm{sq}}(\tau)\mathrm{d}\tau)$.

We now use the Jacobi-Anger relation to find the harmonic expansion for the excitation probability amplitude A_{sq},

$$\begin{aligned} A_{\mathrm{sq}}(t) &= \prod_{j=0}^{\infty}\sum_{k=-\infty}^{\infty} J_k\left[\frac{4\delta}{\pi\Omega}\frac{(-1)^j}{(2j+1)^2}\right]\mathrm{e}^{\mathrm{i}k(2j+1)\Omega t} \\ &\approx \sum_{m=-\infty}^{\infty} J_0\left(-\frac{4\delta}{9\pi\Omega}\right)J_m\left(\frac{4\delta}{\pi\Omega}\right)\mathrm{e}^{\mathrm{i}m\Omega t} \\ &= \sum_m \Delta_m^{\mathrm{sq}}\mathrm{e}^{\mathrm{i}m\Omega t}, \end{aligned} \tag{4.13}$$

where we use the approximation that the terms with $j \geq 2$ do not contribute and the terms with $j = 1$ contribute only with the overall amplitude $J_0(-4\delta/9\pi\Omega)$. Higher-order approximations for Δ_m^{sq} can be obtained as well. The sideband amplitude for periodic latching $f(t) = f_{\mathrm{sq}}(t)$ can be written in the form

$$\Delta_m^{\mathrm{sq}} = \sum_{\{k_j\}} J_{k_0}\left(\frac{4\delta}{\pi\Omega}\right)J_{k_1}\left(-\frac{4\delta}{9\pi\Omega}\right)J_{k_2}\left(\frac{4\delta}{25\pi\Omega}\right)\cdots J_{k_j}\left(\frac{4\delta}{\pi\Omega}\frac{(-1)^j}{(2j+1)^2}\right)\cdots\Big|_{m=\sum_{j=0}^{\infty}(2j+1)k_j}, \tag{4.14}$$

where all k_j's take integer values from $-\infty$ to ∞ and the summation goes over all possible combinations $\{k_j\}$ that result in $m = \sum_{j=0}^{\infty}(2j+1)k_j$.

To make further progress, we consider the limit $\delta/\Omega \ll 1$ and we use the properties of the Bessel functions: near the origin, J_0 approaches 1 while all the other Bessel functions $J_n(x)$ with n non-zero integer are close to zero. Indeed, in the first order Taylor-series expansion, $J_n(x) \approx (1/n!)(x/2)^n$ and $J_{-n}(x) \approx (-1)^n(1/n!)(x/2)^n$, with $n > 0$, thus the order n of the Bessel function is also the order of the dominant term x^n in this expansion. Now, assume that for a given m we want to find the $\{k_j\}$'s such that the condition $m = k_0 + 3k_1 + 5k_2 + ...(2j+1)k_j + ...$ is satisfied. With the $\{k_j\}$'s thus identified, the order of the corresponding product of Bessel functions in Eq. (4.14) will then be $|k_0| + |k_1| + ...|k_j| + ...$, which allows products of higher order. Then, one can cut off the sum

at some $j_{\max}$ based on the observation that the argument of the Bessel functions in Eq. (4.14) decreases quadratically as $1/(2j+1)^2$. This allows us to truncate the series and calculate numerically Δ_m^{sq}. For example, the second order terms from $j=0$ to $j=3$ in the series Eq. (4.14) are $(k_0,k_1,k_2,k_3)\in\{(2,0,0,0,);(-1,1,0,0);(0,-1,1,0);(0,0,-1,1)\}$, in the decreasing order of their contributions. Then the next terms are of the fourth order, $(k_0,k_1,k_2,k_3)\in\{(-3,0,1,0);(1,2,-1,0)\}$.

With these approximations, the resulting effective Hamiltonian written in a frame rotating at frequency $\omega_0-\omega$ around the z axis becomes

$$\hat{H}_{\mathrm{eff}}(t)=\frac{\hbar}{2}\left[\sum_{m=-\infty}^{\infty} g\Delta_m^{\mathrm{sq}}\mathrm{e}^{\mathrm{i}(m\Omega-\omega+\omega_0)t}\hat{\sigma}_+ + \mathrm{H.c.}\right]. \tag{4.15}$$

As seen by the qubit, the driving (the second term in Eq. (4.12)) - is a sum of different driving fields. When $\omega\approx\omega_0+m\Omega$ if the other driving fields are not too strong $g\Delta_k<\Omega$, $k\neq m$, we can make the rotating wave approximation (RWA) by neglecting the non-resonant driving fields. Thus the general Hamiltonian Eq. (4.12) can be transformed to a rotating frame,

$$\hat{H}_{\mathrm{RWA}}=\frac{\hbar}{2}\left[(\omega_0+m\Omega-\omega)\hat{\sigma}_z+g\Delta_m^{\mathrm{sq}}\hat{\sigma}_x\right]. \tag{4.16}$$

Using the dressed state picture, the terms of Eq. (4.16) describe the two nearly resonant doubly dressed states and their coupling, respectively. Considering the dynamics in the Bloch sphere representation, the Hamiltonian Eq. (4.16) generates precession around the vector $(g\Delta_m^{\mathrm{sq}},0,\omega_0+m\Omega-\omega)$ with Rabi frequency

$$g_{\mathrm{d}}^{(\mathrm{m})}=\sqrt{(\omega_0-\omega+m\Omega)^2+g^2\left(\Delta_m^{\mathrm{sq}}\right)^2}. \tag{4.17}$$

In other words, by applying the transverse driving field at the frequency ω equal to the energy difference of the longitudinally dressed states $\omega_0\pm m\Omega$, coherent oscillations with rate $g_{\mathrm{d}}^{(\mathrm{m})}$ are produced between the transmon qubit eigenstates. This demonstrates that sideband control of the single qubit states using frequency modulation is possible [54, 55].

To find the steady state occupation probability P_e, the master equation

$$\begin{aligned}\frac{\mathrm{d}\hat{\rho}(t)}{\mathrm{d}t} &= -\frac{\mathrm{i}}{\hbar}[\hat{H}_{\mathrm{RWA}}(t),\hat{\rho}(t)]-\frac{1}{4}\Gamma_\varphi\left[\hat{\sigma}_z,[\hat{\sigma}_z,\hat{\rho}]\right]\\ &\quad+\frac{1}{2}\Gamma_1\left(2\hat{\sigma}_-\hat{\rho}\hat{\sigma}_+-\hat{\sigma}_+\hat{\sigma}_-\hat{\rho}-\hat{\rho}\hat{\sigma}_+\hat{\sigma}_-\right),\end{aligned} \tag{4.18}$$

which includes the relaxation with the rate Γ_1 and the pure dephasing with the rate Γ_φ ($\Gamma_2=\Gamma_1/2+\Gamma_\varphi$) can be solved analytically around every resolvable resonance [56, 57], *i.e.*, by assuming the RWA as in Eq. (4.16). Note

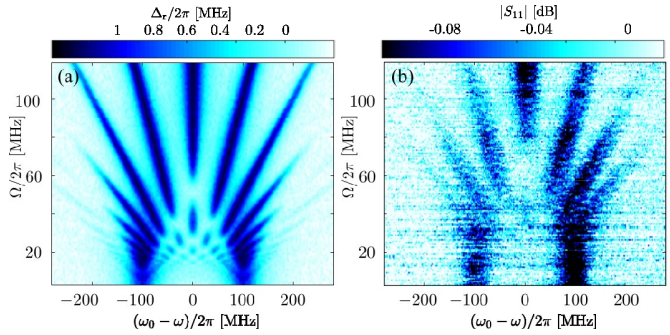

Figure 4.8. Simulation (a) of the transmon dispersive shift and measured (b) reflection coefficient with square wave modulation and parameters $\delta/2\pi = 100$ MHz, $g/2\pi = 20$ MHz, $\Gamma_1/2\pi = 1$ MHz, $\Gamma_2/2\pi = 3$ MHz.

that when decoherence is introduced, the width of the sidebands is broadened due to both the rate Γ_2 and due to the power broadening caused by the strong transverse driving, $g\Delta_m^{\rm sq}$ yielding a linewidth $\lesssim \sqrt{\Gamma_2^2 + (g\Delta_m^{\rm sq})^2\Gamma_2/\Gamma_1}$. In order to apply the RWA as above, the sidebands should be resolvable, *i.e.* the spacing Ω between the sidebands should be larger than the linewidth. Summing the contribution of all independent resonances results in

$$P_e^{\rm sq} = \sum_{m=-\infty}^{\infty} \frac{\frac{\Gamma_2}{2\Gamma_1}\left(g\Delta_m^{\rm sq}\right)^2}{\Gamma_2^2 + (\omega_0 - \omega + m\Omega)^2 + \frac{\Gamma_2}{\Gamma_1}\left(g\Delta_m^{\rm sq}\right)^2} \tag{4.19}$$

for the steady state occupation probability of the qubit excited state.

A related quantity is the absorption spectrum defined as

$$S^{\rm sq}(\omega) = (2\pi)^{-1}\int_{-\infty}^{\infty} d\tau \exp(i\omega t)\langle\hat{\sigma}_-(\tau)\hat{\sigma}_+(0)\rangle_{\rm sq} \tag{4.20}$$

which yields

$$S^{\rm sq}(\omega) = \frac{g^2}{\pi}\sum_{m=-\infty}^{\infty} \frac{\Gamma_2\Delta_m^{\rm sq}}{(\omega_0 - \omega + m\Omega)^2 + \Gamma_2^2}. \tag{4.21}$$

Again we see that the periodic square pulses create multi-photon sidebands into the absorption spectrum, which are resolvable for $g|\Delta_m^{\rm sq}| < \Omega$.

The appearance of a specific pattern of sidebands in the spectrum can be understood as well as the result of the Landau-Zener-Stückelberg (LZS) interference. For sine modulation a detailed analysis for these photon-assisted LSZ transitions has been presented in section 4.3.1. For square modulation, we note first that Eq. (4.10) is the standard form for LSZ Hamiltonians, describing an avoided crossing which is approached by the particles during the pulsed driving $f_{\rm sq}(t)$. Intriguingly, a direct application of the standard adiabatic-impulse method would lead to the conclusion that the Landau-Zener (LZ) velocity at the avoided crossing is infinite for ideal square pulses, resulting in a unit LZ probability, thus precluding

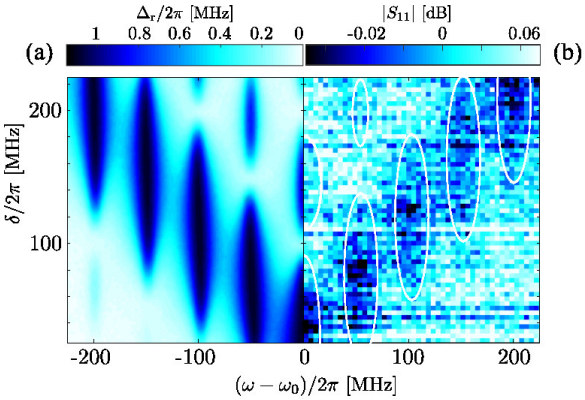

Figure 4.9. Landau-Zener-Stückelberg interference pattern for a square modulation of the system, presented in a compact form with the simulation (a) for negative detunings and experiment (b) for positive detunings. The white ellipses show the theoretically-predicted positions of the LZS maxima. The modulation frequency was fixed at $\Omega = 50$ MHz.

any interference effect. Thus, for square modulation the standard LZ formula is not applicable. A new formalism has to be developed, as we will discuss later in this section. In Fig. 4.9 we plot a few LZS oscillations as a function of modulation amplitude δ for several values of the detuning $\omega - \omega_0$ with respect to the qubit frequency and at fixed modulation amplitude $\Omega/2\pi = 50$ MHz.

Comparison with sinusoidal modulation

Finally, one can compare the spectrum of the system under a square modulation with that under a sine modulation with exactly the same parameters (the same qubit frequency ω_0 and the same modulation amplitude as in Fig. 4.8. The reflection spectrum is presented in Fig. 4.10. By a similar calculation to Eqs. (4.10-4.22) we get, for sine modulation,

$$P_e^{\sin} = \sum_{m=-\infty}^{\infty} \frac{\frac{\Gamma_2}{2\Gamma_1}\left(g\Delta_m^{\sin}\right)^2}{\Gamma_2^2 + (\omega_0 - \omega + m\Omega)^2 + \frac{\Gamma_2}{\Gamma_1}\left(g\Delta_m^{\sin}\right)^2} \tag{4.22}$$

where $\Delta_m^{\sin} = J_m\left(\frac{\delta}{\Omega}\right)$. One notices already from the spectra in Fig. 4.8 and in Fig. 4.10 that the structure at low and intermediate modulation frequencies is different. In Fig. 4.11 we present such a comparison, where for clarity we show the spectra in the low-frequency range, up to 80 MHz. Figure 4.11 shows that the extrema of the multi-photon resonances obtained from the full numerical calculation are shifted from those of the RWA steady state population Eq. (4.22), especially when Ω is small. This discrepancy can be partly removed by including more terms to the approximative Bessel series in Eq. (4.15). Also, when the frequency Ω is small,

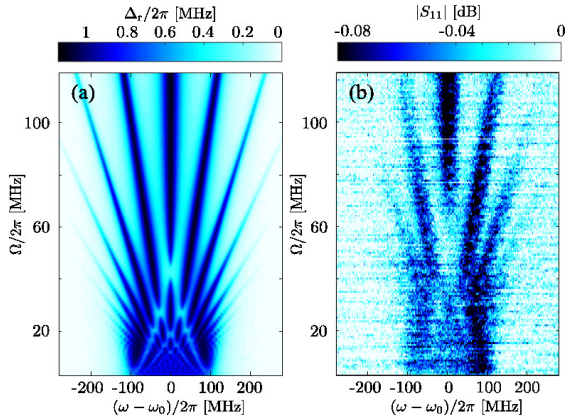

Figure 4.10. Spectrum under harmonic modulation around the qubit frequency ω_0 and with the same modulation amplitude $\delta/2\pi = 100$ MHz as in Fig. 4.8: (a) numerical simulation, and (b) experimental data.

the individual peaks are not resolved and the RWA made in the derivation of Eq. (4.22) is not sufficient. The accuracy of the analytic steady state population can be improved by making Bloch-Siegert and higher order corrections (so-called generalized Bloch-Siegert shift to the RWA calculation) [52]. At large Ω the two structures become rather similar and the two types of modulation cannot be distinguished anymore. This can be understood already from the approximate analytical equations. When driving resonantly with a sideband, we have $\omega = \omega_0 + m\Omega$, and the value of $P_e^{\sin}$ and P_e^{sq} depend only on the values of $\Delta_m^{\sin}$ and Δ_m^{sq}, with the minimum value $P_e = 0$ occurring at the roots of Bessel functions, irrespective of the value of g. The phenomenon of suppression of the tunneling oscillations at these points is sometimes referred to as coherent destruction of tunneling (CDT) [58]: a particle that tunnels back and forth between two wells can become localized in one of the wells if the wells' potentials are modulated at an appropriate frequency. In the simplest sine-oscillation models, this modulation frequency turns out to be determined, for a sideband m, by the same condition $J_m(\delta/\Omega) = 0$ [49]. The coherent destruction of tunneling exists for square wave modulation, and it is approximately given by the condition $\Delta_m^{\mathrm{sq}} = 0$. This phenomenon is not spoiled by the weak anharmonicity of the transmon, and it is also predicted by the numerical simulation.

In contrast, the saturation value $P_e = 1/2$ is reached when $\Delta_m^{\mathrm{sq}}, \Delta_m^{\sin} \gg \sqrt{\Gamma_1\Gamma_2}$, and this depends on the value of g. For relatively large g (compared to $\sqrt{\Gamma_1\Gamma_2}$) the Bessel modulation brings the population to zero only very close to the root of J_k, and changes in J_k do not affect the population unless

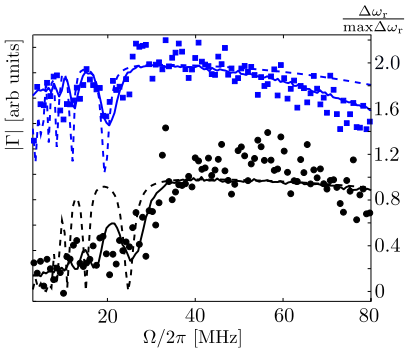

Figure 4.11. Comparison between the population of the second sideband under sine (blue) and square (black) modulation, with the same measurement parameters and the same modulation amplitude. The axis on the left is the measured microwave reflection coefficient Γ. The right axis presents the normalized frequency shifts of the cavity as predicted by the theoretical simulation (continuous lines), and by the analytical formulas Eq. (4.19) (dotted lines). In the real data the high-Ω values coincide for both sine and square modulation. The two sets of figures are shifted for clarity by 0.7 on the right axis.

the value of J_k becomes smaller than $\sqrt{\Gamma_1\Gamma_2}/g$. As a result, the dependence on Ω is rather weak and the spectral line along the sideband becomes flat, as one can see in Fig. 4.11.

The numerical simulation (see Fig. 4.8,4.9 and 4.10) were performed including the 5 energy levels of the transmon. The transmon has a relatively low anharmonicity ($\sim$300MHz) and taking into account the higher energy states in the simulations led to better agreement with the experimental results, as the occupation of higher excited states is not necessarily negligible. The effects of the decay and the dephasing times can be more readily understood by examining Eq. (4.19) and Eq. (4.22), which were derived using the rotating wave approximation. We can see that this is a Lorenzian-shape spectrum where the width originates from two effects: one is the decoherence with rate Γ_2 (the inverse of the T_2 time), and the other is the power broadening (the term containing g. For an ideal qubit without decoherence, only the power broadening term contributes to the linewidth, thereby producing a sharper spectral line. Thus the interference effects and its fine details could be better visible if the qubit's decoherence time were improved.

LSZ formalism and the square wave modulation

As we mentioned previously, in the case of square modulation the standard Landau-Zener formula is no longer applicable. We describe a theoretical approach based on the transfer matrix formalism, that fully explains the

resonances and antiresonances seen in the experiment. This approach does not use the LZ formula: instead, it uses the sudden approximation to calculate the transition probabilities. Here we only discuss some similarities to our problem of square pulse modulation with the standard LZS description of interference. We start with the Hamiltonian

$$\hat{H}_{\mathrm{eff}}(t) = \frac{\hbar}{2}\big[\omega_0 - \omega + f_{\mathrm{sq}}(t)\big]\hat{\sigma}_z + \frac{\hbar g}{2}\hat{\sigma}_x, \tag{4.23}$$

which is exactly of the form of the generic LZS-Hamiltonian. It describes a two-level system whose energy levels are σ_x-coupled, and the resulting avoided crossing of energy levels is swept periodically. In the standard LZS treatment, the dynamics of the time-periodic system is discretized to a free adiabatic time-evolution interrupted by instantaneous non-adiabatic Landau-Zener transitions at the location of the avoided crossing (the so-called adiabatic-impulse method). The probability of a single transition between the adiabatic energy states is

$$P_{\mathrm{LZ}} = e^{-2\pi\alpha}, \tag{4.24}$$

where $\alpha = g^2/4|\nu|$, and the rate of change of the diabatic energy separation evaluated at the crossing is given by $\nu = [df_{\mathrm{sq}}/dt]_{\mathrm{cross}}$. Note that in the case of ideal square pulses, ν is infinite and the Landau-Zener formula predicts $P_{\mathrm{LZ}} = 1$.

The LZS formalism provides, in certain conditions, results that resemble those obtained by the RWA. We start with the observation that both the physical and the numerical realizations of a square pulse always have a finite switching time between the extreme values of f_{sq}. For linear switching with ramp time τ_{ramp}, one can estimate $|\nu| \approx 2\delta/\tau_{\mathrm{ramp}}$. Thus, the rate of change ν is finite and the LZS-model applies. For rapid switching we approximate $P_{\mathrm{LZ}} \approx 1 - 2\pi\alpha$, and that the adiabatic phase collected during the switching can be neglected. The driving forces the system to traverse the avoided crossing periodically. During each traversal, the evolutionary path of the system is split in two due to the possibility of an LZ-transition. The probability amplitudes for different paths can interfere and, by starting from the ground state of the system and averaging over many periods of the drive, we end up with a steady-state population in the first level

$$P_{\mathrm{e}} = \frac{P_{\mathrm{St}}}{2\sin^2\xi}, \tag{4.25}$$

where (in the diabatic limit)

$$P_{\rm st} = 4P_{\rm LZ}(1-P_{\rm LZ})\cos^2(\zeta_2-\pi/4), \tag{4.26}$$

$$\sin^2\xi = P_{\rm st} + P_{\rm LZ}^2\sin^2\zeta_-, \tag{4.27}$$

$$\zeta_- = \zeta_1-\zeta_2. \tag{4.28}$$

Here $\pi/4$ is the so-called diabatic Stokes phase, collected during the non-adiabatic time-evolution. The adiabatic phases collected within a drive period before and after the LZ-transition are defined as

$$\zeta_1 = \tfrac{\pi}{2\Omega}\sqrt{(\omega_0-\omega+\delta)^2+g^2}, \tag{4.29}$$

$$\zeta_2 = \tfrac{\pi}{2\Omega}\sqrt{(\omega_0-\omega-\delta)^2+g^2}, \tag{4.30}$$

respectively. We have also defined the diabatic phase ζ_- collected during the period. The maximum excited state population $P_+ = \frac{1}{2}$ occurs when $\sin^2\xi$ has a minimum, *i.e.* when $\zeta_- = m\pi$ with integer m. When $g \ll |\omega_0-\omega| \ll \delta$, we obtain the familiar multi-photon resonance condition $\omega_0 = \omega - m\Omega$, while if we detune the system slightly from a resonance by an amount $\omega_0-\omega+m\Omega$ we can write the steady state population as

$$P_{\rm e} \approx \frac{1}{2}\frac{\Delta_m^2}{(\omega_0-\omega+m\Omega)^2+\Delta_m^2}, \tag{4.31}$$

which has the same form as the steady state population Eq. (4.22) that results from the RWA Hamiltonian Eq. (4.16). In the above,

$$\Delta_m = \sqrt{2\pi\alpha}\frac{2\Omega}{\pi}\cos\left[\frac{\delta\pi}{2\Omega}-\frac{\pi}{4}(2m+1)\right] \approx \sqrt{2\pi\alpha}\sqrt{\Omega\delta}J_m\Big(\frac{\pi\delta}{2\Omega}\Big), \tag{4.32}$$

where for the latter approximation we use $J_m(z) \approx \sqrt{2/\pi z}\cos[z-\pi(2m+1)/4]$ which holds when $\delta/\Omega > m$.

The calculation above demonstrates that the LZS-model predicts a similar Bessel-function structure for the probabilities as the RWA. However, in spite of the resemblance between Eq. (4.32) and Eq. (4.22), it should be emphasized that the approximation used in the RWA calculation assumes that δ/Ω is small, while the LZS-result above works only when $\delta \gtrsim m\Omega$. These limits are valid in general at different points in the data, for example, in the side-band modulation spectrum Fig. 4.8, the ratio $\delta/\Omega = \infty\ldots1$, while in the LZS interference pattern Fig. 4.9 we have $\delta/\Omega = 0\ldots5$. A further quantitative comparison of the two models would require a truncation of the Fourier series of the square wave (first equality in Eq. (4.13)), leading into a finite switching time for the square pulse. When $\delta \sim m\Omega$, the above calculation can be improved by the inclusion of the effects of g in the adiabatic phases.

4.3.3 Random telegraph noise

The concept of motional averaging and motional narrowing [59, 60] was observed in the nuclear magnetic resonance spectrum of a system consisting of spin-1/2 particles filling a porous material. The pore wall is paramagnetic and the system is subject to an external magnetic field; so the particles near it will experience a modified local magnetic field. When the particles are static they will produce two spectral peaks in the NMR spectrum at frequencies ω_1 and ω_2. In contrast, particles moving swiftly back and forth between the two regions on timescales Δt shorter than $\hbar(\Delta E)^{-1} = (\omega_2 - \omega_1)^{-1}$ are not able to discriminate between the two energy values. Then, as the particles move faster, the outcome in the spectroscopy is not simply a continuous broadening and overlapping of the two peaks. Instead, a new peak emerges at the average frequency ω_0 (motional averaging) with a width smaller than the energy separation $\Delta E/\hbar$ (motional narrowing). In atomic ensembles and condensed-matter systems, this occurs via fast variations of the chemical potential, molecular conformation, effective magnetic fields, lattice vibrations, micro-electric fields producing ac-Stark shifts *etc.*.

The most interesting phenomenon occurs when the transmon is modulated by Random Telegraph Noise (RTN).To generate RTN pulses, we use MATLAB's internal Poisson random number generator $poissrnd(\lambda)$ to obtain binary RTN sequences, and load the sequences into the Agilent 81150A AWG. Each binary RTN sequence consists of 50000 data points and around 5000 random jumps in average. The mean jumping rate χ (of AWG's output) is modulated by changing the clock frequency ν of the AWG: $\chi \approx 5000 \times \nu$. To verify this relation between χ and ν, we observe the RTN sequences at different ν's by a fast oscilloscope (10 GS/s), count the number n of edges (jumping events) for certain period of time t, and calculate the real mean jumping rate by its original definition, $\chi = n/t$. 25 jumps are counted during 0.5 μs, which gives $\chi = 50$ MHz. As long as $\nu < 100$ KHz, the formula $\chi \approx 5000 \times \nu$ gives a good estimation of the mean jumping rate. For $\nu > 100$ KHz, the real mean jumping rate is smaller than the estimated one, due to the intrinsic ~ 2 ns rising/falling time of the AWG (pulses shorter than 4 ns have a certain chance to merge together).

On modulating the qubit with the defined RTN, the Hamiltonian of the transmon qubit is written as

$$\hat{H}(t) = \frac{\hbar}{2}[\omega_0 + \xi(t)]\hat{\sigma}_z, \tag{4.33}$$

The random telegraph noise (RTN) is generated by an arbitrary waveform generator and couples longitudinally through the on-chip flux bias coil of the qubit. The resulting fluctuations in flux $\Phi_{\mathrm{ac}}(t)$ leads to the the time-dependent part $\hbar\xi(t)$ of the energy splitting. The RTN follows the dynamics of a stationary, dichotomous Markovian process, characterized by an average jumping rate χ and symmetrical dwellings at frequency values of $\pm\xi$. The number of jumps is a Poisson process with the probability $P_n(t) = (\chi t)^n e^{-\chi t}/n!$ for exactly n jumps within a time interval t. This Poissonian process simulates the temporal variations causing motional averaging in atomic ensembles and condensed-matter systems.

Now we proceed to calculate the absorption spectrum for a qubit subjected to RTN fluctuations as in equation (4.33), using the quantum regression theorem [61],

$$S(\omega) = \frac{1}{2\pi}\int_{-\infty}^{\infty} \mathrm{e}^{\mathrm{i}(\omega-\omega_0)\tau-\Gamma_2|\tau|}\left\langle \mathrm{e}^{-\mathrm{i}\int_0^\tau \xi(t)\,\mathrm{d}t}\right\rangle_\xi \mathrm{d}\tau, \tag{4.34}$$

where the expectation value is taken over noise realizations and $\Gamma_2 = \Gamma_\varphi + \Gamma_1/2$ is the decoherence rate in the absence of modulation. For our sample $\Gamma_2 \approx 2\pi \times 3$ MHz (determined in an independent measurement). For the Poisson process $\xi(t)$, Eq. (4.34) gives

$$S(\omega) = \frac{1}{\pi}\frac{2\chi\xi^2 + \Gamma_2\left(\bar{\Gamma}_2^2 + \bar{\omega}^2 + \xi^2\right)}{(\xi^2 - \bar{\omega}^2 + \Gamma_2\bar{\Gamma}_2)^2 + 4(\Gamma_2+\chi)^2\bar{\omega}^2}, \tag{4.35}$$

with $\bar{\Gamma}_2 = \Gamma_2 + 2\chi$ and $\bar{\omega} = \omega - \omega_0$. For the spectrum measurements, the qubit is subject to transverse drive given by

$$\hat{H}_{\mathrm{drive}}(t) = \hbar g\cos(\omega t)\hat{\sigma}_x. \tag{4.36}$$

The measurement results of the spectrum of the qubit showing the population of the qubit's excited state, as shown in Fig. 4.12. The simulation of the occupation probability presented in Fig. 4.12a includes also the effect of power broadening due to strong driving amplitudes ($g > \Gamma_1, \Gamma_2$).

From the spectrum, it is evident that the dynamics of the system behaves differently on the two sides of the threshold $\chi = \xi$. In the case of slow jumping, $\chi \ll \xi$, and resolvable energy variations, $\Delta E\Delta t \sim \hbar\xi/\chi \gg \hbar$, the qubit absorbs energy at $\omega_0 \pm \xi$ with the total decoherence rate $\Gamma_2' = \Gamma_2 + \chi$. The correlation time of the displacement process $\hbar\xi(t)$ is $\tau_r = (2\chi)^{-1}$ and the linewidth (full width at half maximum $2\Gamma_2'$) broadens by the amount of the reduced mean life-time of a qubit excitation (exchange broadening). In contrast, for fast jumping processes, $\chi \gg \xi$, and when the variations are not resolvable, $\Delta E\Delta t \sim \hbar\xi/\chi \ll \hbar$, the qubit absorbs energy only at

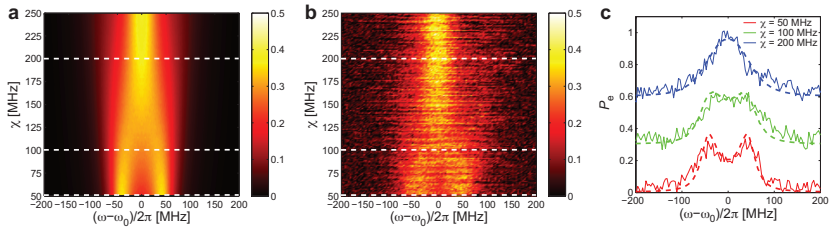

Figure 4.12. Motional averaging. a, Plot of the numerical simulation of the occupation probability P_e in the $\omega - \chi$ plane with parameters $\xi/2\pi = 43$ MHz, $g/2\pi = 8$ MHz, $\Gamma_1/2\pi = 1$ MHz, and $\Gamma_2/2\pi = 3$ MHz. **b,** Experimental results. **c,** Behavior of the system across the dynamical threshold $\chi = \xi$. When $\chi \ll \xi$, two resolved peaks are seen, and when $\chi \gg \xi$, motional averaging effect is seen. Maximum decoherence observed when $\chi = \xi$. The measurement results (solid lines) and numerical simulation results (dashed lines) are displaced for clarity.

the frequency ω_0 with $\Gamma_2' = \Gamma_2 + \xi^2/2\chi$. The increase in decoherence rate by $\xi^2/2\chi$ can be related to the excursions of the accumulated phase $u(\tau) = \int_0^\tau \xi(t)\,\mathrm{d}t$ [cf. equation (4.34)] for single noise realizations, especially to the diffusion coefficient of the process. Surprisingly, the averaged spectral line is well-localized around the mean value, since $\xi^2/2\chi \ll 2\xi$.

The two interesting observations about the decoherence at specific jumping rates can be made based on these results. For the case $\chi \gg \xi$, a raise in the height of the central peak is observed, as the additional decoherence $\xi^2/2\chi$ decreases with increasing jumping rate χ. This effect called motional narrowing is seen in Fig. 4.12c (blue curve). But when χ is comparable with ξ, there is a cross-over region where absorption is reduced and the peak broadens due to enhanced decoherence (green curve in Fig. 4.12c). This shows that a two-level system (TLS) fluctuator causes maximal decoherence when its fluctuation occurs approximately at the same frequency as the coupling to the qubit.

4.4 Summary

In this chapter, we have presented the results of modulation of the transition frequency of a transmon, an artificial atom. This led to the observation of a rich structure of sidebands under sinusoidal modulation and square modulation and the demontration of the effect of motional averaging under random telegraph noise modulation.

For the case of periodic modulation, it can be explained by a model that includes driving and frequency modulation, or it can be seen alternatively

as a type of Landau-Zener-Stückelberg interference in a frame rotating at the drive frequency. The phenomenon of coherent destruction of tunneling is observed as the suppression of the transition to the excited level at specific modulation frequencies. We show that the information about the shape of the pulses can be extracted from the spectral region corresponding to a relatively low modulation frequency.

Random telegraph fluctuation measurements can be regarded as a simulation of a fast-fluctuating environment with the advantage of direct experimental control [56]. This should be contrasted with the typical situation in condensed-matter systems, where one has a large number of particles and the experimentalist can only indirectly attempt to change the fluctuation rate, typically by modifying a thermodynamic function of state such as temperature or pressure.

Our work opens a number of new research directions. First, the formation of sidebands can be useful in quantum computing, because they retain the quantum coherence of the qubit, behaving as additional quantum degrees of freedom that do not need extra hardware on the chip, and that can be controlled in a simple way through the modulation frequency. For example, they can be coupled to mechanical motion [62] or they can be used in quantum-computing architectures to realize novel types of two- or multiple- qubit quantum gates [54, 55]. For the values of the fields used in our experiment we show that, in a rotating frame, the system reaches the ultrastrong coupling regime [63]. The frequency modulated system can be seen as a realization of a quantum simulator of the ultrastrong coupling regime in contrast to other systems where the ultrastrong coupling was obtained by sample design. We have also discussed the use of circuit QED as a platform for simulating various forms of dephasing noise and for realizing experiments where the switching of the qubit frequency has an experimentally controlled pre-defined time dependence.

5. State control and time-domain measurements in a transmon

By using time domain measurements we can coherently manipulate the quantum state of the qubit and create single qubit gates. The first part of this chapter deals with the coherent dynamics of a two-level system using standard non-adiabatic pulses and presents some of our measurement results. The latter parts of this chapter introduces the stimulated Raman adiabatic passage (STIRAP) where the population dynamics of a three level circuit QED system is observed. STIRAP is widely used in atomic physics as a robust way to transfer population. We demonstrate the usage of this technique to transfer the population from the ground state to the second excited state in a three level transmon. Besides application in quantum computation, this demonstrates a fundamental process pertaining to light-matter interaction in multiple level systems and opens possibilities to further study adiabatic effects such as geometric phases.

5.1 State control by nonadiabatic pulses

In section 2.2, we have discussed harmonic perturbation of a two level system and the resulting Rabi oscillations in the context of designing Rabi pulses of specific duration leading to qubit gates. In this section, we discuss the measurement setup and the experimental results for coherent population transfer by nonadiabatic pulses [64] in a transmon. The decoherence of the qubit is also studied by measuring the decay time T_1 and with Ramsey interference fringes measurements. We also show the experimental results for improved coherence time by subjecting it to decoupling Carr-Purcell (CP) sequence. Next we show results of accessing the second excited state by nonadiabatic pulses, with the interest of leading to the next section Stimulated Raman adiabatic passage (STIRAP), in the three level transmon.

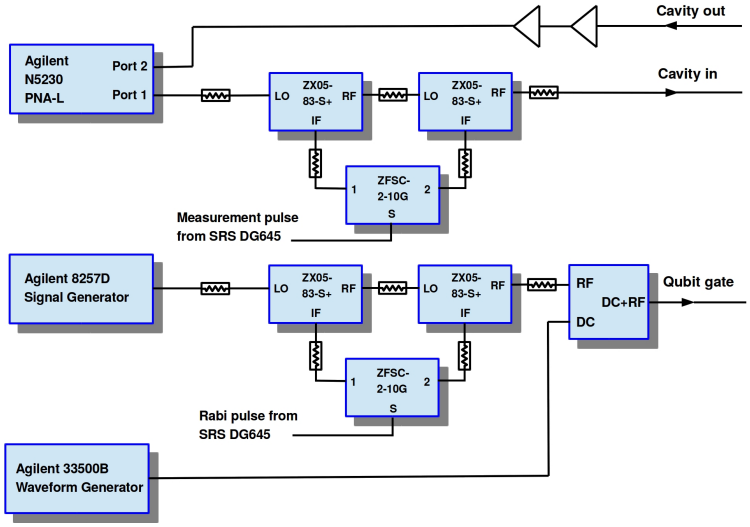

Figure 5.1. Schematic of the measurement setup used for Rabi oscillations measurement.

5.1.1 Rabi Oscillations

This section explains the measurement setup and the experimental results showing the Rabi oscillation in the cQED system. The electronic measurement set-up at room temperature is illustrated in Fig. 5.1. The dc flux bias is generated by an Agilent 81150A arbitrary waveform generator (AWG). The qubit driving signal from an Agilent E8257D analogue signal generator and the CPW cavity probe signal from an Agilent N5230C PNA-L network analyzer. The signal from the cavity output line of the dilution refrigerator is amplified and detected by a PNA-L network analyzer. Between the radio frequency instruments (analog signal generator and network analyzer) and their corresponding lines, dc blocks are used for breaking possible ground loops. All instruments are synchronized with a SRS FS725 rubidium frequency standard (not shown in the figure). The nano second resolution Rabi and measurement pulses (schematic in Fig.5.2), are made by mixing the continuous microwave signal with rectangular pulses from a SRS DG645 digital delay generator via two identical ZX5-83-S+ frequency mixers.

A typical Rabi oscillation measurement is shown in Fig. 5.3. and the effect of the detuning of the drive signal with the qubit transition frequency is shown in Fig. 5.4. The decoherence of the qubit states is clearly seen in Fig. 5.3. The coherence time of the qubit is quantised by the relaxation time T_1 and the dephasing time T_2. The next sections explain the time domain measurements, used to obtain an estimate of T_1 and T_2 respectively.

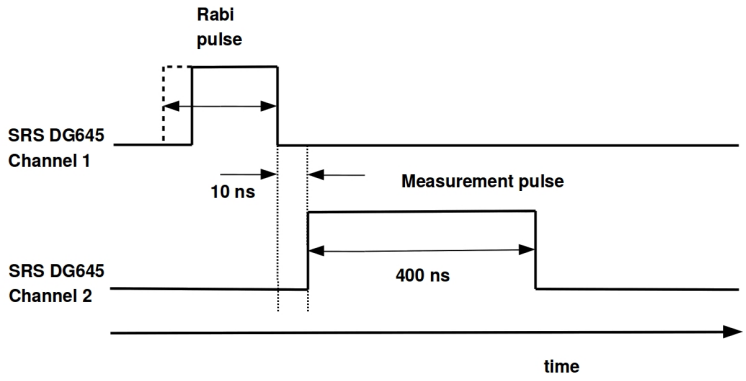

Figure 5.2. Pulse sequence for Rabi oscillation measurement.

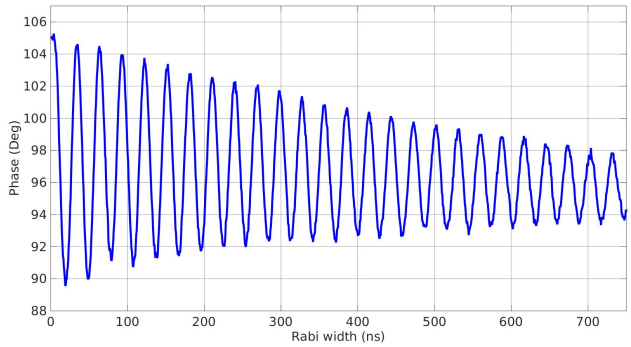

Figure 5.3. Coherent Rabi oscillation measured in the transmon qubit.

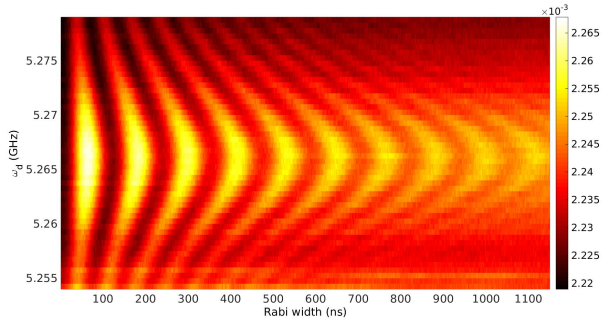

Figure 5.4. Chevron pattern of Rabi oscillations with qubit detuning.

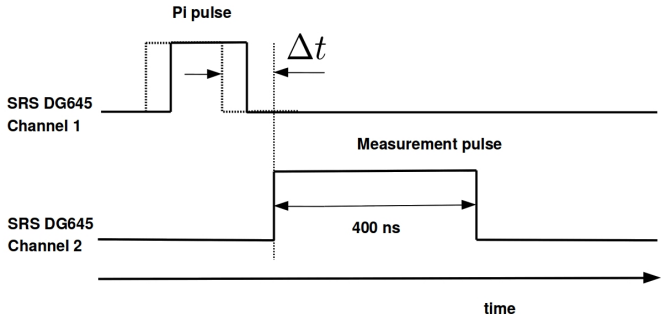

Figure 5.5. Pulse sequence for T_1 measurements.

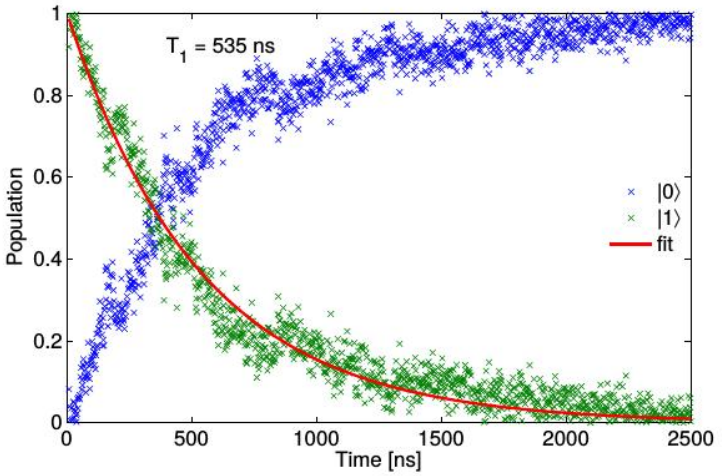

Figure 5.6. Example of a T_1 measurement result in a transmon qubit.

5.1.2 T_1 measurement

From the Rabi measurements, the π pulse width corresponding to a bit flip operation can be obtained. On increasing the time Δt between the π pulse and the measurement pulse (Fig. 5.5), the exponentially falling curve $\exp(-t/T_1)$ is obtained from which the T_1 is estimated as in Fig. 5.6.

5.1.3 Ramsey interference fringes

The pulse sequences for the Ramsey experiments were more complex and we used for this a Tektronix AWG5014B arbitrary waveform generator. The Agilent N5230C PNA-L is employed as a signal generator. Its output signal is split into two parts. One part is used for generating measurement pulses in a similar fashion as the Rabi pulses; the other part acts as a local oscillator (LO) signal to mix the output signal from the cavity via a Marki

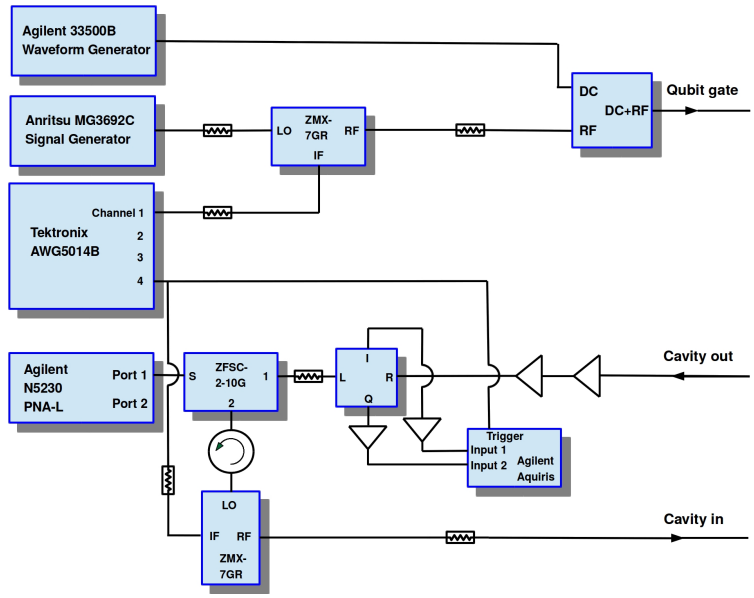

Figure 5.7. Schematic of the Ramsey measurement setup.

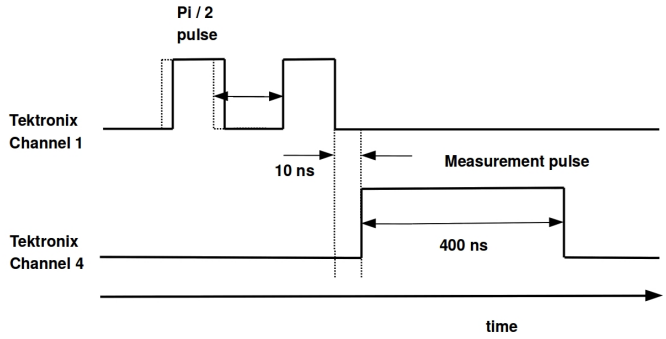

Figure 5.8. Pulse sequence for Ramsey measurement.

IQ mixer. The IQ data is filtered, amplified by a SRS SR445A pre-amplifier, and digitised by an Agilent U1082A-001 digitiser, see Fig. 5.7.

The dephasing time is obtained by the Ramsey measurement. The pulse sequence is shown in Fig. 5.8 and the measurement result is shown in Fig. 5.9.

5.1.4 Decoupling sequences

A number of multi-pulse sequences such as Carr-Purcell (CP), Car-Purcell-Meiboom-Gill (CPMG), Uhrig dynamical decoupling (UDD), *etc.,* [65] have been developed within the field of nuclear magnetic resonance for dynamically decoupling the qubit system from the noisy environment. Recently these techniques have been extended to many other qubit systems based

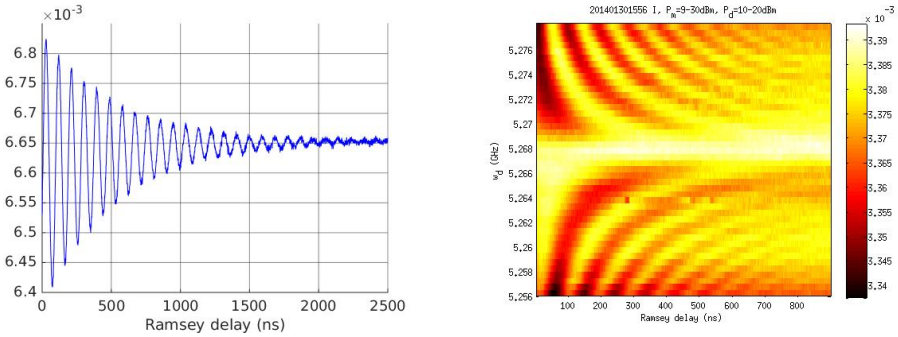

(a) Example of experimentally measured Ramsey oscillations.

(b) Example of a Chevron pattern in a Ramsey measurement.

Figure 5.9. Measured Ramsey oscillations for a transmon sample.

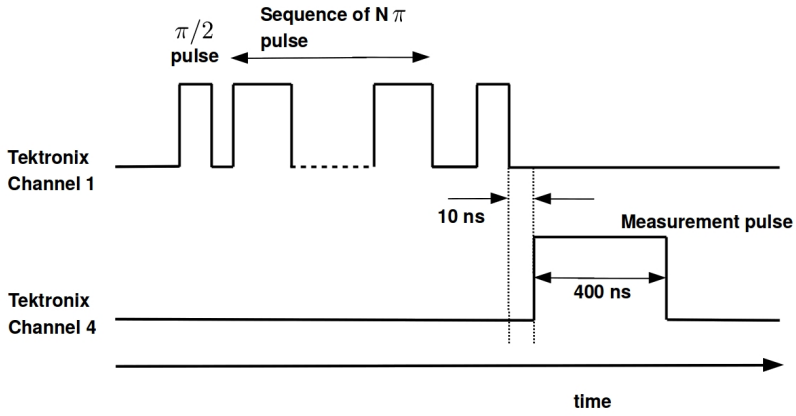

Figure 5.10. Schematic of the CP pulse sequence.

on atomic ensembles, semiconductor quantum dots *etc.* We show that these methods can be used for superconducting quantum devices, and demonstrate that one can obtain a remarkably long-lived transmon qubit by subjecting it to a Carr-Purcell (CP) sequence.

The CP pulse sequence is shown in Fig. 5.10. The spin-echo measurement is a special case of CP pulse sequence when $N = 1$. In other words, it is one π pulse sandwiched between two $\pi/2$ pulses.

The dephasing time increases as the number of π pulses increases. It can be seen from the measurement data shown in Fig. 5.11, that the dephasing time increases as expected as $\{1.3\mu s, 2.1\mu s, 4.5\mu s, 6.4\mu s\}$ corresponding to $N = \{1, 3, 4, 6\}$ respectively.

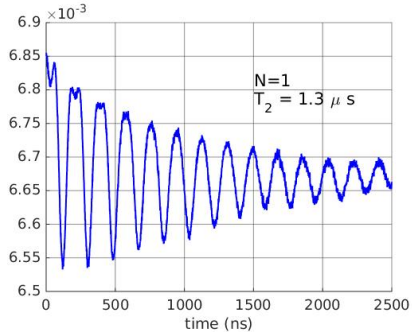

(a) N=1

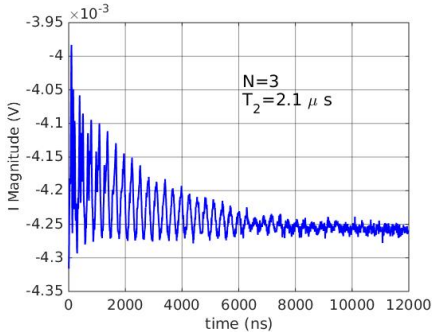

(b) N=3

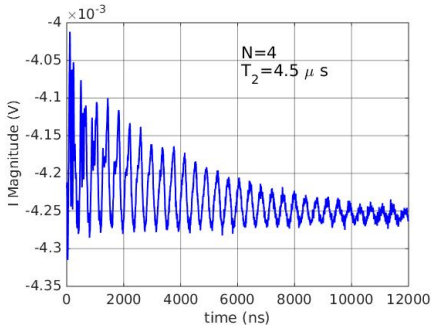

(c) N=4

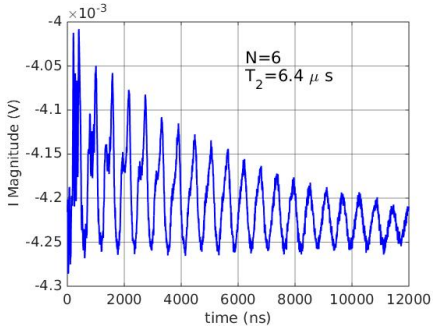

(d) N=6

Figure 5.11. Example of experimentally obtained improvements in T_2 under the Carr-Purcell sequence.

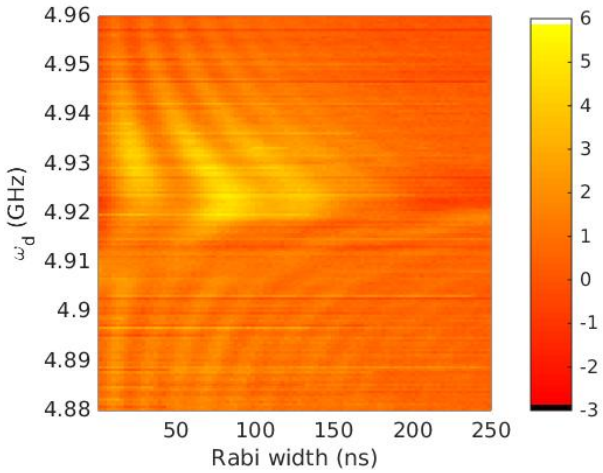

Figure 5.12. Chevron pattern of Rabi oscillations between the first and the second excited states.

5.1.5 Accessing the second excited state by nonadiabatic pulses

Now we attempt to access the second excited state of the transmon. The qubit is excited to state $|1\rangle$ by subjecting it to π_{01} pulse. Then the qubit is subject to a Rabi pulse corresponding to the $|1\rangle$ to $|2\rangle$ transition. After the transition pulses, the cavity response is measured and we observe Rabi oscillation between the first and second excited states as shown in Fig. 5.12. We have checked that these oscillations are indeed between the $|1\rangle$ and $|2\rangle$ states. The oscillations were not present without the π_{01} pulse preceding the Rabi pulse and the $|1\rangle$ to $|2\rangle$ transition frequency agrees with the calculated anharmonicity for the transmon.

5.2 Stimulated Raman adiabatic passage (STIRAP)

Among many requirements in experimental quantum information processing, precise control and manipulation of the state of the system is one of the key components for most of the practical implementations. A large majority of the devices used for quantum information processing are based on quantum two-level systems, qubits. However, recently there has been some interest in using three-level quantum systems in quantum computation [66, 67]. The obvious benefit of building a quantum processor using three level systems instead of two-level systems is their significantly larger Hilbert space, which correspondingly reduces the number of re-

quired qubits to perform certain calculations. Unfortunately the control and the measurement of three-level systems is significantly more difficult than that of two-level systems.

This method has not been previously used in circuit quantum electrodynamics despite its great potential in realizing high fidelity quantum gates in multi-level quantum systems. However, there are some theoretical discussions about the subject [68, 69].

The coherent transfer of population between two energy states of a transmon requires that the spectrum of the system is anharmonic and that the dipole moment between the target states is non-vanishing. In a transmon this only holds for consecutive energy states, and therefore the transfer of population to the $|2\rangle$ state must be done via an intermediate state, $|1\rangle$. When the transfer is done using STIRAP, there will be no population in the intermediate state during the process, which also allows transitions via highly dissipative intermediate states. In quantum systems consisting of real atoms STIRAP has been widely used to transfer population between energly levels in λ configuration, where the transition between the ground and target states is forbidden. In such systems the absense of population in the intermediate state is highly beneficial because of its larger dissitipation. The method works equally well for states in a ladder configuration that we use in the transmon system.

This adiabatic technique requires two coherent microwave fields used to achieve complete population transfer from an initially populated state $|\psi_0\rangle$ to a target state $|\psi_2\rangle$ via an intermediate state $|\psi_1\rangle$. The interesting feature to note is that this technique uses counterintuitive ordering of pulses. In other words, the first pulse couples the initially unpopulated intermediate state $|\psi_1\rangle$ and target state $|\psi_2\rangle$, while the second pulse couples the initially fully populated state $|\psi_0\rangle$ to the unpopulated state $|\psi_1\rangle$. The conditions for successful population transfer by STIRAP is that the two pulses should be of sufficiently strong intensity, there should be sufficient overlap and the time evolution should be adiabatic. We use Gaussian shaped pulses, to ensure the adiabatic evolution of the states. When these conditions are met, STIRAP allows complete population transfer between states $|\psi_0\rangle$ and $|\psi_2\rangle$. In order to understand the dynamics of the population transfer, we start by examining the eigenvalues and the eigenstates of the Hamiltonian driving the probability amplitudes $C(t) = [C_0(t), C_1(t), C_2(t)]^T$, of the three

states $|\psi_0\rangle$, $|\psi_1\rangle$ and $|\psi_2\rangle$ respectively

$$H(t) = \hbar \begin{pmatrix} 0 & \frac{1}{2}\Omega_{01}(t) & 0 \\ \frac{1}{2}\Omega_{01}(t) & \Delta_{01} & \frac{1}{2}\Omega_{12}(t) \\ 0 & \frac{1}{2}\Omega_{12}(t) & \Delta_{01} - \Delta_{12} \end{pmatrix}. \tag{5.1}$$

Here $\Omega_{01}(t)$ and $\Omega_{12}(t)$ are the Rabi frequencies of the RF pulses corresponding to 01 and 12 transitions, and Δ_{01} and Δ_{12} are the single-photon detunings from their respective transition frequencies. The Hamiltonian $H(t)$ has the three instantaneous eigenstates given by

$$|\Phi_+(t)\rangle = |\psi_0\rangle \sin\vartheta(t) \sin\varphi(t) + |\psi_1\rangle \cos\varphi(t) + |\psi_2\rangle \cos\vartheta(t) \sin\varphi(t) \tag{5.2}$$

$$|\Phi_0(t)\rangle = |\psi_0\rangle \cos\vartheta(t) - |\psi_2\rangle \sin\vartheta(t) \tag{5.3}$$

$$|\Phi_-(t)\rangle = |\psi_0\rangle \sin\vartheta(t) \cos\varphi(t) - |\psi_1\rangle \sin\varphi(t) + |\psi_2\rangle \cos\vartheta(t) \sin\varphi(t) \tag{5.4}$$

where the mixing angles $\vartheta(t)$ and $\varphi(t)$ are defined (modulo π) as $\vartheta(t) = \arctan[\Omega_{01}(t)/\Omega_{12}(t)]$, $\varphi(t) = \frac{1}{2}\arctan[\sqrt{\Omega_{01}^2(t) + \Omega_{12}^2(t)}/\Delta]$. Here Δ is the two-photon resonance between the states $|\psi_0\rangle$ and $|\psi_2\rangle$, *i.e.,* $\Delta = \Delta_{01} - \Delta_{12}$. The eigenfrequencies corresponding to these eigenstates are given by

$$\varepsilon_0(t) = 0, \varepsilon_\pm(t) = \frac{1}{2}\Delta \pm \frac{1}{2}\sqrt{\Delta^2 + \Omega_{01}^2(t) + \Omega_{12}^2(t)}. \tag{5.5}$$

Now STIRAP can be explained from the dynamics of the adiabatic state $|\Phi_0(t)\rangle$. This state is a coherent superposition of the initial state $|\psi_0\rangle$ and the target state $|\psi_2\rangle$ and has no component of the intermediate state $|\psi_1\rangle$. The interesting feature to note is that $|\Phi_0(t)\rangle$ is a radiatively dark state. The microwave pulses are counter-intuitively sequenced, $\Omega_{01}(t)/\Omega_{12}(t) \xrightarrow{t\to-\infty} 0$ and $\Omega_{01}(t)/\Omega_{12}(t) \xrightarrow{t\to+\infty} \infty$, so that the mixing angle $\vartheta(t)$ rises from 0 to $\pi/2$, as time progresses from $-\infty$ to $+\infty$. From equation (5.3), it is straightforward to see that the adiabatic state $|\Phi_0(t)\rangle$ evolves from the state $|\psi_0\rangle$ initially, to a superposition of states $|\psi_0\rangle$ and $|\psi_2\rangle$ at intermediate times and finally to the target state $|\psi_2\rangle$ at the end of the interaction. This explains how the counterintuitive pulse ordering leads to an interaction where the state $|\Phi_0(t)\rangle$ links adiabatically the initial state $|\psi_0\rangle$ to the target state $|\psi_2\rangle$.

Diabatic transitions between the adiabatic states are parasitic in this scheme. So for a successful population transfer by STIRAP, the diabatic transition rates should be reduced to negligibly small values. This translates into the requirement that the coupling between each pair of adiabatic states is negligible compared to the difference between the energies of

these states. We can write this adiabatic condition with respect to the dark state $|\Phi_0(t)\rangle$ as

$$|\varepsilon_0 - \varepsilon_\pm| \gg |\langle \dot{\Phi}_0 | \Phi_\pm \rangle|. \tag{5.6}$$

For the case, $(\Delta = 0)$ the adiabaticity condition simplifies to

$$\sqrt{\Omega_{01}^2(t) + \Omega_{12}^2(t)} \gg |\dot{\vartheta}| \propto T^{-1} \tag{5.7}$$

where T is the pulse width. For simplicity, assume $\Omega_{01} = \Omega_{12} = \Omega_0$ (say). Then equation (5.7) can be written as $\Omega_0 T \gg 1$, which is equivalent to the adiabaticity condition of demanding a large pulse area. For practical applications, the product is designed to be in excess of 10, so that an efficient population transfer is ensured.

Summarizing, the conditions that should be carefully designed are two-photon resonance between states $|\psi_0\rangle$ and $|\psi_2\rangle$, counterintuitive pulse ordering, and adiabatic evolution. When these conditions are met, STIRAP guarantees a complete population transfer from $|\psi_0\rangle$ to $|\psi_2\rangle$. One interesting aspect is that the dark state has no component in the intermediate state $|\psi_1\rangle$, and hence this state remains unpopulated during the transfer. So the decay effects of the intermediate state have little impact on the transfer efficiency. The exceptional feature of STIRAP offers the advantage of population transfer in time scales that exceed the lifetime of intermediate state. Another interesting aspect of STIRAP is that it is very robust with respect to small errors in the frequencies of the drive signals as long as the two photon resonance condition is not violated. This makes the method resistant to for example charge noise of the transmon, and in principle allows very high transfer fidelities.

5.2.1 Measurement setup and experimental results

In the cQED setup, the three lowest energy levels were used in the ladder setup. Two independent radio frequency sources were used to address the two transition frequencies. The measurement setup is shown in Fig. 5.13.

The measurement results for the drive resonances and the simulation results for the target state occupancy are shown in Fig. 5.14.

5.2.2 State preparation and verification by quantum tomography

The first step in tomography is to obtain the calibration curves corresponding to the states. Following this, the quantum state is prepared and

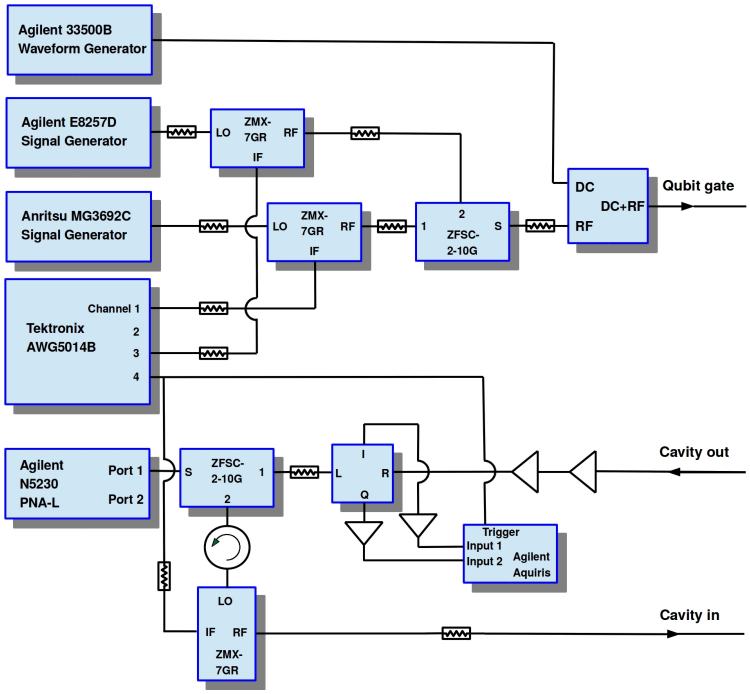

Figure 5.13. Schematic of the STIRAP measurement setup.

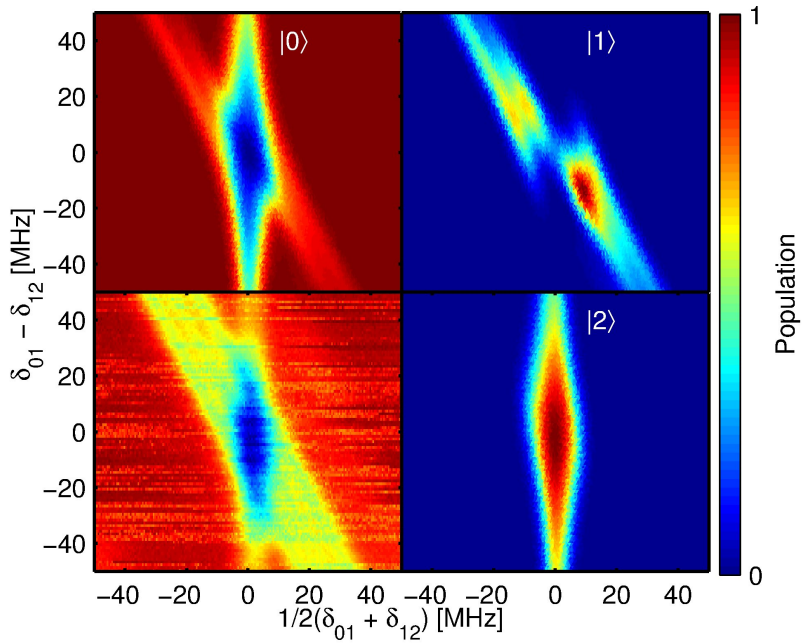

Figure 5.14. The lower left corner shows the experimental plot. The other plots show the simulation results for the probability of occupancy of the three states.

tomography pulses are used to measure the prepared state [70]. In the present case, we record the cavity response in time domain after preparing the transmon in state $\{|0\rangle, |1\rangle, |2\rangle\}$ respectively. The pulse sequence for the calibration process is shown in Fig. 5.15. Figure 5.15a shows a $2\pi_{01}$ pulse which prepares the qubit in the state $|0\rangle$ followed by a measurement pulse which records the response of the cavity corresponding to the qubit the state $|0\rangle$. In a similar fashion the qubit is prepared in state $|1\rangle$ by subjecting it to π_{01} pulse, and the measurement pulse probes the cavity (Fig. 5.15b). Figure 5.15c shows a π_{01} pulse followed by π_{12} pulse which prepares the qubit in the state $|2\rangle$. Following this the response of the cavity corresponding to the qubit in state $|2\rangle$ is recorded. The cavity response measured individually after preparing the qubit states as explained above, is shown in Fig. 5.16.

The STIRAP pulses are interrupted at several points before completion, and the cavity response is measured. Estimate of the population of states is made by numerical fitting, using the method of least squares. In other words, consider an arbitrary state $\rho(t)$ with diagonal elements $\alpha(t) = \mathrm{Tr}\left[|0\rangle\langle 0|\rho(t)\right]$, $\beta(t) = \mathrm{Tr}\left[|1\rangle\langle 1|\rho(t)\right]$ and $\gamma(t) = \mathrm{Tr}\left[|2\rangle\langle 2|\rho(t)\right]$ where $\alpha(t) + \beta(t) + \gamma(t) = 1$ and $0 \leq \alpha(t), \beta(t), \gamma(t) \leq 1$. The numerical fitting uses the calibration curves corresponding to $|0\rangle, |1\rangle, |2\rangle$, and tries to find the corresponding probability of occupancy $\alpha(t), \beta(t), \gamma(t)$, for the fractional STIRAP pulses. The pulse sequence for arbitrary state preparation is shown in Fig. 5.17 and the population of states calculated by tomography is shown in Fig. 5.18.

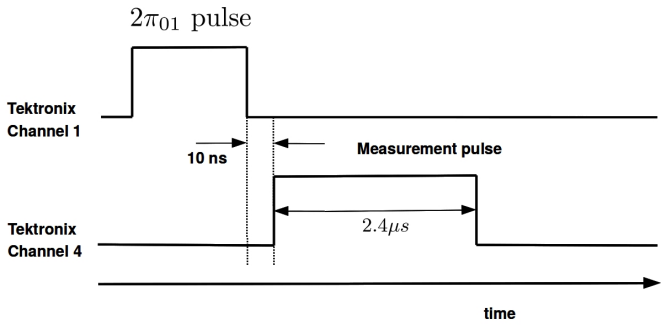

(a) Pulse sequence for calibration of the state $|0\rangle$.

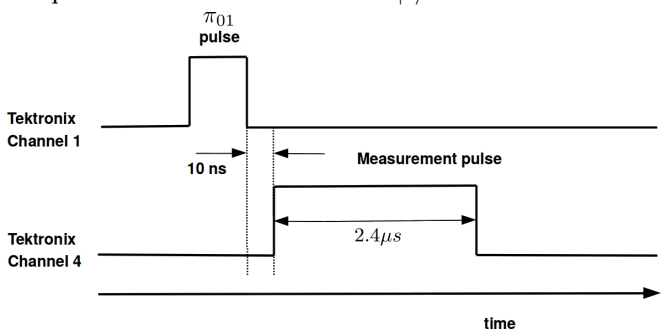

(b) Pulse sequence for calibration of the state $|1\rangle$.

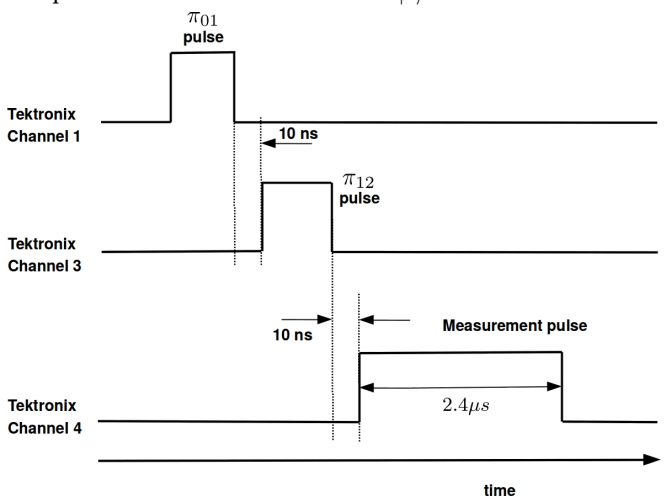

(c) Pulse sequence for calibration of the state $|2\rangle$.

Figure 5.15. Schematic of calibration sequence for tomography.

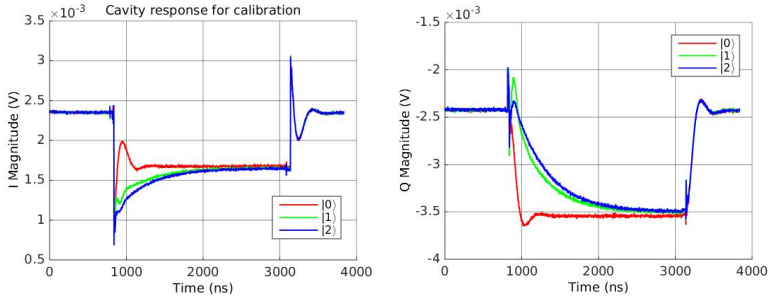

(a) In phase quadrature calibration cavity response.

(b) Out-of-phase quadrature cavity response.

Figure 5.16. Cavity response with qubit in $|0\rangle$, $|1\rangle$ and $|2\rangle$ state.

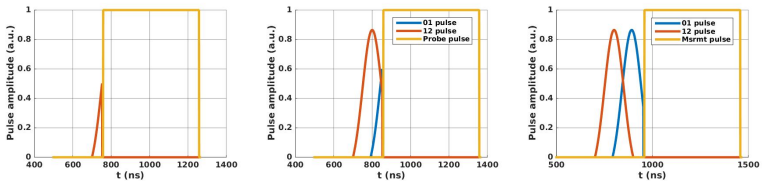

Figure 5.17. State preparation pulse sequence interrupted at different points a) before the 01 pulse b) in the middle of the STIRAP sequence c) near the end of the STIRAP sequence.

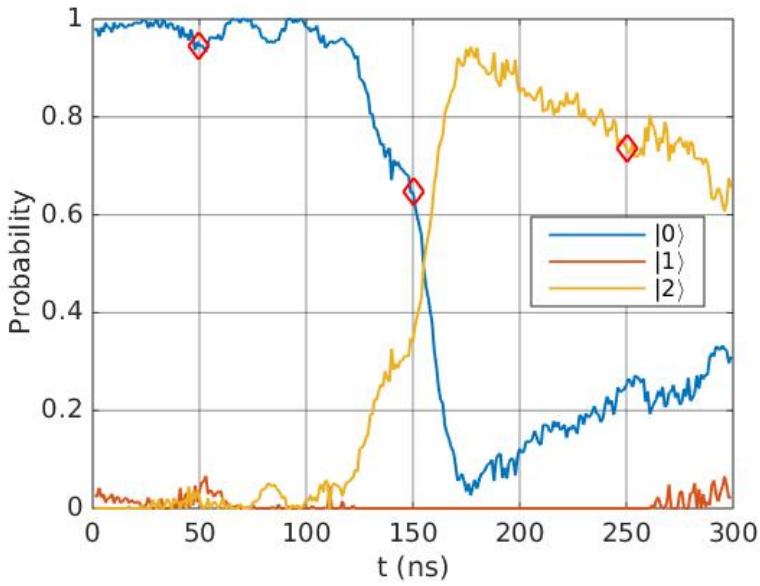

Figure 5.18. Population transfer by STIRAP experiment. The red diamond marker represent data corresponding to Fig. 5.17a,b and c, respectively.

5.3 Summary

We have shown that it is possible to achieve an efficient transfer of population from the ground state $|0\rangle$ to the second excited state $|2\rangle$ in a three level transmon system. This can be applied in many quantum information processing applications, where control of a three level system is required.

6. Summary and Conclusion

With a background in electronics, and working with algorithm design, I was naturally fascinated by the potential of quantum physics for quantum information processing. This fascination led to the exploration of the field, which resulted in Publication **I** .

The next step after getting introduced to quantum information processing, is to understand and implement the hardware to run the software. This desire was fulfilled as I had the opportunity to setup a Bluefors cryostat, measurement modules, intrument interfacing, computer control through the IEEE-488 GPIB buses and programming using MATLAB for measurement controlling and data processing, for Kvantti group, which subsequently led to the experiments and results presented in the thesis.

It was Richard Feynman's foresight that a quantum computer would be the optimal tool to simulate a many body quantum system. Publication **III** presents our steps in that direction: the motional averaging effect observed in large assemblies of particles, as in nuclear magnetic resonance in porous media, is simulated in a circuit QED setup.

Quantum optics deals with the quantum nature of light and its interactions with atoms. Harnessing the quantum nature of microwave radiation and observing its interactions with a tunable artificial atom, in circuit QED is fascinating in itself. In the circuit version of cavity QED, state control measurements similar to those observed in quantum optics were performed, which led to Publication **VI** .

In a wider perspective, the main challenges of building a quantum computer is the decoherence of the quantum states. In other words, the quantum architecture should ensure that the qubit is well isolated from sources of noise, but should enable selective coupling to external interactions during qubit control and readout. The architecture of a quantum computer should allow scalability while still retaining quantum coherence.

These mutually incompatible requirements constitute the challenges that raise the question whether building a quantum computer is physically possible.

Circuit QED started only in the mid 2000s and phenomenal progress has been made in just a decade. Compared to the first superconducting qubits, better designing of the qubit and isolation techniques improved the coherence time by a factor of $\sim 10^4$. There are numerous technological challenges to be solved before realising a quantum processor, but the interesting physics that gets disclosed in the pursuit, is in itself quite rewarding.

The idea of quantum mechanics on a chip and that of quantum light in a circuit were the inspirational concepts that led me towards a PhD in this field. And on the day, as I finish writing my thesis, these ideas still fascinate me with equal intensity. The field of circuit QED is still in its infancy and there are many more technological and conceptual challenges lying ahead.

The woods are lovely, dark, and deep,
But I have promises to keep,
And miles to go before I sleep,
And miles to go before I sleep.
- Robert Frost

Bibliography

[1] Shnirman, A., Schon, G. & Hermon, Z. Quantum manipulations of small Josephson junctions. *Phys. Rev. Lett.* **79**, 2371 – 2374 (1997).

[2] Bouchiat, V., Vion, D., Joyez, P., Esteve, D. & Devoret, M. H. Quantum coherence with a single Cooper pair. *Physica Scripta.* **T76**, 165 – 170 (1998).

[3] Nakamura, Y., Pashkin, Y. A. & Tsai, J. S. Coherent control of macroscopic quantum states in a single Cooper pair box. *Nature* **398**, 786 – 788 (1999).

[4] Deutsch, D. *The Fabric of Reality* (Penguin UK, 2011).

[5] Bell, J. S. On the Einstein-Podolsky-Rosen paradox. *Physics* **1**, 195 – 200 (1964).

[6] Nielsen, M. A. & Chuang, I. L. *Quantum Computation and Quantum Information* (2000).

[7] DiVincenzo, D. P. The physical implementation of quantum computation. *Fortschr. Phys.* **48**, 771 – 783 (2000).

[8] Shor, P. W. Polynomial-time algorithms for prime factorization and discrete logarithms on a quantum computer. *arXiv:quant-ph/9508027* (1995).

[9] Grover, L. K. Quantum mechanics helps in searching for a needle in a haystack. *Phys. Rev. Lett.* **79**, 325–328 (1997).

[10] Zhou, X.-Q., Kalasuwan, P., Ralph, T. C. & O'Brien, J. L. Calculating unknown eigenvalues with a quantum algorithm. *Nature Photonics* **7**, 223–228 (2013).

[11] v Dam, W. & Seroussi, G. Efficient quantum algorithms for estimating Gauss sums. *arXiv preprint quant-ph/0207131* (2002).

[12] Ralph, T. C. Quantum computation: Boson sampling on a chip. *Nature Photonics* **7**, 514–515 (2013).

[13] Broome, M. A. *et al.* Photonic boson sampling in a tunable circuit. *Science* **339**, 794–798 (2013).

[14] Harrow, A. W., Hassidim, A. & Lloyd, S. Quantum algorithm for linear systems of equations. *Phys. Rev. Lett.* **103**, 150502 (2009).

[15] Jordan, S. P. Fast quantum algorithm for numerical gradient estimation. *Phys. Rev. Lett.* **95**, 050501 (2005).

[16] Heinrich, S. Quantum integration in Sobolev classes. *Journal of Complexity* **19**, 19–42 (2003).

[17] Alter, O. & Yamamoto, Y. Inhibition of the measurement of the wave function of a single quantum system in repeated weak quantum nondemolition measurements. *Phys. Rev. Lett.* **74**, 4106 (1995).

[18] D'Ariano, G. M. & Yuen, H. P. Impossibility of measuring the wave function of a single quantum system. *Phys. Rev. Lett.* **76**, 2832 (1996).

[19] Wootters, W. K. & Zurek, W. H. A single quantum cannot be cloned. *Nature* **299**, 802–803 (1982).

[20] Galvao, E. F. & Hardy, L. Cloning and quantum computation. *Phys. Rev. A* **62**, 022301 (2000).

[21] Duan, L. M. & Guo, G. C. Probabilistic cloning and identification of linearly independent quantum states. *Phys. Rev. Lett.* **8**, 4999 (1998).

[22] Buzek, V. & Hillery, M. Universal optimal cloning of arbitrary quantum states: From qubits to quantum registers. *Phys. Rev. Lett.* **81**, 5003 (1998).

[23] Weile, D. S. & Michielssen, E. Genetic algorithm optimization applied to electromagnetics: A review. *IEEE Transactions on Antennas and Propagation* **45**, 343–353 (1997).

[24] Fortunato, E. M. *et al.* Design of strongly modulating pulses to implement precise effective hamiltonians for quantum information processing. *The Journal of chemical physics* **116**, 7599–7606 (2002).

[25] Josephson, B. D. Possible new effects in superconductive tunnelling. *Physics Letters* **1**, 251–253 (1962).

[26] Josephson, B. D. The discovery of tunnelling supercurrents. *Rev. Mod. Phys.* **46**, 251 (1974).

[27] Clarke, J. *SQUIDs: Principles, noise, and applications* (Academic Press, NY, 1990).

[28] Devoret, M. H., Martinis, J. M. & Clarke, J. Measurements of macroscopic quantum tunneling out of the zero-voltage state of a current-biased Josephson junction. *Phys. Rev. Lett.* **55**, 1908 (1985).

[29] Martinis, J. M., Devoret, M. H. & Clarke, J. Experimental tests for the quantum behavior of a macroscopic degree of freedom: The phase difference across a Josephson junction. *Phys. Rev. B* **35**, 4682 (1987).

[30] Clarke, J. & Wilhelm, F. K. Superconducting quantum bits. *Nature* **453**, 1031–1042 (2008).

[31] Devoret, M. H., Wallraff, A. & Martinis, J. M. Superconducting qubits: A short review. *arXiv:cond-mat/0411174* (2004).

[32] Makhlin, Y., Schön, G. & Shnirman, A. Quantum-state engineering with Josephson-junction devices. *Rev. Mod. Phys.* **73**, 357 (2001).

[33] Devoret, M. H. & Martinis, J. M. Implementing qubits with superconducting integrated circuits. In *Experimental Aspects of Quantum Computing*, 163–203 (Springer, 2005).

[34] Houck, A. A., Koch, J., Devoret, M. H., Girvin, S. M. & Schoelkopf, R. J. Life after charge noise: recent results with transmon qubits. *Quant. Inf. Proc.* **8**, 105 (2009).

[35] Koch, J. *et al.* Charge-insensitive qubit design derived from the Cooper pair box. *Phys. Rev. A* **76**, 042319 (2007).

[36] Blais, A., Huang, R. S., Wallraff, A., Girvin, S. M. & Schoelkopf, R. J. Cavity quantum electrodynamics for superconducting electrical circuits: An architecture for quantum computation. *Phys. Rev. A* **69**, 062320 (2004).

[37] Wallraff, A. *et al.* Strong coupling of a single photon to a superconducting qubit using circuit quantum electrodynamics. *Nature* **431**, 162–167 (2004).

[38] Fink, J. M. *et al.* Climbing the jaynes–cummings ladder and observing its $\sqrt{n}$ nonlinearity in a cavity QED system. *Nature* **454**, 315–318 (2008).

[39] Bishop, L. S. *et al.* Nonlinear response of the vacuum Rabi resonance. *Nat. Phys.* **5**, 105–109 (2009).

[40] Wallraff, A. *et al.* Approaching unit visibility for control of a superconducting qubit with dispersive readout. *Phys. Rev. Lett.* **95**, 060501 (2005).

[41] Schuster, D. I. *et al.* Resolving photon number states in a superconducting circuit. *Nature* **445**, 515–518 (2007).

[42] Schuster, D. I. *Circuit Quantum Electrodynamics*. Ph.D. thesis, Yale University.

[43] Reed, M. D. *et al.* High-fidelity readout in circuit quantum electrodynamics using the jaynes-cummings nonlinearity. *Phys. Rev. Lett.* **105**, 173601 (2010).

[44] Bishop, L. S., Ginossar, E. & Girvin, S. M. Response of the strongly-driven Jaynes–Cummings oscillator. *Phys. Rev. Lett.* **105**, 100504 (2010).

[45] Boissonneault, M., Gambetta, J. M. & Blais, A. Improved superconducting qubit readout by qubit-induced nonlinearities. *Phys. Rev. Lett.* **105**, 100504 (2010).

[46] Autler, S. H. & Townes, C. H. Stark effect in rapidly varying fields. *Phys. Rev.* **100**, 703 (1955).

[47] Shirley, J. H. Solution of the Schrödinger equation with a hamiltonian periodic in time. *Phys. Rev.* **138**, B979 (1965).

[48] Wilson, C. M. *et al.* Coherence times of dressed states of a superconducting qubit under extreme driving. *Phys. Rev. Lett.* **98**, 257003 (2007).

[49] Shevchenko, S. N., Ashhab, S. & Nori, F. Landau-Zener-Stückelberg interferometry. *Phys. Rept.* **492**, 1–30 (2010).

[50] Sillanpää, M., Lehtinen, T., Paila, A., Makhlin, Y. & Hakonen, P. Continuous-time monitoring of Landau-Zener interference in a Cooper-pair box. *Phys. Rev. Lett.* **96**, 187002 (2006).

[51] Oliver, W. D. *et al.* Mach-Zehnder interferometry in a strongly driven superconducting qubit. *Science* **310**, 1653–1657 (2005).

[52] Tuorila, J. *et al.* Stark effect and generalized Bloch-Siegert shift in a strongly driven two-level system. *Phys. Rev. Lett.* **105**, 257003 (2010).

[53] Grossmann, F., Dittrich, T., Jung, P. & Hänggi, P. Coherent destruction of tunneling. *Phys. Rev. Lett.* **67**, 516 (1991).

[54] Beaudoin, F., da Silva, M. P., Dutton, Z. & Blais, A. First-order sidebands in circuit QED using qubit frequency modulation. *Phys. Rev. A* **86**, 022305 (2012).

[55] Leek, P. J. *et al.* Using sideband transitions for two-qubit operations in superconducting circuits. *Phys. Rev. B* **79**, 180511 (2009).

[56] Li, J. *et al.* Motional averaging in a superconducting qubit. *Nature Communications* **4**, 1420 (2013).

[57] Allen, L. & Eberly, J. H. *Optical resonance and two-level atoms* (Courier Corporation, 2012).

[58] Grifoni, M. & Hänggi, P. Driven quantum tunneling. *Phys. Rept.* **304**, 229–354 (1998).

[59] Abragam, A. *The principles of nuclear magnetism* (Oxford University press, 1961).

[60] Anderson, P. W. A mathematical model for the narrowing of spectral lines by exchange or motion. *J. Phys. Soc. Jpn.* **9**, 316–339 (1954).

[61] Gardiner, C. & Zoller, P. *Quantum noise: a handbook of Markovian and non-Markovian quantum stochastic methods with applications to quantum optics*, vol. 56 (Springer Science & Business Media, 2004).

[62] Pirkkalainen, J. M. *et al.* Hybrid circuit cavity quantum electrodynamics with a micromechanical resonator. *Nature* **494**, 211–215 (2013).

[63] Niemczyk, T. *et al.* Circuit quantum electrodynamics in the ultrastrong-coupling regime. *Nature Physics* **6**, 772–776 (2010).

[64] Claudon, J., Zazunov, A., Hekking, F. W. J. & Buisson, O. Rabi-like oscillations of an anharmonic oscillator: Classical versus quantum interpretation. *Phys. Rev. B* **78**, 184503 (2008).

[65] Bylander, J. *et al.* Noise spectroscopy through dynamical decoupling with a superconducting flux qubit. *Nature Physics* **7**, 565–570 (2011).

[66] Luo, M. X., Ma, S. Y., Chen, X. B. & Yang, Y. X. The power of qutrit logic for quantum computation. *Int. J. Theor. Phys.* **52**, 2959–2965 (2013).

[67] Lanyon, B. P. *et al.* Simplifying quantum logic using higher-dimensional hilbert spaces. *Nat. Phys.* **5**, 134–140 (2009).

[68] Mangano, G., Siewert, J. & Falci, G. Sensitivity to parameters of STIRAP in a Cooper pair box. *Eur. Phys. J. Special Topics* **160**, 259–268 (2008).

[69] Falci, G. *et al.* Design of a lambda system for population transfer in superconducting nanocircuits. *Phys. Rev. B* **87**, 214515 (2013).

[70] Shalibo, Y. *et al.* Direct wigner tomography of a superconducting anharmonic oscillator. *Phys. Rev. Lett.* **110**, 100404 (2013).

A. Sample fabrication

In this Appendix I summarize the sample fabrication recipes used for the transmon devices presented in this thesis.

A.1 Wafer dicing

The substrate used was MTI undoped pure silicon with orientation-100, and resistivity $>$ 1000 Ω-cm. It is best to spin the wafer before dicing, to prevent the dust from the substrate and dicing-machine to attach to the chip surface. Additionally, blue tape can be attached for the protection of the resist and the silicon wafer surface, and then baked for approximately 10 mins at 50°C in the clean-room oven. The substrate wafer is then diced into 5x5 mm chips and the protection tape on top of the chips is removed carefully with tweezers. After inspection with an optical microscope to confirm that detrimental defects are not present, the chips are ready for patterning with the SEM (scanning electron microscope). If the dust particles on the surface make the diced chip unsuitable for lithography, it is best to clean the chip with acetone and repeat the resist spinning.

A.2 Spinning the resist layers

First the chips are cleaned by following the steps listed below:

1. The chips are fully immersed for 10 minutes in acetone on a 95°C hot plate. The beakers are placed in a water bath in order to prevent overheating.

2. The beakers containing either acetone or isopropanol are subjected to ultrasound cleaning for 10 minutes at 30 % ultrasound in either acetone

or IPA (isopropanol).

3. Following the ultrasound treatment, the chips are rinsed in IPA and dried with nitrogen so that no stains from solvent evaporation are left on the chips.

After the cleaning process is complete and the chips are inspected with an optical microscope, they are ready to be spin-coated with resists. Two layers of different resists, namely Copolymer EL10 and PMMA A3 are used for this purpose. The reason is that the Copolymer EL10 is more sensitive to electron beam than PMMA A3. This creates a larger undercut (a bridge over a sacrificial layer), which is important for shadow evaporation which leads to a Josephson junction. The following steps present the resist spinning parameters used for sample fabrication.

1. After plaching a small drop of Copolymer EL10 in the center of the chip, the chip is spun at 4000 rpm for 60 s. Then it is baked at 150°C on a hot plate for 90 s. The resulting thickness of the bottom layer is ~ 370 nm.

2. Then the second layer of resist PMMA A3 is applied on the chip and spun at 4000 rpm for 60 s and baked at 180°C for 90 s. The resulting thickness of the second layer is ~ 130 nm.

Note : if a nonconducting substrate such as sapphire is used, espacer is used as the third layer of the resist. The chip with espacer is spun at 4000 rpm for 60 s and then baked at 100°C for 90 s.

A.3 Electron-beam lithography

The electron-beam lithography parameters are usually specific to the SEM used. The parameters also drift over time leading to artifacts such as lithography offsets at higher magnification, stigma corrections and e-beam dosage fluctuations. These effects are to be monitored and corrected manually by maintaining a log of the parameters used over time. Below we describe the parameters we used when working with JEOL 7100+ SEM. The distance between the electron gun and the resist surface (working distance) was set to 10 mm. Before the e-beam exposure, offset and stigma corrections are made. The e-beam dosage and development time with

MIBK:IPA (Methyl isobutyl ketone : isopropanol) are related. Higher e-beam dose requires lower development time and vice-versa. For the area-dose of the order 300-400μC/cm^2 the following development recipe provided good results:

1. ~ 20 s at 1:3 MIBK:IPA,
2. Rinse with IPA to stop the development,
3. Blow dry with nitrogen,
4. Check with an optical microscope.

If there are defects observed in the optical microscope, oxygen plasma cleaning is done at 250 mTorr pressure for 15 s with an oxygen flow rate of 10 standard cubic centimeters per minute.

A.4 Shadow evaporation

Care should be taken that metallisation and oxidation is done in a chamber in which the conditions remain the same over time. Even small amounts of impurities in the vacuum chamber affect the oxidation rate and ultimately the obtained junction resistance.

1. Pump down the vacuum chamber to roughly 3×10^{-7} mbar and wait further for $\sim$15 minutes. It is beneficial to evacuate the chamber to roughly the same pressure since this will affect the resistances obtained.

2. Evaporate 30 nm of aluminium from an angle of +25 degrees. Evaporation rate should be around 1-2 Å/s.

3. Oxidize at a pressure 19 mTorr oxygen for 100 s.

4. Evaporate 60 nm of aluminium from an angle of -25 degrees. Evaporation rate should be around 2-4 Å/s.

A.5 Lift-off

After the evaporation is done, it is best to do the lift-off immediately.

1. The metallized chip is subject to boiling at 95°C acetone beaker immersed in a water bath for 3 minutes.

2. After 3 minutes, remove the acetone beaker from the hotplate. Firmly grip the chip with the tweezers and squirt the chip with hot acetone using a plastic syringe. After squirting for a few times, the aluminum will be washed away except for those places where the resist was not exposed to the electron beam.

3. After the unwanted aluminium is lifted off, remove the chip from acetone and rinse with isopropanol.

4. Dry the solvents using a nitrogen gun and examine the chip under the optical microscope.

Note : if the aluminium sticks persistently to the substrate surface, the options are to boil the chip longer for 5 to 10 minutes in acetone, or to sonicate the chip using ultrasound. However sonication should be the last resort as that can lead to breaking of the sensitive aluminium patterns. Lowest power and short pulse duration of ultrasound vibration should be used.

A.6 Measuring the Josephson test-junction resistance

After the transmon chip is fabricated, the next step is to measure the resistance of the Josephson test junctions. In order to avoid misleading resistance measurements, the substrate is cooled to liquid nitrogen temperatures as even high resistivity silicon has a finite conductance at room temperature. Some silicon substrates at room temperature give a contribution of ~ 20 kΩ, leading to erratical Josephson junction resistance values.

1. Wire-bond the test junction to the ports.

2. Ensure that the wire-bonds connect the ports using a voltmeter. Care should be taken that the voltmeter shares the same ground as the bonder. Also ground yourself using the wrist-band which is connected to the ground of the setup.

3. It is best to have a ~ 20 kΩ resistor in parallel. A Fluke III multimeter is used, and the resistance range is manually adjusted to ensure that the overcurrent from the multimeter does not break the junctions.

4. Ground the liquid nitrogen dewar, the multimeter, and user to the same ground. Gently dip the sample box into the liquid nitrogen dewar. The same procedure can be done also at liquid helium temperature using a liquid helium dewar.

5. After observing the resistance, gently lift the sample box and bring them to room temperature using a heat gun. Care should be taken that there is no condensed water remaining.

6. Remove the bonds fully using tweezers so that no loose hanging wires are present.

Note: for sapphire samples, the same procedure is followed at room temperature as the substrate is an electrical insulator.

A.7 Bonding the sample for cooldown

The sample holder should be cleaned and the oxide layer on copper should be finely removed using a scalpel. The oxide layer is what causes majority of bonding problems. GE varnish is used to attach the sample to the sample holder. Also checking that the bond wire runs directly below the bond needle ensures that the bond sticks to the surface. Feeding some wire manually, and checking using the optical microscope helps in checking that the bond wire is below the bond needle. The pads to the coplanar waveguide and the gate to the qubit are bonded with at least 5 wires. The ground of the chip is bonded to the ground of the sample box with as many bonds as possible, maintaining a distance of $\lesssim 0.5$ mm between the parallel bonds.

Aalto-DD 158/2015

ISBN 978-952-60-6477-2 (printed)
ISBN 978-952-60-6478-9 (pdf)
ISSN-L 1799-4934
ISSN 1799-4934 (printed)
ISSN 1799-4942 (pdf)

Aalto University
School of Science
Department of Applied Physics
www.aalto.fi

BUSINESS +
ECONOMY

ART +
DESIGN +
ARCHITECTURE

SCIENCE +
TECHNOLOGY

CROSSOVER

DOCTORAL
DISSERTATIONS